CONSEQUENCES OF BEING OUT OF SHAPE: THE EFFECTS OF BEAM DISTORTIONS IN ADVANCED INTERFEROMETRIC GRAVITATIONAL WAVE DETECTORS

by

DANIEL AXEL WILHELM TÖYRÄ

A thesis submitted to the University of Birmingham for the degree of

DOCTOR OF PHILOSOPHY

Institute of Gravitational Waves
Astrophysics and Space Research Group
School of Physics and Astronomy
College of Engineering and Physical Sciences
University of Birmingham
September 2018

Abstract

The era of gravitational wave astronomy has begun, which enables us to collect complementary information on events that can be seen by other means, and to study events that previously were invisible. The gravitational wave detectors that have made this possible, use laser interferometry to measure the gravitational-wave induced differential length change in two perpendicular arms. These laser interferometers are optical systems with high complexity, and can therefore be challenging to understand, diagnose and design. Numerical modelling softwares provide a bridge in the gap between theory and experiment, which allows for studying the realistic effects of isolated variables or perturbations, and exploring the large parameter space of the detectors. This can be used to contribute to design improvements, or identifying the cause of a certain symptom seen in the experiment.

The aim of the work presented in this thesis is to contribute to the commissioning and design processes of gravitational wave detectors by building and simulating realistic models, as well as developing tools that enable and/or facilitate the same for others. In particular, this work focus on the effects of beam distortions and misalignments in the LIGO and Virgo gravitational wave detectors. These beam distortions can be modelled by adding spatial higher-order Hermite-Gaussian modes to the ideal Gaussian beam.

We have quantified the effects of spatial mode mismatches on the performance of frequency dependent squeezed light, which is planned to be used in the near-future. A way of mitigating this negative effect is proposed, which includes the use of squeezed higher-order spatial modes. In addition, this work includes commissioning modelling for Virgo, related to the length control of the near-unstable power recycling cavity

during lock acquisition, and creating a LIGO model designed for alignment sensing modelling.

DEDICATION

I dedicate this work to my parents and sister, who have always supported and encouraged me.

ACKNOWLEDGEMENTS

This work was supported by the People Programme (Marie Curie Actions) of the European Union's Seventh Framework Programme FP7/2007-2013/ (PEOPLE-2013-ITN) under REA Grant Agreement No. (606176).

I would like to express my gratitude to my primary supervisor, Professor Andreas Freise, for giving me the opportunity to pursue a PhD degree, for teaching me how to do research, and for great advice in general. The time as Andreas' student has been an invaluable experience for me.

I would also like to express my gratitude to my two secondary supervisors, Haixing Miao and Conor Mow-Lowry, for all the help and support they have given me. A special thanks to Haixing, whom I had the great privilege of working with on the squeezed higher-order modes project. It was motivating and a lot of fun to work with you. A special thanks to Conor for many fun evenings at various pubs.

Many thanks to all my Birmingham PhD colleagues and postdocs: Anna Green, Daniel Brown, Miguel Dovale, Haoyu Wang, Sam Cooper, Aaron Jones, Chris Collins, Mengyao Wang, Artemiy Dmitriev, Kazuhiro Agatsuma, Samuel Rowlinson, Philip Jones, Chiara Di Fronzo, and Joe Bentley. Special thanks to Anna Green with whom

I shared the experience of being a PhD student, and to Daniel Brown who has been an invaluable FINESSE and PyKat support system as well as a great collaborator and project leader on PyKat developing.

An enormous thank you to the Birmingham people I spent most of my non-working time with: Serena Vinciguerra, James Barrett, Matthew Hunt, Alejandro Vigna Gomez, Coenraad Neijssel, Hannah Middleton, Matteo Bianconi, Kathrine Grover, Carl-Johan Haster, Simon Stevenson, Jacob Crossett, Jack Gartlan, Eddie Ross, Matthew Robson, Max Jones and Robin Smith. You all contributed significantly to make my time in Birmingham joyful. I also want to thank our favourite bartender Judith Julius, who has served me and the rest of the people above an uncountable number of beers and drinks at staff house.

Thank you my GraWIToN colleagues (Serena Vinciguerra, Shubhanshu Tiwari, Matthieu Gosselin, Marina Trad Nery, Jose Maria Gonzalez, Akshat Singhal, Imran Khan, Omar de Varona, Gang Wang, Gregoire Lacaille, Rudy Nahed, Zeno Tornasi, and Justus Schmidt) and GraWIToN associates (Ornella Piccinni, Diego Bersanetti, Eleonora Capocasa, Maria Bader, Janis Wöhler, Martina Neri, Yann Bouffanais, Donatella Fiorucci, etc.). It has been a great pleasure to get to know you and to have your company at many schools and conferences.

Many thanks to the 10 meter prototype group at the Albert Einstein Institute in Hannover, for hosting me for a month, and especially Harald Lück and Vaishali Adya for collaborating with me. Also, thank you Vaishali for taking care of me and making me feel welcome.

Thank you everyone at EGO for hosting me for two months, and special thanks to Madalena Mantovani and Julia Casanueva for working with me and making me feel welcome even during a stressful commissioning period. Also, thank you Matthieu, Julia, Annalisa Allocca, and Daniel Hoak for driving me to the site every day.

Thanks to all other people that I have had the privilege of collaborating with, most notably Antonio Perreca, Valeria Sequino and Alessio Rocchi. I have learned a lot from you.

Thank you Olov Öhgren, Arvid Siegwan, Julia Lindgren, Linnea Persson, Nils Lerner, Erik Tjernqvist, Daniel Lundmark, Annie Hittenkofer, Sandra Wikström, Maja Marklund, Ida Vincent, Sam Remmets, Mattias Gustavsson and Johan Lindsten for being great friends that support me and are there for me whenever I need you. Parts of this thesis were even written when I was hosted by some of you.

I have had the fortune of having many great school teachers, of whom I would like to especially acknowledge Siw Carlsson, Per-Olof Nilsson, and Torvald Segerstedt. You contributed to making me enjoy studying and spending time in school.

To my parents Svante Töyrä and Ann-Sofi Töyrä, and my sister Amanda Töyrä: thank you for always supporting me in whatever I do in life. I would not be here without you.

Thank you Vaishali Adya for putting up with me, and keeping me somewhat sane and floating during the time I wrote this thesis. You are invaluable to me.

CONTENTS

LIST OF FIGURES

LIST OF TABLES

NOMENCLATURE

This is a list of acronyms and abbreviations that are used within the body of this thesis.

AR	Anti-reflective
AS	Asymmetric port. The main port, located after the signal recycling mirror in LIGO, seen from within the interferometer.
ASC	Alignment Sensing and Control
BS	Beamsplitter
CARM	Common ARM length
CM1	Curved mirror 1: a mirror in the OMC of LIGO
CM2	Curved mirror 2: a mirror in the OMC of LIGO
CPX	Compensation plate X, located behind the AR-surface of ITMX in LIGO
CPY	Compensation plate Y, located behind the AR-surface of ITMY in LIGO
DARM	Differential ARM length
EOM	Electro-optic modulator
ETMX	End Test Mass X of LIGO
ETMY	End Test Mass Y of LIGO
FC	Filter Cavity
FSR	Free Spectral Range
FWHM	Full Width at Half Maximum

HAM	Horizontal Access Module
HG	Hermite-Gaussian
HR	Highly-reflective
IC	Input coupler: input mirror of the OMC in LIGO
IM1	Input mirror 1: a mirror in the input path of LIGO
IM2	Input mirror 2: a mirror in the input path of LIGO
IM3	Input mirror 3: a mirror in the input path of LIGO
IM4	Input mirror 4: a mirror in the input path of LIGO
IMC	Input Mode Cleaner
ITMX	Input Test Mass X of LIGO
ITMY	Input Test Mass Y of LIGO
LIGO	Laser Interferometer Gravitational-Wave Observatory
LSC	Length Sensing and Control
MC1	Mode cleaner 1: a mirror in the IMC of LIGO
MC2	Mode cleaner 2: a mirror in the IMC of LIGO
MC3	Mode cleaner 3: a mirror in the IMC of LIGO
MICH	Michelson differential length
NE	North end mirror of Virgo
NI	North input mirror of Virgo
OC	Output coupler: output mirror of the OMC in LIGO
OM1	Output mirror 1: mirror in the output path of LIGO
OM2	Output mirror 2: mirror in the output path of LIGO
OM3	Output mirror 3: mirror in the output path of LIGO
OMC	Output Mode Cleaner
POP	Port located on transmission through PR2 in LIGO
PR	Power recycling mirror of Virgo
PR2	Mirror in the power recycling path of LIGO
PR3	Mirror in the power recycling path of LIGO

PRC	Power Recycling Cavity
PRCL	Power Recycling Cavity Length
PRM	Power Recycling Mirror of LIGO
QPD	Quadrant Photo Detector
REFL	The port located on reflection off the power recycling mirror in LIGO.
RoC	Radius of Curvatue
SR2	Mirror in the signal recycling path of LIGO
SR3	Mirror in the signal recycling path of LIGO
SRC	Signal Recycling Cavity
SRCL	Signal Recycling Cavity Length
SRM	Signal Recycling Mirror of LIGO
TR_X	Transmission X. Port located on transmission through ETMX of LIGO
TR_Y	Transmission Y. Port located on transmission through ETMY of LIGO
TRANSMON EX	Optical table located behind ETMX in LIGO
TRANSMON EY	Optical table located behind ETMY in LIGO
WE	West end mirror of Virgo
WFS	Wavefront Sensor
WI	West input mirror of Virgo

CHAPTER 1

INTRODUCTION

When the Laser Interferometer Gravitational-Wave Observatory (LIGO) observed a binary black hole merger [1], on September 14, 2015 at 09:50:45 UTC, gravitational waves were for the first time both directly detected and used to study the universe. A new window to the outer space was opened that enables us to directly observe objects that up until then were invisible. The signal measured by the two LIGO detectors from this event is shown in figure 1.1. To date, a total of five binary black hole mergers [2, 3, 4, 5] have been observed by LIGO. The latest of these was also seen by the Virgo detector, which significantly improved the sky localisation. This improvement was of great importance when LIGO and Virgo three days later for the first time observed

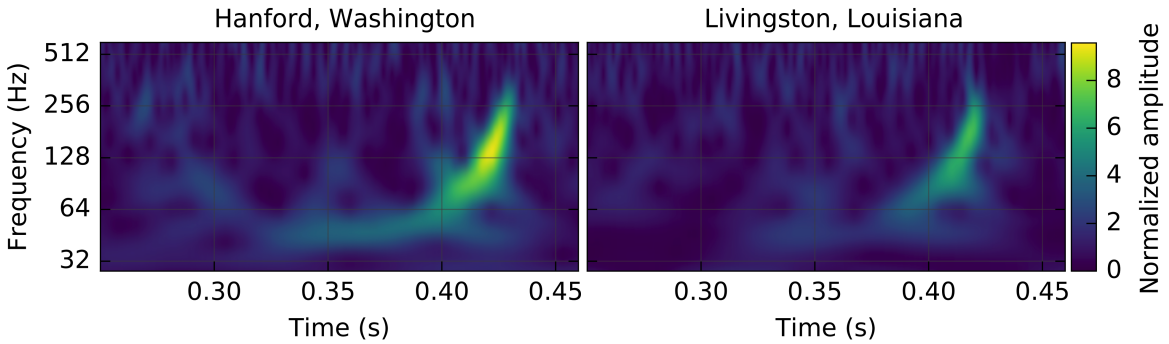

Figure 1.1: The signals seen by the two LIGO detectors from the first observed gravitational wave event [1].

two neutron stars inspiral and cause a kilonova when merging [6]. The sky localisation provided by the three gravitational wave detectors enabled telescopes to focus on the region and subsequently observe the aftermath of the collision through electromagnetic waves within multiple frequency bands of the electromagnetic spectrum [7]. In addition, gamma-ray bursts were detected by the Fermi Gamma-ray Burst Monitor (Fermi GBM) [8] and the International Gamma-Ray Astrophysics Laboratory (INTEGRAL) spacecraft [9]. This was a milestone in multi-messenger astronomy as it was the first time gravitational waves and electromagnetic waves from the same event were observed.

Since gravitational waves are the only information carriers generated by gravity, they are unique sources of information on events in the macroscopic universe. Gravitational waves are very weakly coupled to matter, which makes them challenging to detect, but it also allows them to propagate almost undisturbed through space and therefore provide a clear view of their origin. As the process that generates gravitational waves is fundamentally different from the processes generating the other information messengers, they can both provide complimentary information on events seen by other means, and allow us to observe events that otherwise would be invisible, such as colliding black holes. Information collected via gravitational waves can for example put bounds on possible neutron star equations of state [10, 11], and on the speed of gravity [12]; provide tests for general relativity [13]; and provide an independent measure of the Hubble constant [14].

Interferometric gravitational wave detectors use laser interferometry to measure the gravitational-wave induced relative motion between nearly free test masses. These laser interferometers are optical systems with high complexity, and can therefore be challenging to understand, diagnose and design. Numerical modelling softwares serve as a bridge in the gap between theory and experiment, which allows for studying the

realistic effects of isolated variables or perturbations, and exploring the large parameter space of the detectors. This can be used to contribute to design improvements, or identifying the cause of a certain symptom seen in the experiment.

The aim of the work presented in this thesis is to contribute to the commissioning and design processes of gravitational wave detectors by building and simulating realistic models, as well as developing tools that enable and/or facilitate the same for others. In particular, this work focus on the effects of beam distortions and misalignments in the LIGO and Virgo gravitational wave detectors. These beam distortions can be described by adding spatial higher-order Hermite-Gaussian modes to the ideal Gaussian beam.

This chapter is outlined as follows. Section 1.1 gives an overview of the thesis and brief descriptions of the chapters. In section 1.2, the nature and effect of gravitational waves are described. Section 1.3 introduces the network of interferometric gravitational wave detectors, and explains the basics of their functionality, and their response to gravitational waves. In section 1.4, the basics of the theory used to analyse the laser interferometer is introduced. Section 1.6 introduces the simulation software FINESSE and its Python wrapper PyKat, each of which have been used extensively to carry out the work presented in this thesis.

1.1 Thesis overview

In chapter 1 gravitational waves, gravitational wave detectors and their optical systems are introduced, as well as the basic theory used for laser optics.

Chapter 2 describes published work on how frequency dependent squeezed light is ef-

fected by spatial mode mismatches. In addition we show that the system can be made resilient to spatial mode matches by injecting squeezed higher-order modes.

Chapter 3, presents work on quantifying how the Virgo power recycling cavity (PRC) length sensing signal is affected by power recycling mirror (PRM) misalignments. This includes describing how to model a near-unstable cavity like the Virgo PRC in a realistic way, and describing for which modelling tasks this might require that a large amount of higher-order modes are included.

Chapter 4 describes work on building a FINESSE model of the LIGO Livingston detector that can be used for misalignment modelling. It is also shown that the simulated responses of the wavefront sensors to the misalignment degrees of freedom agree relatively well with measured data.

1.2 Gravitational waves

The existence of gravitational waves was predicted by Albert Einstein in 1916 [15] as he found wave solutions to the linearised weak-field approximation of the field equations he put forward a year earlier. These waves stretch and squash space itself as they propagate with the speed of light in the fabric of spacetime. The effect that a passing gravitational wave has on a ring of free test masses is shown in figure 1.2. Here, free means that each test mass is free to move in the plane of the paper. If the distances between the test masses along one transverse axis are increased, the distances between the test masses along the other transverse axis are decreased.

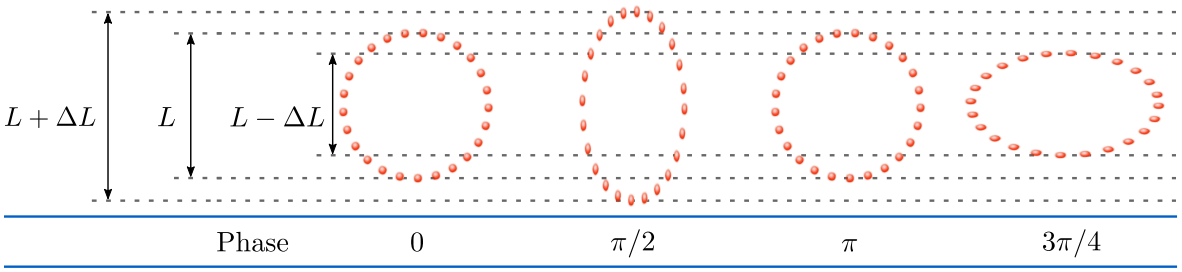

Figure 1.2: The figure shows the effect a gravitational wave has on the distances between free test masses that form a circle.

The far-field amplitude of a gravitational wave is to first order given by [16]

$$h_0(r) = \frac{2G}{c^4 r} \frac{\mathrm{d}^2 Q}{\mathrm{d}t^2}, \tag{1.1}$$

where r is the distance from the source, G is the gravitational constant, c is the speed of light and Q is the quadrupole moment of the source. The amplitude $h_0(r)$ is a dimensionless quantity that expresses strain, i.e., "length change per length". Thus, the length change ΔL and circle diameter L in figure 1.2 are related as

$$\Delta L = L\, h_0(r). \tag{1.2}$$

1.3 Interferometric gravitational wave detectors

The current network of ground based large-scale interferometric gravitational wave detectors is shown in figure 1.3. The operational detectors are the two LIGO detectors [17], located in Livingston, Louisiana and Hanford, Washington; Virgo [18] in Cascina, Italy; and GEO600 [19] in Hannover, Germany. In addition, KAGRA [20] in the Gifu Prefecture, Japan, is under construction and is expected to join the network in 2019, and LIGO India is a planned detector that is scheduled to be operational in 2025.

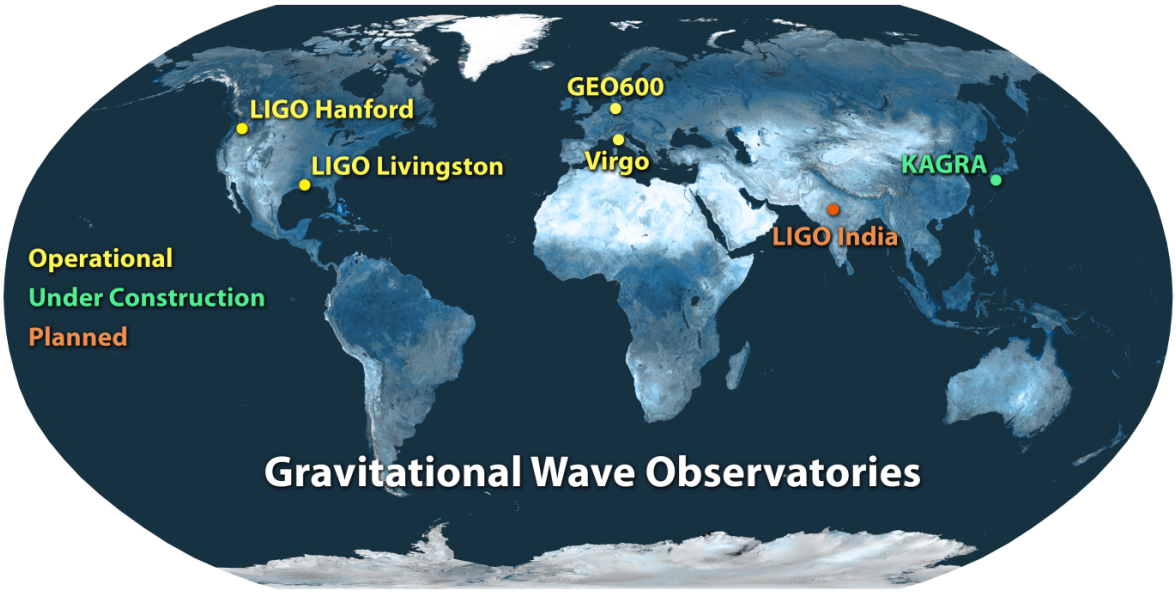

Figure 1.3: The current network of large-scale interferometric gravitational wave detectors. Courtesy Caltech/MIT/LIGO Lab.

1.3.1 Michelson interferometer and the principle of gravitational wave detectors

All current ground based gravitational wave detectors are based on the Michelson interferometer, which is shown in figure 1.4. Michelson interferometers employ light, ideally a laser beam, to measure the length difference between two paths commonly called arms. A beam splitter is used to divide the beam between the two arms, each of which has a free test mass in the end. The two test masses are mirrors that reflect

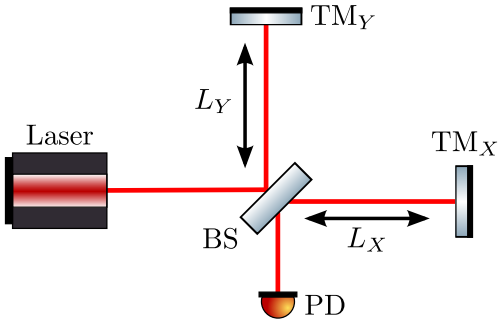

Figure 1.4: A Michelson interferometer. A beam splitter (BS) divides the beam between the two arms. The beams are reflected back to the beam splitter by the test mass (TM) mirrors, and the power is measured by a photodetector (PD). The measured power depends on the length difference between L_X and L_Y.

the beams back towards the beam splitter where they are recombined and interfere with each other. The Michelson interferometers used in gravitational wave detectors are operated at, or near, the dark fringe. This means that the interferometer is tuned such that the two beams interfere destructively at the photodetector-side of the beam splitter. The reason for choosing this operating point is that, at the dark fringe, sidebands generated by modulation effects that are differential between the two arms are maximally transmitted to the photodetector, while the transmission of sidebands generated by common effects is minimised. Gravitational waves are of differential nature, while for example laser noises are common. In the phase convention used in this work, a field transmitted through a mirror picks up a phase shift of $\pi/2$, while the phase shift of the reflected field is 0. Thus, if the path length between the beam splitter and test mass Y (TM_Y) is $L_Y + \lambda_0/4$, and the distance between the beam splitter and test mass X (TM_X) is L_X, the power detected by the photodetector is given by

$$\begin{aligned} P_{\mathrm{PD}} &= P_0 \sin^2(2k_0 \Delta L) \\ &= 16\pi^2 P_0 \frac{\Delta L^2}{\lambda_0^2} + \mathcal{O}\left(\left(\frac{\Delta L}{\lambda_0} \right)^4 \right) \end{aligned} \tag{1.3}$$

where $\Delta L = (L_Y - L_X)/2$, P_0 is the input power, $k_0 = 2\pi/\lambda_0$ the wavenumber, and λ_0 is the wavelength of the laser field. Thus, if $\Delta L = 0$ the interferometer is on the dark fringe. Small deviations from $\Delta L = 0$ results in a power on the photodetector that is proportional to ΔL^2, where small means that $\Delta L \ll \lambda_0$. The carrier wavelength used in the current gravitational wave detectors is $\lambda_0 = 1.064$ μm.

The effect of a passing sinusoidal gravitational wave can be seen by setting $\Delta L = Lh(t)$, where $L = (L_Y + L_X)/2$, $h(t) = h_0 \sin(\omega_{\mathrm{gw}} t + \varphi_{\mathrm{gw}})$, and ω_{gw} and φ_{gw} are the frequency

and phase of the gravitational wave. Thus, the power on the photodetector becomes

$$P_{\mathrm{PD}} = 16\pi^2 P_0 \frac{L^2 h_0^2}{\lambda_0^2} \sin^2(\omega_{\mathrm{gw}} t + \varphi_{\mathrm{gw}}) + \mathcal{O}\left(\left(\frac{L h_0}{\lambda_0} \right)^4 \right). \tag{1.4}$$

Since the amplitudes of gravitational waves on earth are expected to not exceed $h_0 \approx 10^{-20}$, the square of the number Lh_0/λ_0 is too small to measure with a photodetector. Therefore, to make P_{PD} proportional to Lh/λ_0, a technique called DC-readout [21, 22] is employed in current gravitational wave detectors. In this technique, a small static arm length difference δL_{off} is used to allow some coherent carrier light to leak out through the readout port of the beam splitter, which allows the signal sidebands to beat with this carrier field. The differential arm length becomes $\Delta L = \delta L_{\mathrm{off}} + Lh(t)$, which to first order (assuming that $\delta L_{\mathrm{off}} \ll \lambda_0$) yields the output power:

$$P_{\mathrm{PD}} \approx 32\pi^2 P_0 \frac{\delta L_{\mathrm{off}}}{\lambda_0} \frac{L h_0}{\lambda_0} \sin(\omega_{\mathrm{gw}} t + \varphi_{\mathrm{gw}}). \tag{1.5}$$

The exact value of the static offset δ_{off} is a tradeoff between signal and noise. It needs to be large enough so that the amount of coherent carrier light at the photodetector is large enough to dominate unwanted waste light that also reach the photodetector. This is to assure that the beat signal between the coherent carrier field and the signal sidebands is stronger than the beat signal between the waste light and the signal sidebands. On the other hand, the offset cannot be too large as control noises and the impact of laser noises increase with increasing δL_{off}.

So far, it has been assumed that the storage time $\tau = 2L/c$ (the time each photon spends in an arm) is small compared to the period time T_{gw} of the gravitational wave. This assumption was inherent in that only the total difference between the arm lengths was affected by the gravitational wave, which is equivalent to differentially moving the test masses. The gravitational wave strain however, stretches and squashes every

infinitesimal length segment $\mathrm{d}L$ in the arms. Thus, to calculate the effective ΔL due to a gravitational wave, the time varying strain needs to be integrated over the roundtrip length, or equivalently, over the storage time:

$$\begin{aligned} 2\Delta L &= \int_0^{2L} h(t)\mathrm{d}L \\ &= ch_0 \int_{t-\tau}^{t} \sin(\omega_{\mathrm{gw}} t + \varphi_{\mathrm{gw}})\mathrm{d}t \\ &= \frac{2ch_0}{\omega_{\mathrm{gw}}} \sin\left(\frac{\omega_{\mathrm{gw}} L}{c}\right) \sin\left(\omega_{\mathrm{gw}} t + \varphi_{\mathrm{gw}} - \frac{\omega_{\mathrm{gw}} L}{c}\right). \end{aligned} \tag{1.6}$$

The laser power impinging on the photodetector is in this case given by

$$P_{\mathrm{PD}} \approx 16\pi P_0 \frac{\delta L_{\mathrm{off}}}{\lambda_0} \frac{\omega_0}{\omega_{\mathrm{gw}}} h_0 \sin\left(\frac{L\omega_{\mathrm{gw}}}{c}\right) \sin\left(\omega_{\mathrm{gw}} t + \varphi_{\mathrm{gw}} - \frac{L\omega_{\mathrm{gw}}}{c}\right), \tag{1.7}$$

where $\omega_0 = 2\pi c/\lambda_0$ is the angular frequency of the carrier laser beam. From this expression one can see that the optimal arm length is $L = \lambda_{\mathrm{gw}}/4$. Thus, for gravitational wave frequency of 1 kHz, the arm length should ideally be about 75 km, and the ideal length grows longer with decreasing frequency. Such long arms are inconvenient, therefore optical cavities are used to trap the photons inside the arms for a longer time.

In this section, it has been assumed that the two beams have a perfect spatial overlap on the beam splitter. In reality however, the beams never perfectly overlap. This can be due to beam misalignments, or that the two beams have different sizes or shapes. Imperfect spatial overlaps introduce noise on the photodetector, which reduces the sensitivity to gravitational waves. The effects of such spatial beam imperfections is the main topic of the work presented in this thesis.

1.3.2 Fabry-Perot arm cavities

The longest arms used by the current interferometric gravitational wave detectors are the 4 km arms of the LIGO detectors, which is in the order of a factor of 10 shorter than the optimal length mentioned in section 1.3.1. Therefore, to increase the photon storage time, two test masses (mirrors) are used in each arm to form Fabry-Perot optical cavities that trap the photons for a longer time. A Michelson interferometer

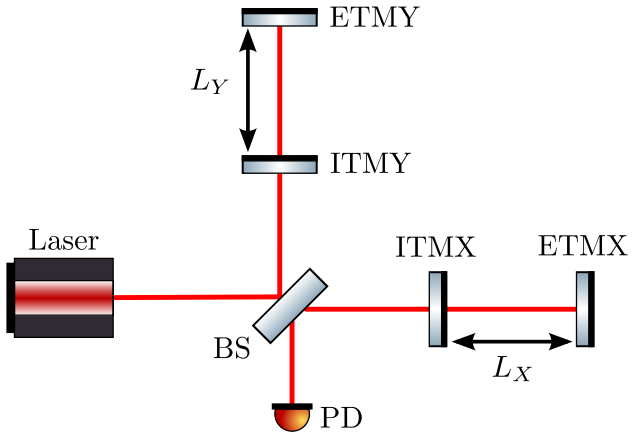

Figure 1.5: A Michelson interferometer with Fabry-Perot cavities. The difference compared to a simple Michelson interferometer (seen in 1.4) is that two extra test masses (mirrors) are added to form optical cavities in the arms. These cavities effectively increase the time the photons spend in the arms. The two test masses in each arm are referred to as input test mass (ITM) and end test mass (ETM).

with Fabry-Perot arm cavities is shown in figure 1.5. This setup requires that the cavities are set up such that the carrier field resonates inside the arms, which also has the effect of increasing the power inside the arms. The design arm cavity power gain of advanced LIGO is ≈ 290. This serves to increase the signal to shot noise ratio on the photodetector that limits the gravitational wave sensitivity at high frequencies, but it also increases the radiation pressure noise on the test masses, which limits the sensitivity at low frequencies.

1.3.3 Power recycling cavity

To increase the power in the arms without increasing the input laser power, a mirror between the laser and beam splitter can be added, as shown in figure 1.6. This power

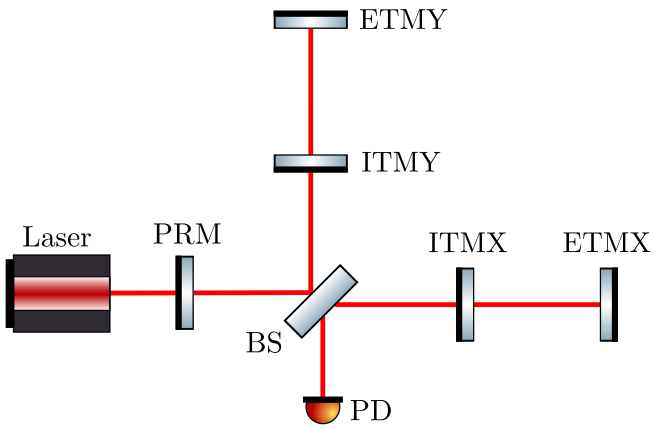

Figure 1.6: A Michelson interferometer with Fabry-Perot arm cavities and a power recycling cavity. Compared to figure 1.5, a power recycling mirror (PRM) has been added, which resonantly enhances the power in the arm cavities.

recycling mirror (PRM) forms the power recycling cavity (PRC) together with the input test masses. As the name suggests, this mirror is used to recycle the light that returns from the arms towards the laser, and send it back in towards the arms again. The advanced LIGO PRC is designed to resonantly enhance the carrier power by a factor of ≈ 40.

1.3.4 Signal recycling cavity

The signal recycling cavity (SRC) is formed by placing a signal recycling mirror (SRM) between the beam splitter and the photodetector, as shown in figure 1.7. As the name suggests, this cavity can be used to resonantly enhance the signal by reflecting the signal sidebands back into the arm cavities. This allows for increasing the sensitivity in a narrow bandwidth in exchange for reduced broadband sensitivity. The SRC can however, also be operated in signal extraction mode. In this mode, the signal

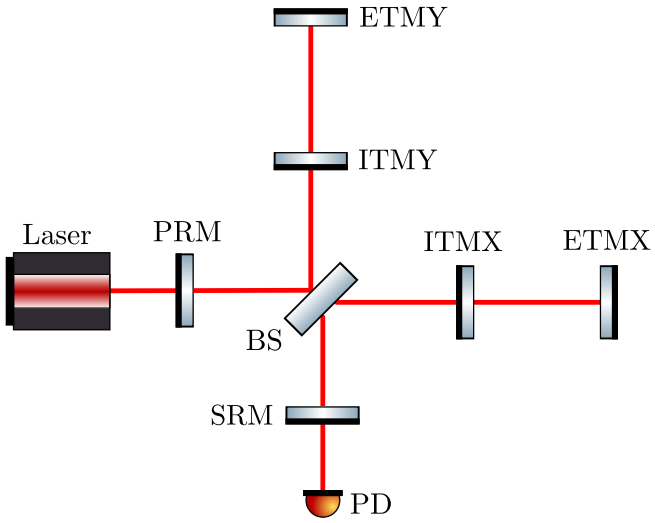

Figure 1.7: A Michelson interferometer with Fabry-Perot arm cavities, a power recycling cavity, and a signal recycling cavity. Compared to figure 1.6, a signal recycling mirror (SRM) has been added. This can serve to either increase the sensitivity in a narrow bandwidth, or to increase the bandwidth.

sidebands are anti-resonant in the SRC, which trades reduced peak sensitivity for increased broadband sensitivity. Advanced LIGO is currently operated using the signal extraction mode.

1.3.5 Mode cleaners

The input mode cleaner (IMC) is located between the laser and the power recycling mirror, and its purpose is to clean the laser beam from unwanted spatial higher-order modes (beam distortions) before entering the main interferometer. This is achieved by utilising the fact that spatial modes of different orders pick up different phases during propagation due to the Gouy-phase. The cavity is impedance matched to allow the resonating fundamental mode of the carrier to be transmitted, while it reflects beam components that are off resonance. Thus, the IMC is designed such that the first few higher-order modes are well outside the linewidth of the cavity, as these have the strongest couplings to the fundamental mode for small beam distortions.

The purpose of the output mode cleaner (OMC) is to clean the beam in the output port before it reaches the photodetector. In addition to filtering out beam distortions in the same way as the IMC, the OMC is also designed to filter out the RF-sidebands that are used for control of the interferometer, as these would add noise to the readout [23].

1.4 Laser optics for interferometry

1.4.1 The wave equation and the paraxial approximation

The electromagnetic wave equation derives from Maxwell's equations, and can be written in terms of either the electric or the magnetic field. Here, we chose to use a complex valued scalar function $E(\mathbf{r}, t)$ that describes the amplitude and phase of the electric field. it is given by

The electromagnetic wave equation derives from Maxwell's equation, and can be written

$$\left(\nabla^2 - \frac{1}{c^2}\frac{\partial^2}{\partial t^2}\right) E(\mathbf{r}, t) = 0, \tag{1.8}$$

where $E(\mathbf{r}, t)$ is a complex valued scalar function that describes the amplitude and phase of the electric field. The real valued scalar (the polarisation is omitted) electric field is given by $\mathrm{Re}\big(E(\mathbf{r}, t)\big)$.

where c is the speed of light in vacuum, and $\mathbf{r}$ is the position vector. Note that the polarisation of the electric field has been ignored, and a scalar electric field is used instead. This reason is that within the scope of this work, the only polarisation effect necessary to take into account is when the polarisation of the beam is misaligned to the axis of a polarising optic, which can be modelled as a loss. Assuming that

the temporal and spatial variables can be separated, the electric field can be written $E(\mathbf{r},t) = T(t)A(\mathbf{r})$, which allows for writing equation 1.8 as

$$\frac{1}{A(\mathbf{r})}\nabla^2 A(\mathbf{r}) = \frac{1}{c^2 T(t)}\frac{\mathrm{d}^2}{\mathrm{d}t^2}T(t). \tag{1.9}$$

Since the left hand side only depends on the spatial variable $\mathbf{r}$, and the right-hand side only depends on temporal variable t, general solutions to this equation must have both sides being constant. Thus,

$$\begin{aligned}\nabla^2 A(\mathbf{r}) &= -k^2 A(\mathbf{r}) \\ \frac{\mathrm{d}^2}{\mathrm{d}t^2}T(t) &= -k^2 c^2 T(t),\end{aligned} \tag{1.10}$$

where the constant $-k^2$ is chosen as it turns out to be convenient in the solution. The general solution to the temporal part is

$$T(t) = A\mathrm{e}^{i\omega t} + B\mathrm{e}^{-i\omega t}, \tag{1.11}$$

where $\omega = kc$ can be identified as the angular frequency.

The spatial part of the wave equation is called Helmholtz equation. By assuming that $A(\mathrm{r})$ can be written on the form $A(\mathbf{r}) = u(x,y,z)\mathrm{e}^{-ikz}$, where z is along the propagation direction of the wave, Helmholtz equation becomes

$$\begin{aligned}\mathrm{e}^{-ikz}\left(\frac{\partial^2}{\partial x^2} + \frac{\partial^2}{\partial y^2}\right)u(x,y,z) + \frac{\partial^2}{\partial z^2}\Big(u(x,y,z)\mathrm{e}^{-ikz}\Big) + k^2 u(x,y,z)\mathrm{e}^{-ikz} = 0 \\ \left(\frac{\partial^2}{\partial x^2} + \frac{\partial^2}{\partial y^2} + \frac{\partial^2}{\partial z^2}\right)u(x,y,z) - 2ik\frac{\partial}{\partial z}u(x,y,z) = 0.\end{aligned} \tag{1.12}$$

From here, the paraxial approximation is used, which means that it is assumed that the

second derivative of $u(x, y, z)$ with respect to z is much smaller than the other terms:

$$\begin{aligned}\frac{\partial^2 u}{\partial z^2} &\ll k\frac{\partial u}{\partial z},\\ \frac{\partial^2 u}{\partial z^2} &\ll \frac{\partial^2 u}{\partial x^2},\\ \frac{\partial^2 u}{\partial z^2} &\ll \frac{\partial^2 u}{\partial y^2}.\end{aligned} \tag{1.13}$$

Thus, the function $u(x, y, z)$ must vary slowly in the z-direction compared to the transverse directions, and compared to e^{-ikz}. The paraxial Helmholtz equation for $u(x, y, z)$ is given by

$$\left(\frac{\partial^2}{\partial x^2} + \frac{\partial^2}{\partial y^2}\right)u(x, y, z) - 2ik\frac{\partial}{\partial z}u(x, y, z) = 0. \tag{1.14}$$

This equation has many families of solutions, of which the Hermite-Gaussian (HG) functions (described in section 1.4.3) have been used throughout the work described in this thesis. These are commonly used for describing the spatial properties of laser beams propagating in free space, and they are particularly useful when there are rectangular symmetry in system, which is the case for the setups considered in this work. Another family of solutions that is commonly used for describing laser beams is the Laguerre-Gaussian functions.

1.4.2 Plane waves, definitions, and propagation

The obtained solution to the wave equation is

$$E(x, y, z, t) = \left(A\mathrm{e}^{i(\omega t - kz)} + B\mathrm{e}^{-i(\omega t + kz)}\right)u(x, y, z). \tag{1.15}$$

Here, the components with amplitudes A and B propagate forwards and backwards, respectively. For the purposes of this work however, there is no need to explicitly keep the backwards-propagating wave as we can add it back in when and if necessary. Thus we set $B = 0$. The spatial distribution $u(x, y, z)$ is described in section 1.4.3, and is of great importance in this thesis, however, we omit it in this section and only look at the plane wave solution given by

$$E(x, y, z, t) = A\mathrm{e}^{i(\omega t - kz)}. \tag{1.16}$$

This is a complex representation of the electric wave function, which in turn is given by $\mathcal{E}(x, y, z, t) = \mathrm{Re}\big(E(x, y, z, t)\big)$ and also solves the wave equation. For convenience however, we chose to work with the complex representation of the electric field. Further, the unit of the electric field is redefined to be in $\sqrt{\mathrm{W}}$, which can be done by letting $|A|^2 = P$ where P is the power of the field averaged over a period time. The reason for this is that the frequency ($\approx 2.8 \times 10^{14}$ Hz) of the carrier field used in gravitational wave detectors is too high to be resolved by the photodetectors, thus the average power is what is measured. The photodetectors used in gravitational wave detectors are able to resolve frequencies up to around the order of 100 MHz.

It should be borne in mind the parameters A, k, and ω are free as there are no boundary conditions constraining them. Thus, any sum $\sum_{j=0}^{\infty} A_j \mathrm{e}^{i(\omega_j - k_j z)}$ is also a solution to the wave equation.

1.4.3 Hermite-Gaussian modes

The Hermite-Gaussian solutions $u_{mn}(x, y, z)$ to the paraxial Helmholtz [24, 25, 26, 27] equation compose an orthonormal set over the xy-plane, i.e.,

$$\iint_{-\infty}^{\infty} u_{mn}(x, y, z) u^*_{m'n'}(x, y, z)\, \mathrm{d}x\mathrm{d}y = \delta_{mm'}\delta_{nn'}. \tag{1.17}$$

Thus, as long as the paraxial approximation is valid, any laser field with N frequency components can be described as

$$E(x, y, z, t) = \sum_{j=0}^{N-1} \sum_{m=0}^{\infty} \sum_{n=0}^{\infty} c_j a_{jmn} u_{mn}(x, y, z) \mathrm{e}^{i(\omega_j t - k_j z)} \tag{1.18}$$

where c_j is the total amplitude of frequency component ω_j, and

$$\sum_{m=0}^{\infty} \sum_{n=0}^{\infty} |a_{jmn}|^2 = 1. \tag{1.19}$$

The Hermite-Gaussian functions can be further separated into x and y as $u_{mn}(x, y, z) = u_m(x, z)u_n(y, z)$, where

$$u_n(x, z) = \left(\frac{\sqrt{2}}{2^n\, n! \sqrt{\pi}\, w(z)} \right)^{1/2} \mathrm{e}^{i\frac{2n+1}{2}\psi(z)} H_n\left(\frac{\sqrt{2}x}{w(z)} \right) \mathrm{e}^{-\frac{x^2}{w^2(z)}} \mathrm{e}^{-i\frac{kx^2}{2R_c(z)}}. \tag{1.20}$$

Here, $H_n(\xi)$ are the physicists' Hermite polynomials, given by

$$\begin{aligned} H_0(\xi) &= 1 \\ H_{n+1}(\xi) &= 2\xi H_n(\xi) - \frac{\mathrm{d}H_n(\xi)}{\mathrm{d}\xi} \end{aligned} \tag{1.21}$$

where the normalisation factors are included in $u_n(x, z)$. Ideally, the beam only contains the fundamental mode, but due to spatial defects such mode mismatched cavities and imperfect optics, the laser light scatter into higher-order modes. The parameters of the Gaussian beam are shown in figure 1.8, and described below. Two of the parameters,

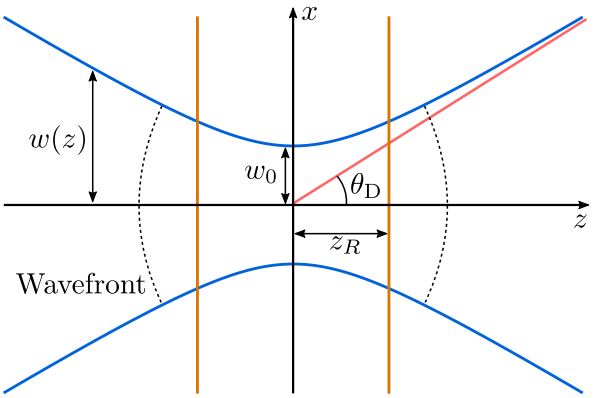

Figure 1.8: The figure shows the shape and the parameters of a gaussian beam.

the distance to the waist $z - z_0$ and the waist radius (waist size) w_0, are used to express the other parameters. These two can also be combined into the complex beam parameter as

$$q(z) = q_0 + z - z_0, \quad \text{where} \quad q_0 = i\frac{\pi w_0^2}{\lambda}. \tag{1.22}$$

The beam radius $w(z)$ is the transverse distance at which the intensity of the fundamental mode u_{00} has decreased by a factor of e^{-2} compared to at the centre of the beam. This parameter can be parametrised as

$$w(z) = w_0\sqrt{1 + \left(\frac{z - z_0}{z_R}\right)^2} = \sqrt{\frac{\lambda\,|q|^2}{\pi\,\mathrm{Im}(q)}}, \tag{1.23}$$

where

$$z_R = \frac{\pi w_0^2}{\lambda} = \mathrm{Im}(q) \tag{1.24}$$

is called the Rayleigh range. This is the distance from the waist at which the radius of curvature of the wavefront $R_c(z)$ reaches its minimum value of $2z_R$. At the waist the, $R_c(z) = \infty$ and in the far field defined by $z - z0 \gg z_R$, the radius of curvature grows

with the distance as $R_c(z) \to z - z_0$. This can also be seen from:

$$R_c(z) = z - z_0 + \frac{z_R^2}{z - z_0} = \frac{|q|^2}{\mathrm{Re}(q)}. \tag{1.25}$$

The diffraction angle θ_D is the angle between the optical axis and the waist size of the far field, and can be written as

$$\tan^{-1}\left(\frac{w_0}{z_R}\right) \approx \frac{w_0}{z_R} \tag{1.26}$$

The Gouy-phase $\psi(z)$ is an extra longitudinal phase that a beam with finite spatial distribution accumulates during propagation compared to a plane wave, and it is given by

$$\psi(z) = \tan^{-1}\left(\frac{z - z_0}{z_R}\right) = \tan^{-1}\left(\frac{\mathrm{Re}(q)}{\mathrm{Im}(q)}\right). \tag{1.27}$$

Thus, the the Gouy-phase goes from $-\pi/2$ at $z = -\infty$ to $\pi/2$ at $z = \infty$, and it is 0 at the beam waist. The smaller the Rayleigh range, the quicker the Gouy-phase changes along the z-axis in the region near the waist. Thus, a more focused beam accumulates Gouy-phase quicker than a less focused beam, which means that the cavity length and mirror radii of curvature determines the accumulated roundtrip Gouy-phase for an optical cavity eigenmode. Another important aspect of the Gouy-phase is that different spatial modes pick up different amounts of it, as seen from the mode number dependent factor in front of the Gouy-phase in 1.20. This means that different spatial modes generally have different resonant conditions in optical cavities, which is of importance throughout this thesis.

1.5 Quantum optics and squeezed light

The quantised electric field operator in the Heisenberg picture is

$$\hat{E}(\mathbf{r},t,q) = \int_0^\infty \frac{\mathrm{d}\omega}{2\pi}\sqrt{\frac{2\pi\hbar\omega}{\mathcal{A}c}}\sum_{mn}\left[\hat{a}_\omega \mathrm{e}^{-i(\omega t-kz)}u_{mn}(\mathbf{r},q) + \hat{a}_\omega^\dagger \mathrm{e}^{i(\omega t-kz)}u_{mn}^*(\mathbf{r},q)\right] \quad (1.28)$$

where $\mathcal{A}$ is the effective cross sectional are of the beam satisfying $(1/\mathcal{A})\int_{-\infty}^{\infty}|u(\mathbf{r},q)|^2\,\mathrm{d}x\mathrm{d}y = 1$; and $\hat{a}_\omega$ and $\hat{a}_\omega^\dagger$ are the annihilation and creation operators with the commutation relation $\left[\hat{a}_\omega, \hat{a}_{\omega'}^\dagger\right] = 2\pi\delta(\omega-\omega')$. Since we are interested in the quantum fluctuations at the gravitational wave sideband frequencies, each of these operators are split into creation and annihilation operators for a pair of sidebands surrounding the carrier frequency ω_0. Thus, we define $\hat{a}_\pm = \hat{a}_{\omega_0\pm\Omega}$ and $\hat{a}_\pm^\dagger = \hat{a}_{\omega_0\pm\Omega}^\dagger$. These can in turn be used to define the correlated two-photon operators [28, 29, 30]

$$\hat{a}_1 = \frac{\hat{a}_+ + \hat{a}_-^\dagger}{\sqrt{2}} \quad \text{and} \quad \hat{a}_2 = \frac{\hat{a}_+ - \hat{a}_-^\dagger}{i\sqrt{2}}. \quad (1.29)$$

By using the two-photon operators, and for simplicity omitting the spatial distribution of the field, the electric field operator in equation 1.28 can be written

$$\hat{E}(\mathbf{r},t,q) = \sqrt{\frac{4\pi\hbar\omega_0}{\mathcal{A}c}}\left(\hat{X}_1\cos(\omega_0 t) + \hat{X}_2\sin(\omega_0 t)\right). \quad (1.30)$$

where the cosine and sinus quadratures are

$$\hat{X}_{1,2} = \int_0^\infty \left(\hat{a}_{1,2}\mathrm{e}^{-i(\Omega t-kz)} + \hat{a}_{1,2}^\dagger \mathrm{e}^{i(\Omega t-kz)}\right)\frac{\mathrm{d}\Omega}{2\pi}. \quad (1.31)$$

Here, the fact that $\Omega \ll \omega_0$ has been used to approximate ω by ω_0 in the square root.

The variance of the quantum vacuum fluctuations can be computed as

$$V(\hat{X}_{1,2})_0 = \langle 0|\hat{X}_{1,2}^2|0\rangle - \langle 0|\hat{X}_{1,2}|0\rangle^2 \tag{1.32}$$

$$= 2\pi + 0, \tag{1.33}$$

where $|0\rangle$ is the vacuum state or lowest Fock state, which is the state with no excitation. Thus, it makes sense that the expectation value (second term above) evaluates to zero. To compute this, we have used that $\hat{a}_\pm |n\rangle = \sqrt{n}\,|n-1\rangle$ and $\hat{a}_\pm^\dagger |n\rangle = \sqrt{n+1}\,|n+1\rangle$.

The squeezed vacuum state [31] is defined as

$$|\chi\rangle = \hat{S}(r,\phi)\,|0\rangle \tag{1.34}$$

where $\hat{S}(r,\phi) = \exp\left[r\left(\hat{a}_+\hat{a}_- e^{-2i\phi} - \hat{a}_+^\dagger \hat{a}_-^\dagger e^{2i\phi}\right)\right]$ is the squeeze operator, r is the squeeze magnitude and ϕ is the squeeze angle. The effect the squeeze operator has on the two-photon operators is given by

$$\hat{S}^\dagger(r,\phi)\hat{a}_1\hat{S}(r,\phi) = \hat{a}_1(\cosh r + \sinh r\cos 2\phi) - \hat{a}_2 \sinh r \sin 2\phi, \tag{1.35}$$

$$\hat{S}^\dagger(r,\phi)\hat{a}_2\hat{S}(r,\phi) = \hat{a}_2(\cosh r - \sinh r\cos 2\phi) - \hat{a}_1 \sinh r \sin 2\phi. \tag{1.36}$$

From this, one can see that $\phi = 0$ gives $\hat{S}^\dagger\hat{a}_1\hat{S} = e^r\hat{a}_1$ and $\hat{S}^\dagger\hat{a}_2\hat{S} = e^{-r}\hat{a}_2$, while $\phi = \pi/2$ gives $\hat{S}^\dagger\hat{a}_1\hat{S} = e^{-r}\hat{a}_1$ and $\hat{S}^\dagger\hat{a}_2\hat{S} = e^r\hat{a}_2$. Thus, in the first case the quantum fluctuations are reduced (squeezed) in the sine quadrature, while they are increased (anti-squeezed) in the cosine quadrature, and the roles are switched in the second case. This means that the quantum fluctuations of the upper and lower sidebands are correlated, or entangled. This can be seen as trading increased uncertainty in momentum for decreased uncertainty in position, or vice versa. Since the current advanced gravitational wave detectors are limited by quantum noise in the upper part

of the bandwidth, and in the future they will be limited by the same also at lower frequencies, squeezed light will be used to further improve the sensitivity.

1.6 Finesse and PyKat

The simulation software FINESSE [32, 33, 27] and its Python wrapper PyKat [34] have been used extensively for the work presented in this thesis. A significant part of the work has been to develop (mainly PyKat) and test the softwares to enable myself and others to perform various simulation tasks.

FINESSE is a frequency domain simulation software, designed for realistic modelling of the laser optical systems in gravitational detectors. Most important for this work is that it is capable of computing the effects of various realistic optical defects, including misalignments and spatial mode mismatches between optical cavities, as well as simulating the quantum mechanical aspects of light, such as squeezed light, shot noise and radiation pressure noise.

FINESSE assumes that all components of the optical system can be described by a set of linear coupling coefficients that relates the input and output complex field amplitudes; the frequency of a field component never changes; and that there are no polarising components. If spatially finite beams are used in a simulation, FINESSE uses either Hermite-Guassian or Laguerre-Gaussian functions to describe the spatial distribution. As these are solutions to the paraxial Helmholtz-equation, the paraxial approximation must be valid for FINESSE to yield correct results.

FINESSE can perform both static and frequency dependent simulations. Here, static

means that an output signal is computed as a function of a parameter in the system. This could for example be a simulation of how the power inside an optical cavity depends on the position of one of the mirrors that compose the cavity. A frequency dependent simulation in FINESSE computes the behaviour of an output signal as a function of the frequency of a sinusoidal input signal, i.e., a transfer function or a frequency response is computed. For example, this can be a simulation of how a Michelson interferometer output signal depends on the frequency of a sinusoidal gravitational wave.

Given a user defined interferometer model, FINESSE converts the model into a matrix equation on the form

$$\mathbf{M}\,\mathbf{a} = \mathbf{a}_{\mathrm{in}}, \tag{1.37}$$

where the vector $\mathbf{a_{in}}$ contains the source field components, the interferometer matrix $\mathbf{M}$ contains all the couplings between the field components in the interferometer, and the vector $\mathbf{a}$ contains all the field components inside the interferometer, which are initially unknown. To solve this task, the matrix $\mathbf{M}$ is inverted, thus one obtains

$$\mathbf{a} = \mathbf{M}^{-1}\,\mathbf{a}_{\mathrm{in}}. \tag{1.38}$$

In general, FINESSE solves three such equations per simulated data point: one for the carrier fields created by lasers and their sidebands created by modulators; one for the signal fields, which are sidebands generated by for example a moving mirror or a gravitational wave; and one for the quantum noise sideband fields. The equation for the carrier fields is always solved first as these fields are assumed to be independent of the much smaller signal and quantum fields, while the signal and quantum field components depend on the carrier fields. FINESSE solves these matrix equations by using numerical sparse matrix solvers [33].

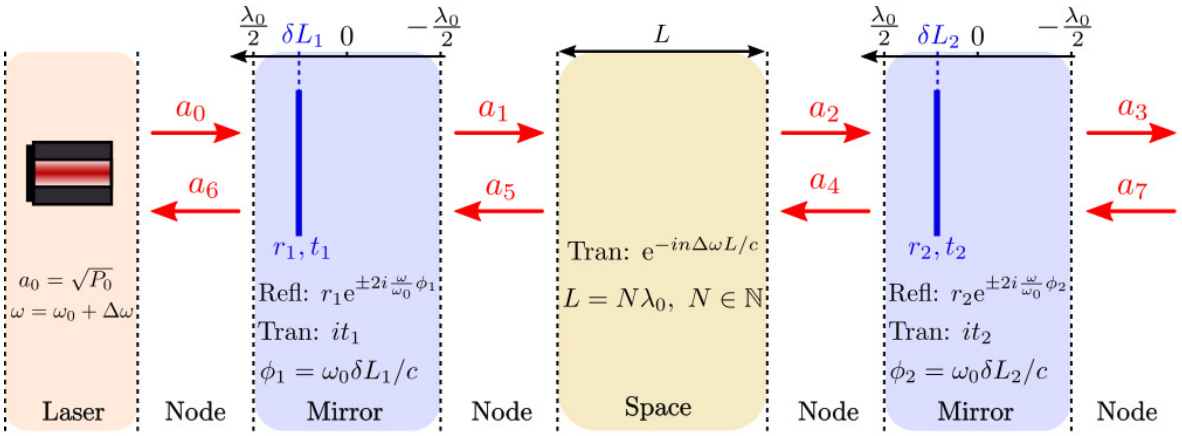

Figure 1.9: The figure visualises how FINESSE models a system that consists of a laser and a linear optical cavity. The system is modelled using four components: a laser, two mirrors, and a space. These components are connected by nodes, in which the field components a_k are computed. Here, P_0 is the input laser power, ω_0 is the reference frequency used by FINESSE (usually the frequency of the main laser), ω is the frequency of the field, $r_{1,2}$ and $t_{1,2}$ are the amplitude reflection and transmission coefficients of the mirrors, $\delta L_{1,2}$ are the microscopic position of the mirrors, L is the macroscopic length of the space, and n is the refractive index of the space.

A simple example of how FINESSE constructs the equations system for the carrier field is obtained by considering a system consisting of a plane-wave laser and a linear optical cavity, as shown in figure 1.9. Each component in the interferometer is represented by a set of coupling coefficients that determines the relations between the incoming and outgoing fields, except the laser which generates an input field with amplitude a_0 and angular frequency $\omega = \omega_0 + \Delta\omega$. The angular frequency ω_0 has a special meaning in FINESSE: the length of any space component is an integer multiple of the wavelength $\lambda_0 = 2\pi c/\omega_0$. Instead, the mirror component has a phase parameter ϕ that allows the mirror surface to be anywhere between two reference planes separated by the distance λ_0, as seen in figure 1.9. Thus, any physical distance D is split up into $D = L + \Delta L$, where the macroscopical distance L is a parameter of the space component, and the microscopical distance $\Delta L \leq \lambda_0$ is determined by the tuning parameter ϕ of the optics connected to the space. FINESSE uses the convention of phase shifts of 0 and $\pi/2$ on reflection off and transmission through a thin mirror mirror, respectively. The fields of

this example system can be described by the equation system:

$$\begin{aligned}
a_0 &= \sqrt{P_0} \\
a_1 &= it_1 a_0 + r_1 \mathrm{e}^{-2i\phi_1 \frac{\omega}{\omega_0}} \\
a_2 &= \mathrm{e}^{\frac{-in\Delta\omega L}{c}} a_1 \\
a_3 &= it_2 a_2 + r_2 \mathrm{e}^{-2i\phi_2 \frac{\omega}{\omega_0}} a_7 \\
a_4 &= r_2 \mathrm{e}^{2i\phi_2 \frac{\omega}{\omega_0}} a_2 + it_2 a_7 \\
a_5 &= \mathrm{e}^{\frac{-in\Delta\omega L}{c}} a_4 \\
a_6 &= r_1 \mathrm{e}^{2i\phi_1 \frac{\omega}{\omega_0}} a_0 + it_1 a_5 \\
a_7 &= 0.
\end{aligned} \tag{1.39}$$

If this is instead written on the form of equation 1.37, the interferometer matrix, the input vector, and the field vector become

$$\mathbf{M} = \begin{bmatrix}
1 & 0 & 0 & 0 & 0 & 0 & 0 & 0 \\
-it_1 & 1 & 0 & 0 & 0 & -r_1 \mathrm{e}^{\frac{-2i\phi_1\omega}{\omega_0}} & 0 & 0 \\
0 & -\mathrm{e}^{\frac{-in\Delta\omega L}{c}} & 1 & 0 & 0 & 0 & 0 & 0 \\
0 & 0 & -it_2 & 1 & 0 & 0 & 0 & -r_2 \mathrm{e}^{\frac{-2i\phi_2\omega}{\omega_0}} \\
0 & 0 & -r_2 \mathrm{e}^{\frac{2i\phi_2\omega}{\omega_0}} & 0 & 1 & 0 & 0 & -it_2 \\
0 & 0 & 0 & 0 & -\mathrm{e}^{\frac{-in\Delta\omega L}{c}} & 1 & 0 & 0 \\
-r_1 \mathrm{e}^{\frac{2i\phi_1\omega}{\omega_0}} & 0 & 0 & 0 & 0 & -it_1 & 1 & 0 \\
0 & 0 & 0 & 0 & 0 & 0 & 0 & 1
\end{bmatrix}, \tag{1.40}$$

$$\mathbf{a}_{\text{in}} = \begin{bmatrix} \sqrt{P_0} & 0 & 0 & 0 & 0 & 0 & 0 & 0 \end{bmatrix}^{\mathrm{T}}, \tag{1.41}$$

and

$$\mathbf{a} = \begin{bmatrix} a_0 & a_1 & a_2 & a_3 & a_4 & a_5 & a_6 & a_7 \end{bmatrix}^{\mathrm{T}}. \tag{1.42}$$

The size of this equation system grows with the number of included frequency components, spatial modes, and the number of nodes in the system.

PyKat is a python package that facilitates complex FINESSE modelling tasks, for example when multiple FINESSE-runs are required. Its recently developed IFO module include support for simulating Virgo and LIGO site specific models. It has been developed by the undersigned, together with Daniel Brown, Andreas Freise, and Anna Green, where I in particular have contributed to the Virgo-specific package and the misalignment modelling features.

FINESSE can have as many outputs as the user wants, but maximally two parameters of the model can be varied during one simulation. Therefore, many common simulation tasks, such as finding an operating point for an interferometer, optimising sensing signals, and computing spatial mismatches between many different optical cavities, require multiple simulations. PyKat includes many pre-defined functions for performing such modelling tasks, and it also provides tools that allows the users to build their own sets of FINESSE simulations.

1.7 Project motivation and significance

The work presented in this thesis focuses on the spatial aspects of the beams in laser interferometry. Most interferometry models are built on the assumption that the laser

beams are purely Gaussian, which is never true in reality. Optical defects, misalignments, cavities with non-matching eigenmodes etc., cause beam distortions that affect the interferometer. Beam distortions can reduce the spatial overlap between the fields, which in turn causes negative effects such as reduced power in the interferometer, extra noise due to unwanted light leaking out through the dark port, degraded sensing and control signals, and squeeze degradations. It is increasingly important to understand the effects of beam distortions in gravitational wave detectors as the sensitivity of the devices increases. Especially following the implementation of squeezed light, as these squeezed states are particularly susceptible to beam distortions.

The gravitational wave detectors, however, are complex systems that can be very challenging to understand as there are plenty of parameters in play simultaneously. Numerical modelling softwares like FINESSE can therefore be powerful tools if used correctly, as they enable studying realistic effects of one parameter at a time, which can be used for exploring the large parameter space of the detectors.

The general aim of this project was to contribute to the commissioning and design processes of gravitational wave detectors. This has been done by performing simulation tasks and analytical investigations myself, with the aim of increasing our knowledge on how spatial distortions affects gravitational wave detectors, and by developing tools and models that enable and facilitate, for myself and others, to perform realistic simulations that accounts for the spatial aspects of laser interferometry.

In particular, chapter 2 shows (by means of simulation) how frequency dependent squeezed light in LIGO is affected by spatial mismatches between the eigenmodes of the squeezer, the filter cavity, and the interferometer. This is of immediate importance as squeezed light currently is being implemented. In addition, we propose a novel

technique for mitigating the negative effects that spatial mismatches have on squeezed light, and we experimentally show that the technique works in the special case where the spatial mismatch is a misalignment. This may be of importance in the future if it turns out to be difficult to mode match the cavity eigenmodes to a satisfactory level.

The work presented in chapter 3, investigates how the length sensing signal for the power recycling cavity in Virgo, is affected by power recycling mirror misalignments. This work had the immediate impact of facilitating the decision of switching from using 132 MHz modulation sidebands to 119 MHz modulation sidebands to control the power recycling cavity during lock acquisition. The bulk of the material presented in this chapter is however, on how to correctly and realistically model a near-unstable cavity (like the Virgo power recycling cavity). This may be of importance during future commissioning and design processes for Virgo.

Chapter 4 describes a model of LIGO Livingston, developed to be able to perform commissioning and design simulations of the alignment sensing system. One of the reasons for building this model is that LIGO Livingston currently is limited by misalignment couplings into the gravitational wave channel at the low end of the gravitational wave bandwidth. The model may be useful in trying to understand the reason for this, and it can be used for simulating the alignment sensing matrix and investigate if there are better way of utilising this information in the control system.

CHAPTER 2

MULTI-SPATIAL-MODE EFFECTS IN SQUEEZED-LIGHT-ENHANCED INTERFEROMETRIC GRAVITATIONAL WAVE DETECTORS

This chapter outlines research done on how spatial mode mismatches affects the frequency dependent squeezed vacuum states that are planned to be injected into the current interferometric gravitational wave detectors in the future. We also propose using multi-spatial-mode squeezed vacuum to increase the robustness to spatial mode mismatches, which is a novel idea in the field of gravitational waves. Most of this work has been published in the scientific article *Multi-spatial-mode effects in squeezed-light-enhanced interferometric gravitational wave detectors* [35], and the work presented in section 2.4 is pending for publication. Both text and figures from these articles have been used verbatim in this chapter.

The current advanced interferometric gravitational-wave detectors, e.g., the Advanced LIGO [17] detectors, are dual-recycled Michelson interferometers with arm cavities, as shown in figure 2.1. One of the limiting noise sources is quantum noise which arises from quantum fluctuations of light. To reduce the quantum noise over a broad-frequency

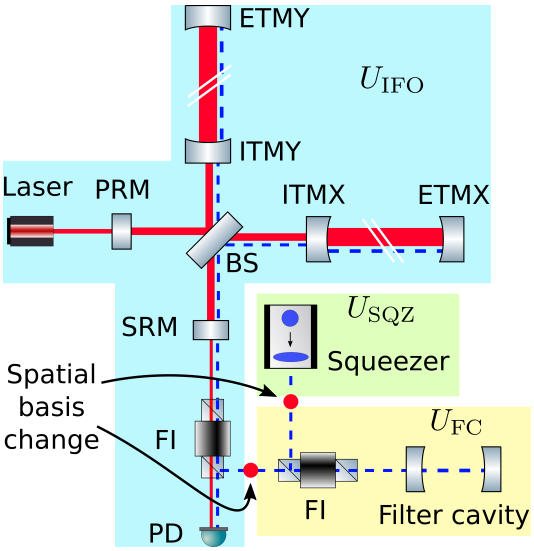

Figure 2.1: The field emitted by the squeezer is reflected off a filter cavity to produce frequency dependent squeezed states. These states are injected into the interferometer through the signal recycling mirror. There are three potentially different spatial eigenbases in this setup: U_{FC} for the filter cavity (yellow background), U_{SQZ} for the squeezer (green), and U_{IFO} for the interferometer (blue), where the background colors indicate which basis that is used where. All the coherent laser power is in the fundamental mode of the interferometer basis.

band, one approach is to inject frequency dependent squeezed vacuum states into the dark port of the interferometer [36, 37]. These states are produced by the combination of a *squeezer* and a *filter cavity*, where the filter cavity generates the frequency dependency [30, 38, 39], such that the phase quadrature is squeezed for high frequencies and the amplitude quadrature is squeezed for low frequencies. This technology can be fitted into the current infrastructure [40, 41], and is planned to be implemented in the next upgrade of the current observatories.

There are several practical imperfections that can influence the performance of this scheme, such as spatial mode-mismatches, optical losses, and phase noise [42, 41, 43]. This chapter focuses on spatial mode-mismatches. Their effects on the squeezing can be categorized into two types. The first type is when a part of the squeezed states in the fundamental mode irreversibly scatters to higher-order modes, which has an effect similar to an optical loss. The second type is when the quantum states are allowed

to coherently couple back and forth between the fundamental mode and higher-order modes. This type requires multiple interfaces where mode-mismatch induced scatterings occur. Particularly, there are two important such interfaces, located between the three components of interest in this work: the squeezer, the filter cavity, and the interferometer — each to a good approximation having its own well-defined spatial mode basis.

Kwee *et al.* [41] studied the combined effect of these two types by considering mode-mismatches at the above mentioned interfaces. In this study, to better understand the effects of these two types separately, we isolate them as much as possible by mode-mismatching one of the three components at a time, i.e., two components are always kept perfectly mode matched to each other. In contrast to reference [41] and to what would be done in practice, the filter cavity is intentionally made to be resonant for higher-order modes within the frequency band of interest. On the one hand, this allows us to further study the interesting coherent scattering effect. On the other hand, it might be relevant in reality for long filter cavities.

In this chapter, we show that broadband squeeze degradation effects, similar to an optical loss, are obtained when the interferometer is mode mismatched to the filter cavity and the squeezer, while the squeezer and the filter cavity are matched, and when the squeezer is mode mismatched to a mode matched filter cavity and interferometer. Squeeze degradations larger than an optical loss, induced by coherent scattering, are obtained when the squeezer and the interferometer are mode matched, while the filter cavity is mode mismatched to both of these. This effect is seen at low frequencies where the fundamental mode is resonant in the filter cavity, and at the resonance frequencies of the higher-order modes.

We also show that the injection of *multi-spatial-mode squeezing*, where two higher-order spatial modes (HG_{02} and HG_{02}) are squeezed in addition to the fundamental mode, in theory can provide robustness to spatial mode-mismatches. The interesting spatial aspects of squeezed states have generated the relatively new field of quantum imaging [44, 45, 46], which has experimentally demonstrated the abilities of both generating squeezed higher-order Gaussian modes [47, 48, 49], and combining different squeezed transverse modes [50]. These are, in principle, the tools needed to produce the multi-spatial-mode squeezing considered in this chapter.

Further, experimental results are presented showing that a field with a squeezed HG_{01} mode, in addition to a squeezed fundamental mode, can mitigate squeeze degradations induced by a misalignment that couples the modes HG_{00} and HG_{01}. In principle, this also proves that multiple-spatial mode squeezing can mitigate the effect of spatial mode mismatches that couple the second order modes and the fundamental mode. However, practical implementation of squeezing both the second order modes independently may be more complicated and therefore require an experimental demonstration of its own.

The outline of this chapter goes as follows. In section 2.1, the effect that spatial mode mismatches have on squeezed light are quantified through simulations using FINESSE , and the results are analysed by using analytical expressions. In section 2.2 we elaborate on the model to show that the injection of squeezed states in multiple spatial modes, in theory, can provide robustness to mode-mismatches, and section 2.3 shows that this remains true for a slightly more realistic model where there are small spatial mode mismatches within the interferometer as well. Section 2.4 experimentally shows that squeezing a first order mode, in addition to the fundamental mode, indeed mitigates the squeeze degradation due to misalignments.

2.1 The effect of spatial mode-mismatches

We now go into the details behind the modeling of how mode-mismatches affects the quantum-noise-limited sensitivity of a squeezed-light-enhanced interferometric gravitational wave detector. Specifically, we start with the description of the optical setup in subsection 2.1.1, and then in subsection 2.1.2, we describe the general framework used to analyze the results. FINESSE [32, 33, 27]—the numerical software that was used to produce the results—uses an equivalent method [51, 52]. A similar framework can also be found in reference [53]. In the later subsections 2.1.3, 2.1.4, and 2.1.5, we look into mode-mismatches between the three components—the squeezer, the filter cavity, and the interferometer.

2.1.1 The optical setup

The optical setup used here is visualized in figure 2.1, and is a simplified and idealized model of an Advanced LIGO detector [17] with frequency dependent squeezed light injected through the dark port. The key parameters of the interferometer are listed in Table 2.1. The frequency dependent squeezing is realized by reflecting the squeezed field off a detuned over-coupled Fabry-Perot cavity. This cavity is frequently referred to as a filter cavity [30, 38, 39]. The filter cavity considered in this work is a linear overcoupled 16 m long confocal optical cavity, based on the one proposed in [40] for near-term upgrade of Advanced LIGO. In this work, the input mirror is lossless, the end mirror is perfectly reflective, and we have assumed that the mirrors are much larger than the beam sizes so that clipping losses are negligible. The values used for cavity detuning and input mirror transmission were obtained by maximizing the broadband sensitivity between 10 Hz and 3 kHz. The radius of curvature for the two mirrors is chosen to make the higher-order modes up to order four resonant within the frequency

band of interest so that the effects of these can be seen, which is of particular interest for the coherent scattering effect. All the used filter cavity parameters are shown in Table 2.2.

Table 2.1: The table shows the interferometer parameters that were used.

Symbol	Parameter	Value
λ_0	Carrier wavelength	1064 nm
P_{arm}	Arm cavity power	0.74 MW
P_{bs}	Power on the beam splitter	5.3 kW
L_{arm}	Arm cavity lengths	3994.5 m
m	Mass of test-mass mirrors	40 kg
L_{src}	Signal recycling cavity length	57 m
T_{srm}	SRM power transmission	0.35

Table 2.2: The table shows the design parameters for the filter cavity used in Sec. 2.1.

Symbol	Parameter	Value
L_{fc}	Length	16.0 m
R_{C}	Mirror radius of curvature	15.999 m
T_{in}	Input mirror transmission	61 ppm
R_{in}	Input mirror reflection	1-T_{in}
R_{end}	End mirror reflection	1
FSR	Free spectral range	9.37 MHz
$\Delta/2\pi$	Detuning	46.18 Hz
$\gamma_{\text{fc}}/2\pi$	Half-width	45.49 Hz
δ_f	Mode-separation	$(1+4\times10^{-5})\frac{\text{FSR}}{2}$ Hz

We have three components to mode-mismatch to each other: the interferometer, the filter cavity, and the squeezer. The mode-mismatch between the interferometer and the filter cavity is generated by displacing a mode matching lens along the optical axis. For the squeezer component, FINESSE allows us to freely specify the complex beam parameter of the field that is emitted, and we used this feature to control the mode matching of the squeezer.

2.1.2 The mathematical framework

The spatial distribution of the field within the interferometer can be expanded in one common interferometer eigenbasis $U_n^{\mathrm{IFO}}(x, y, z)$. Specifically, the sideband field with frequency $\omega_0 \pm \Omega$ (ω_0 is the carrier frequency of the laser) reads:

$$\hat{E}(\omega_0 \pm \Omega, x, y, z) = \sum_{n=0}^{N} c_n \hat{a}_{\omega_0 \pm \Omega, n} U_n^{\mathrm{IFO}}(x, y, z) \tag{2.1}$$

Here $\hat{a}_{\omega_0 \pm \Omega, n}$ are the annihilation operators for the upper and lower sidebands of the nth mode, c_n is the relative weight of the nth mode satisfying $\sum_{n=0}^{\infty} |c_n|^2 = 1$, N denotes the number of modes included in the model, z is the coordinate along the optical axis, and x and y are the transverse coordinates. Similarly, the eigenbases of the filter cavity and the squeezer are denoted by U_n^{FC} and U_n^{SQZ}, respectively. These are the three eigenbases used to describe the spatial distribution of the field within the optical setup. Which eigenbasis is used where is indicated by the background colors in figure 2.1, and the red dots indicate where the basis changes take place. Scattering between modes labeled by different numbers n occurs when changing basis from U_n^{SQZ} to U_n^{FC} and when changing basis from U_n^{FC} to U_n^{IFO}, if the complex beam parameters of the bases are different.

In this chapter, we use the two-photon formalism [28, 29, 54] to model the quantum noise. In this formalism, the key quantitates are (i) the amplitude and phase quadrature operators which are defined as

$$\hat{a}_1(\Omega) = \frac{\hat{a}_{\omega_0+\Omega} + \hat{a}^\dagger_{\omega_0-\Omega}}{\sqrt{2}}, \ \hat{a}_2(\Omega) = \frac{\hat{a}_{\omega_0+\Omega} - \hat{a}^\dagger_{\omega_0-\Omega}}{\sqrt{2}\, i} \tag{2.2}$$

and (ii) the transfer matrix relating the quadrature operators of the fields at different locations. In our case, we care about higher-order modes where the quadrature

operators can be represented in terms of a column vector of length $2N$:

$$\mathbf{a} = \bigoplus_{n=0}^{N} \mathbf{a}_n(\Omega) \tag{2.3}$$

with each pair of quadrature operators for mode n being defined as

$$\mathbf{a}_n(\Omega) = \begin{bmatrix} \hat{a}_{1,n}(\Omega) & \hat{a}_{2,n}(\Omega) \end{bmatrix}^{\mathrm{T}}. \tag{2.4}$$

The field that enters the interferometer can be related to the field entering the squeezer through

$$\mathbf{a}_{\mathrm{IFO}} = \mathcal{K}_2 \mathcal{T} \mathcal{K}_1 \mathcal{S}\, \mathbf{a}_{\mathrm{SQZ}}, \tag{2.5}$$

Here, $\mathcal{S}$ is the squeezing matrix, $\mathcal{T}$ is the filter cavity transfer matrix, $\mathcal{K}_1$ describes the basis change from U_n^{SQZ} to U_n^{FC}, and $\mathcal{K}_2$ describes the basis change from U_n^{FC} to U_n^{IFO}. These matrices are described as follows.

The joint squeezing matrix $\mathcal{S}$ is given by the direct sum of the individual squeezing matrices for every spatial mode in the field:

$$\mathcal{S} = \bigoplus_{n=0}^{N} \mathcal{S}_n. \tag{2.6}$$

The squeezing matrix $\mathcal{S}_n$ for spatial mode n is given by

$$\begin{bmatrix} \cosh r_n + \sinh r_n \cos 2\varphi_n & \sinh r_n \sin 2\varphi_n \\ \sinh r_n \sin 2\varphi_n & \cosh r_n - \sinh r_n \cos 2\varphi_n \end{bmatrix}, \tag{2.7}$$

where r_n and φ_n are the squeeze factor and angle, respectively. In later subsections, the states in the fundamental mode are squeezed by 10 dB while all higher order modes

contain pure vacuum states. That is, $r_0 = (2\log_{10}\mathrm{e})^{-1}$ and $r_n = 0$ for all $n > 0$. The angle φ_0 is optimized such that the high-frequency shot noise is maximally reduced. The filter cavity then takes care of correctly rotating the squeezed states for the rest of the frequency components.

The matrix $\mathcal{K}$ describing a basis change between two spatial mode bases is given by

$$\mathcal{K} = \begin{bmatrix} \mathcal{K}_{0,0} & \cdots & \mathcal{K}_{0,k} & \cdots & \mathcal{K}_{0,N} \\ \vdots & \ddots & \vdots & \ddots & \vdots \\ \mathcal{K}_{n,0} & \cdots & \mathcal{K}_{n,k} & \cdots & \mathcal{K}_{n,N} \\ \vdots & \ddots & \vdots & \ddots & \vdots \\ \mathcal{K}_{N,0} & \cdots & \mathcal{K}_{N,k} & \cdots & \mathcal{K}_{N,N} \end{bmatrix}, \tag{2.8}$$

where each entry $\mathcal{K}_{n,k}$ is a 2×2 matrix given by

$$\mathcal{K}_{n,k} \equiv \kappa_{nk} \begin{bmatrix} \cos\beta_{nk} & -\sin\beta_{nk} \\ \sin\beta_{nk} & \cos\beta_{nk} \end{bmatrix}. \tag{2.9}$$

Here, κ_{nk} is the coupling magnitude from mode number k in the old basis to mode number n in the new basis, and β_{nk} is the corresponding coupling phase.

Expressed in the spatial basis U_n^{FC}, the reflection off the filter cavity is given by

$$\mathcal{T} = \bigoplus_{n=0}^{N} \mathcal{T}_n(\Omega), \tag{2.10}$$

where the spatial mode n undergoes a phase change specified by

$$\mathcal{T}_n(\Omega) = \mathcal{A}_2 \begin{bmatrix} r_n(\Omega) & 0 \\ 0 & r_n^*(-\Omega) \end{bmatrix} \mathcal{A}_2^{-1}. \tag{2.11}$$

The transfer function for a sideband in spatial mode n is given by

$$r_n(\Omega) = \frac{\mathrm{e}^{-i\phi_n(\Omega)} - \sqrt{R_{\mathrm{in}}}}{\sqrt{R_{\mathrm{in}}}\mathrm{e}^{-i\phi_n(\Omega)} - 1}, \tag{2.12}$$

where

$$\phi_n(\Omega) = \left[\frac{2L}{c}(\Omega + \Delta) - q_n\psi_{\mathrm{rt}}\right] \tag{2.13}$$

and R_{in} is the input mirror power reflectivity, Δ is the cavity detuning, L is the macroscopic cavity length, c is the speed of light, ψ_{rt} is the round-trip Gouy phase and q_n is the order of the mode n. The matrix

$$\mathcal{A}_2 = \frac{1}{\sqrt{2}} \begin{bmatrix} 1 & 1 \\ -i & i \end{bmatrix} \tag{2.14}$$

is used to transform the transfer function for the sidebands to that for the quadratures.

2.1.3 Mode-mismatched interferometer

In this scenario, the interferometer is mode-mismatched to both the squeezer and the filter cavity, while the squeezer and the filter cavity are kept mode matched to each other. To generate this mode-mismatch, one of the lenses used to mode match the filter cavity to the interferometer is displaced along the optical axis. The resulting quantum-noise-limited sensitivity is shown in figure 2.2, while figure 2.3 shows the

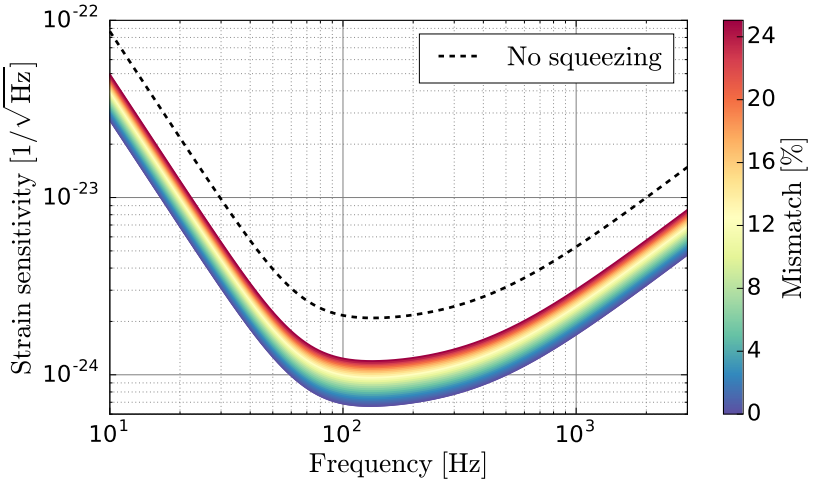

Figure 2.2: The figure shows the quantum-noise-limited sensitivity for various levels of mode-mismatch between the interferometer and the filter cavity. The squeezer is kept mode matched to the filter cavity.

same data but expressed in terms of improvement over the nonsqueezed case. The dip

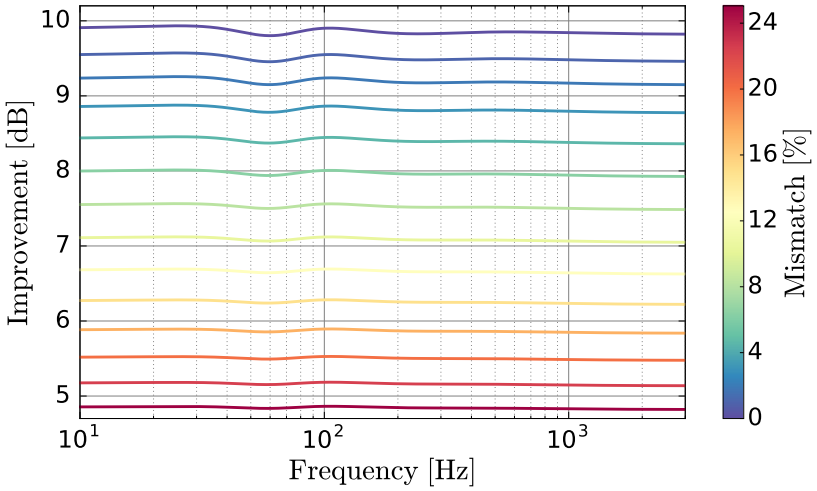

Figure 2.3: The figure shows the same information as figure 2.2, but here the data is expressed in dB relative to the non-squeezed case. This more clearly shows that this type of mismatch gives rise to a broadband squeeze degradation similar to an optical loss.

in improvement around 70 Hz is a consequence of that one cannot achieve a perfect broad-frequency band noise reduction by using only one filter cavity [30]. However, when operating with a tuned signal recycling cavity, as done here, one filter cavity still performs very well [55, 56]. Since we are using realistic mirror losses inside the interferometer, the sensitivity improvement does not reach exactly 10 dB even when

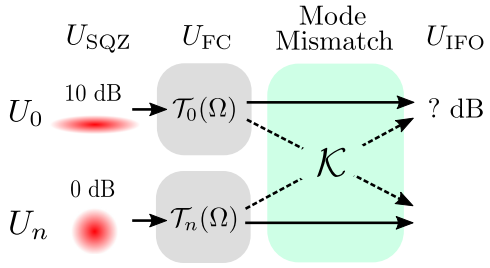

Figure 2.4: The figure shows the effect of mode-mismatching the interferometer to the filter cavity and the squeezer. Initially, the vacuum noise in the spatial mode U_0 is squeezed by 10 dB, while the arbitrary higher-order mode U_n contains pure vacuum noise. The noise fields in the two spatial modes mix after being subjected to the frequency and mode dependent rotation of the squeeze angle when reflected off the filter cavity.

all three components are perfectly mode matched. The reason for the broad-frequency band squeezing degradation is best explained by using the analytics developed above. Since the squeezer and the filter cavity are mode matched, and assuming that the self-coupling phases in equation 2.9 are $\beta_{kk} = 0$, the basis change matrix $\mathcal{K}_1$ in equation 2.5 becomes the identity matrix. This assumption does not reduce the generality as any self-coupling phase could be compensated for by adjusting the initial squeeze angle. Equation 2.5, describing the quantum field injected into the interferometer, is then reduced to

$$\mathbf{a}_{\mathrm{IFO}} = \mathcal{K}\mathcal{T}\mathcal{S}\,\mathbf{a}_{\mathrm{SQZ}}, \tag{2.15}$$

which is visualized in figure 2.4. The only frequency dependent process that the field undergoes is the interaction with the filter cavity, which is described by equation 2.10. When this process takes place, all the squeezed states are in the fundamental mode and therefore undergo the correct rotation $T_0(\Omega)$. The phase changes of the pure vacuum states in the higher-order modes $T_n(\Omega)$ are unimportant, as these just rotate circular symmetric probability distributions around their symmetry axes.

The mode-mismatch-induced basis change $\mathcal{K}$ makes the fundamental mode exchange some squeezed states for pure vacuum states with the higher-order modes. This makes

the fundamental mode of the interferometer eigenbasis less squeezed for all frequencies, and has the same effect as an optical loss. That is, for small coupling coefficients κ_0, where

$$\kappa_0^2 = \sum_{n=1}^{N} \kappa_{0n}^2 \tag{2.16}$$

is the total power coupling magnitude for scattering away from the fundamental mode, the quantum noise in the interferometer scales as

$$(1 - \kappa_0^2)\mathrm{e}^{-2r_0} + \kappa_0^2. \tag{2.17}$$

2.1.4 Mode-mismatched filter cavity

Just as above, the filter cavity is spatially mode-mismatched to the interferometer, but here the squeezer is kept mode matched to the interferometer instead of to the filter cavity.

In this case, there are nontrivial spatial basis changes before and after the filter cavity that give rise to couplings between different spatial modes. Since the squeezer and the interferometer are mode matched to each other, the second basis change is the inverse of the first, thus, equation 2.5 becomes

$$\mathbf{a}_{\mathrm{IFO}} = \mathcal{K}^{-1}\mathcal{T}\mathcal{K}\mathcal{S}\,\mathbf{a}_{\mathrm{SQZ}}. \tag{2.18}$$

This process is visualized in figure 2.5.

Due to the mode-mismatch $\mathcal{K}$ between the squeezer and the filter cavity, the field incident on the filter cavity input mirror has a part of its squeezed states located in

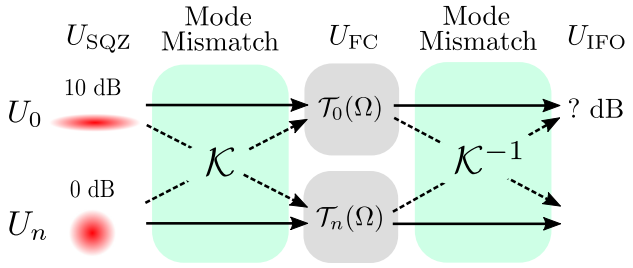

Figure 2.5: The figure shows the effect of mode-mismatching the filter cavity to the squeezer and the interferometer. The noise fields in the two spatial modes mix twice, with a frequency and mode dependent rotation of the squeeze angle in between due to the filter cavity. Since the squeezer and the interferometer are mode matched, the two mixing operations are the inverse of each other.

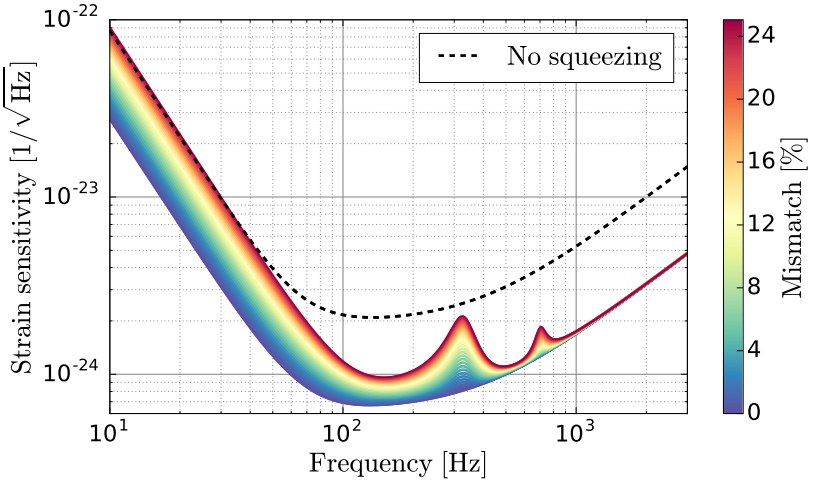

Figure 2.6: The figure shows the quantum-noise-limited sensitivity as a function of gravitational wave frequency. The squeezer and the interferometer are kept mode matched to each other, and the colours indicate the level of mismatch between these and the filter cavity. Around the resonance frequencies of the involved spatial modes, squeeze degradations are seen due to coherent scattering between the spatial modes.

higher-order modes. If these higher-order modes experience phase shifts different from the phase shift of the fundamental mode when reflected off the filter cavity (i.e., if $T_n(\Omega) \neq T_0(\Omega)$), then the mode-mismatch between the filter cavity and the interferometer, $\mathcal{K}^{-1}$, enables for these now wrongly rotated squeezed states to mix back in with the squeezed states in the fundamental mode. If the wrongly rotated states are antisqueezed, this coherent scattering process is worse than an optical loss. In Figs. 2.6 and 2.7, this coherent scattering effect can be seen in two different regions: at low frequencies, where the fundamental mode is nearly resonant while the higher-order

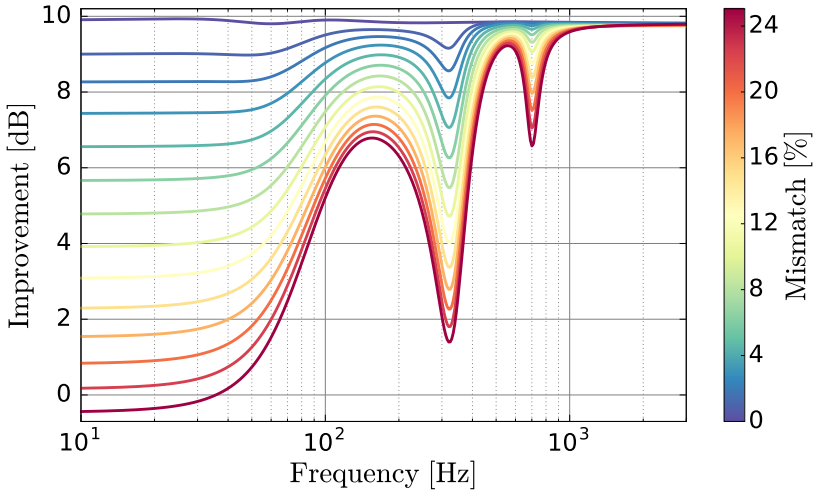

Figure 2.7: The figure shows the same information as figure 2.6, but here the y-axis is in units of dB, where the case without any squeezed field is used as the reference.

modes are off resonance, and at about 300 Hz and 700 Hz where the second-order and fourth-order modes are resonant while the fundamental mode is not. The reason that the second-order and fourth-order modes show up is that the mode-mismatch was generated by offsetting the waist size and displacing the waist position of the beam, which only generates nonzero couplings between modes with even mode-order spacing. Since the couplings decrease with increasing mode-order spacing, we only included modes up to order four in our simulations.

For a small mode-mismatch, and for the worst case higher-order-mode rotations, the quantum noise in the interferometer scales as

$$\mathrm{e}^{-2r} + 4(1 - \mathrm{e}^{-2r})\kappa_0^2. \tag{2.19}$$

See Appendix A for a derivation of this formula. For large squeeze magnitudes, this is a factor of 2 worse than the effect of a corresponding optical loss. It should be mentioned that the filter cavity was deliberately designed to have this small mode spacing so that we could see the effect of higher-order mode resonances. If this 16 m filter cavity would be implemented in LIGO, it would be designed such that the higher-order modes are resonant well outside the frequency range of interest. However, this might not be

possible for much longer filter cavities, e.g., as proposed for the Einstein Telescope [57].

For high frequencies, neither the fundamental mode nor the higher-order modes are resonant, thus $T_n(\Omega) = T_0(\Omega)$, and the squeezed field is consequently unaffected by this mode-mismatch.

2.1.5 Mode-mismatched squeezer

Here we consider the case where the squeezer is mode-mismatched to both the filter cavity and the interferometer, while the last two are kept mode matched to each other. This means that the basis change between the squeezer and the filter cavity generally has nonzero couplings between different spatial modes, while the matrix performing the basis change in between the filter cavity and the interferometer becomes the identity matrix. Thus, equation 2.5 becomes

$$\mathbf{a}_{\mathrm{IFO}} = \mathcal{T}\mathcal{K}\mathcal{S}\,\mathbf{a}_{\mathrm{SQZ}}, \tag{2.20}$$

which is visualized in figure 2.8. The effect is the same in Sec. 2.1.3, thus the result can be seen in Figs. 2.2 and 2.3. In contrast to the case in Sec. 2.1.3, there are indeed squeezed states in the higher-order modes that have incorrect rotations due to the filter cavity. But since these are not allowed to couple back to the fundamental mode again, this does not contribute to any extra quantum noise.

2.2 Robustness to mode-mismatches through squeezed higher-order modes

In this section, we show that the injection of squeezed states in multiple spatial modes potentially can provide robustness to mode-mismatches. This requires that the initial

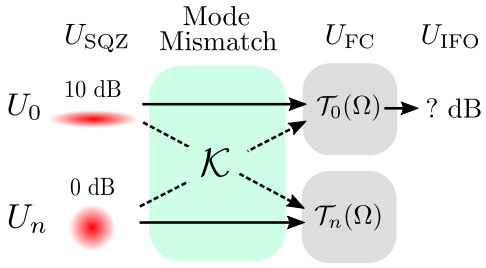

Figure 2.8: The figure shows the effect of mode-mismatching the Squeezer to the FC and the Interferometer. The noise fields in the two spatial modes mix before being subjected to the frequency and mode dependent rotation of the squeeze angle when reflected off the FC.

orientation of the squeezing ellipses can be independently optimized for each spatial mode, which would be challenging to achieve in practice due to the degenerate resonance conditions of the second order modes. Further, the field from three different squeezers would have to be superimposed into one by using mode-selecting cavities.

In subsection 2.2.1 the mode-mismatched interferometer is revisited (see Sec. 2.1.3), but this time three spatial modes are squeezed instead of just the fundamental mode. Subsection 2.2.2 provides a simple analytic test of the principle of using multiple squeezed modes to improve the robustness to spatial mode mismatches.

2.2.1 Mode-mismatched interferometer

The same mode-mismatch is considered as in Sec. 2.1.3, that is, the interferometer is mode-mismatched to the filter cavity and the squeezer, while the filter cavity and the squeezer are kept mode matched to each other. Therefore, equation 2.15 applies here as well, but with some alterations to the squeezing matrix $\mathcal{S}$ and to the filter cavity transfer matrix $\mathcal{T}$, as described below.

We squeezed the Hermite-Gaussian modes HG_{02} and HG_{20}, in addition to the fundamental mode, as these two second order modes have the strongest couplings to the fundamental mode, as mentioned in Sec. 2.1.4. All three states are squeezed by 10

dB. The two extra modes are labeled $n = 1$ and $n = 2$, thus, the squeeze magnitudes in the squeezing matrix $\mathcal{S}$ (equation 2.7) becomes $r_n = (2 \log_{10} \mathrm{e})^{-1}$ for $n \in \{0, 1, 2\}$, and $r_n = 0$ for $n > 2$. Further, for each level of mode-mismatch the initial squeeze angles φ_n for $n \in \{0, 1, 2\}$ are independently optimized to maximize the sensitivity (or equivalently, to minimize the quantum noise). This optimization is needed to correctly compensate for the phases β_{0k}, $k \in \{1, 2\}$, that are picked up when the squeezed higher order modes couple into fundamental mode due to the mode-mismatch-induced basis change $\mathcal{K}$ (equation 2.8).

To acquire the optimal frequency dependent rotation for the squeezed states in all three spatial modes, the filter cavity was made critical by changing the radius of curvature of the two filter cavity mirrors to 16 m. This gives a round-trip Gouy-phase of π, hence, the second order modes have the same resonance condition as the fundamental mode, and therefore pick up the same phase shift modulo 2π when subjected to filter cavity transfer matrix $\mathcal{T}$. This can be seen by setting $\psi_{\mathrm{rt}} = \pi$, $q(0) = 0$ and $q(1) = q(2) = 2$ in equation 2.13.

The results for two different levels of mode-mismatches are shown in figure 2.9, and are presented in terms of sensitivity improvement over the no-squeezing case. The figure also includes the corresponding traces from subsection 2.1.3 for comparison. One can see that for 5 % mode-mismatch the sensitivity is increased with about 1.5 dB compared to the case when only the fundamental mode is squeezed, and that most of the mode-mismatch-induced squeezing degradation is recovered by squeezing the two extra spatial modes. There are two reasons for this:

(i) In the previous section, pure vacuum states from the second-order modes mixed in with the squeezed states in the fundamental mode due to the mode-mismatch. Now, correctly rotated squeezed states mix in instead.

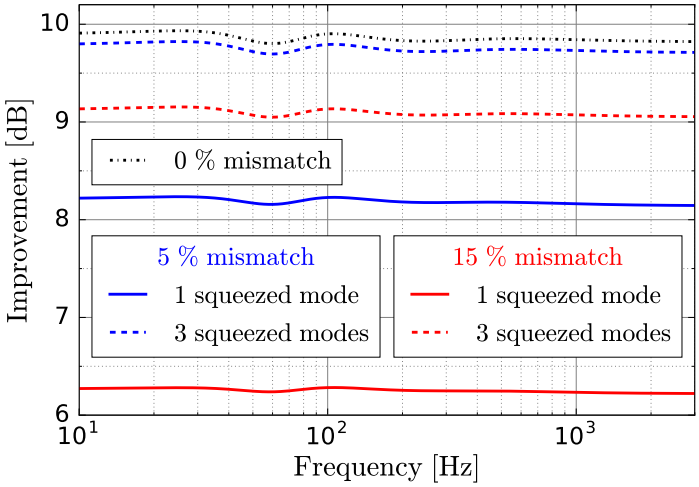

Figure 2.9: The figure shows the improvement in dB that we obtain by squeezing the vacuum fluctuations that enters through the signal recycling cavity. The dashed traces indicates the improvement when squeezing 3 spatial modes, and the solid lines indicate the improvement when squeezing 1 spatial mode. This is shown for two different levels of mode-mismatch between the interferometer and the filter cavity.

(ii) The couplings between the fundamental mode and the higher-order modes that carry pure vacuum states are small for this level of mode-mismatch.

For the larger mode-mismatch of 15 %, the sensitivity gain is also larger—about 3 dB. This is because the coupling magnitudes between the fundamental mode and the second-order modes have increased. However, the sensitivity does not rise to around the mode matched case, as the fundamental mode has significant couplings to pure-vacuum-state-carrying higher-order modes. The results show that squeezing the two extra spatial modes provide robustness to this particular mode-mismatch in our model.

2.2.2 Theoretical test of principle

In this subsection we provide a theoretical test of principle for multi-spatial-mode squeezing by injecting two squeezed quantum fields into a Mach-Zehnder interferometer, as seen in figure 2.10. The setup of this theoretical experiment consists of two squeezers—one for each incoming field—and two mixing points with a generic propaga-

tion in between. The test originated from the idea of testing if the benefits of squeezing higher-order modes could be downgraded or even rejected, if we allow propagations and scatterings that are more general in nature than the couplings between the even-order spatial modes studied in the previous subsection. The test was performed as follows:

(i) The parameters of the system are independently assigned random values drawn from uniform probability distributions within realistic and physically valid intervals. These parameters are: the beam splitters' reflection coefficients and microscopical offsets along their surface normals; the macroscopical and microscopical propagation phases; and the readout quadrature. Here, microscopical refers to distances smaller than the carrier wavelength, and macroscopical refers to distances of any magnitude, but of integer multiples of the carrier wavelength.

(ii) The upper input field is squeezed by 10 dB and the lower input field remains pure vacuum, as seen in the left part of figure 2.10. The initial squeeze angle is optimised to yield maximum squeezing (minimum noise) in the upper output path in the readout quadrature, and the resulting readout squeezing is stored.

(iii) The second squeezer is switched on so that both fields are squeezed by 10 dB, as seen in the right part of figure 2.10. The initial squeeze angle for the lower field is then also optimised to yield maximum squeezing in the upper output path in the readout quadrature, and the resulting value is stored.

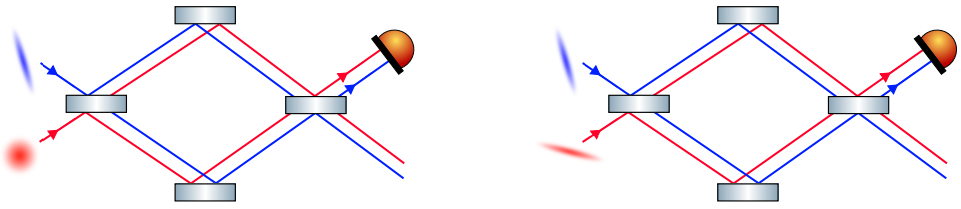

Figure 2.10: The figure shows Mach-Zehnder interferometers used to mix two quantum fields. In the left figure, a squeezed vacuum field is mixed with pure vacuum, and in the right figure, two independent squeezed vacuum fields are mixed. The photo detector indicates that the upper output path is the one of interest.

(iv) Repeat (i) to (iii) 10,000 times, each with a different set of randomly chosen parameters.

The result is shown as a histogram in figure 2.11. The blue distribution show the data obtained when using one squeezed field in step (ii), and the red bar is the result obtained when both fields are squeezed in step (iii). The height of bar number k is given by

$$h_k = \frac{n_k}{Na} = \frac{n_k}{1000} \tag{2.21}$$

where n_k is the number of counts within the limits of bar number k, a is the width of the bars in dB, and $N = \sum_k n_k$ is the total number of counts. The shape of the blue distribution is not important by itself, as it strongly depends on how the bins are constructed and on how the random sets of parameters are drawn. More important is that the blue and red distributions together show that for any set of parameter values, one can always obtain 10 dB of output squeezing as long as the initial squeeze angles can be independently optimised.

The rest of this subsection is focused on describing the model that was used in more detail. The system can be described by the framework from section 2.1.2, with $N = 1$ as there are only two fields in this setup. The upper (lower) field, and the operations acting on the upper (lower) field, are everywhere in the setup labeled by $n = 0$ ($n = 1$). The relation between the output fields and the input vacuum fields is given by equation 2.5, however, the transfer matrices $\mathcal{K}_1$, $\mathcal{K}_2$ and $\mathcal{T}$ are modified as follows.

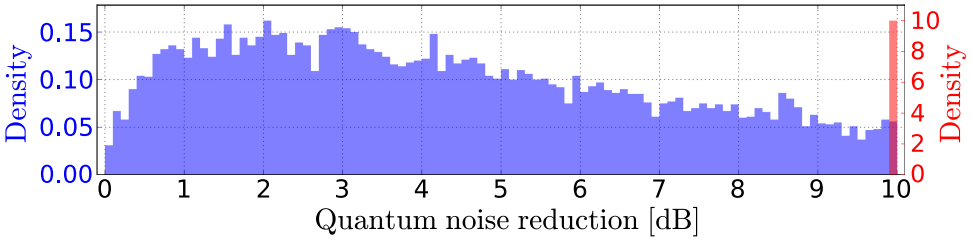

Figure 2.11: The figure shows the normalised number of counts for various output squeeze intervals when mixing squeezed vacuum with pure vacuum (blue), and when mixing two squeezed vacuum fields (red). The squeeze angles have, for both distributions, been optimised to minimise the noise.

Each lossless beam splitter can be represented by

$$\mathcal{K}_i = \begin{bmatrix} r_i \cos\beta_i & -r_i \sin\beta_i & t_i & 0 \\ r_i \sin\beta_i & r_i \cos\beta_i & 0 & t_i \\ t_i & 0 & -r_i \cos\beta_i & -r_i \sin\beta_i \\ 0 & t_i & r_i \sin\beta_i & -r_i \cos\beta_i \end{bmatrix} \tag{2.22}$$

where $r_i \in [0.7, 1]$ is the reflection coefficient, t_i is the transmission coefficient satisfying $t_i^2 = 1 - r_i^2$, and $\beta_i \in [-\pi, \pi]$ is the phase shift due to the displacement of the beam splitter along its surface normal.

The propagation $\mathcal{T}$ consists of two independent paths of lengths $D_n = L_n + \delta L_n$, where $|\delta L_n| < \lambda_0$ and $L_n = k_n \lambda_0$ with $k_n \in \mathbb{N}$. Thus, the transfer matrices for paths $n = 0, 1$ are given by

$$\mathcal{T}_n(\Omega) = \mathrm{e}^{-i\theta_n} \begin{bmatrix} \cos\phi_n & \sin\phi_n \\ -\sin\phi_n & \cos\phi_n \end{bmatrix}. \tag{2.23}$$

Here,

$$\theta_n = \frac{\Omega L_n}{c} \in [0, \pi] \tag{2.24}$$

is the phase picked up due to the macroscopical length L_n, and

$$\phi_n = \frac{\omega_0 \delta L_n}{c} \in [-\pi, \pi] \tag{2.25}$$

is the phase shift induced by the microscopical length δL_n.

2.3 A more realistic Advanced LIGO model

To get a hint of how mode-mismatches inside the interferometer affect the multi-spatial-mode squeezed field, we here consider a model of an advanced LIGO detector that includes small mode-mismatches between the cavities inside the interferometer.

There are two important differences compared to the model described in Sec. 2.1. The first one is that the asymmetries between the two transverse spatial directions are included in the model, which gives rise to mode-mismatches that are small, but not negligible. These asymmetries show up because of nonzero angles of incidence in combination with spherical mirrors. The second important difference is that an Advanced LIGO output mode cleaner (see section 1.3.5) has been added to the model. The reason for this is that some fraction of the coherent laser power is in higher-order modes due to the internal mode-mismatches. Without the output mode cleaner, higher-order modes of the quantum field are allowed to beat with the higher-order modes of the coherent carrier field. This creates noise that would not be present with the output mode cleaner included.

The simulation was performed by mode-mismatching the filter cavity to the output mode cleaner by varying the position of a mode matching lens along the optical axis. This mode matching lens is located between the filter cavity and the injection point

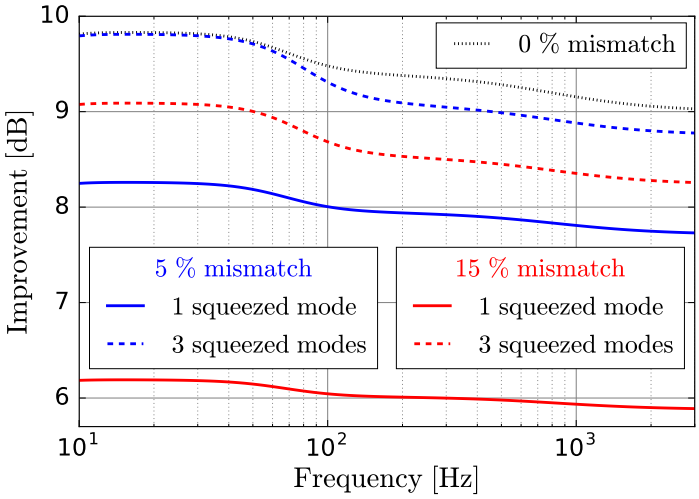

Figure 2.12: The figure shows the improvement in quantum-noise-limited sensitivity over the nonsqueezed case, both for a single squeezed spatial mode (solid lines) and for multiple squeezed spatial modes (dashed lines). The blue and red traces are for mode-mismatch levels between the interferometer and the filter cavity of 5 % and 15 %, respectively. The squeezer is kept mode matched to the filter cavity. The black dotted trace indicates the improvement when the filter cavity and the output mode cleaner are near perfectly mode matched.

for the squeezed field. The squeezer was kept mode matched to the filter cavity. We computed the quantum-noise-limited-sensitivity in the frequency band of interest for two levels of mode-mismatches. This was done both for a squeezer that emits one and three squeezed spatial modes. The resulting improvements over the no-squeezing case are shown in figure 2.12. The behavior at low frequencies is identical to the result obtained with the simpler model considered in Sec. 2.2. At high frequencies, the squeezed field experiences a slightly larger degradation. The reason for this is likely the small internal mismatches in the interferometer, however, further investigation is needed to conclude this. Moreover, we can conclude that the internal mode-mismatches included in this model are too small to give rise to any large effects. Future work aims at systematically studying the impact of internal mode-mismatches due to, e.g., thermal lensing.

2.4 Experimental verification of multi-spatial-mode squeezing

In an experimental setup, we show that most of squeezing that is lost from the fundamental mode due to a mode mismatch, here a misalignment, can be regained by squeezing the TEM_{01} in addition to the fundamental. This experiment is detailed in [58], and a summary is given in this section. The experimental setup is shown in figure 2.13. Two squeezed-light sources are used: S_{00} squeezes the fundamental mode

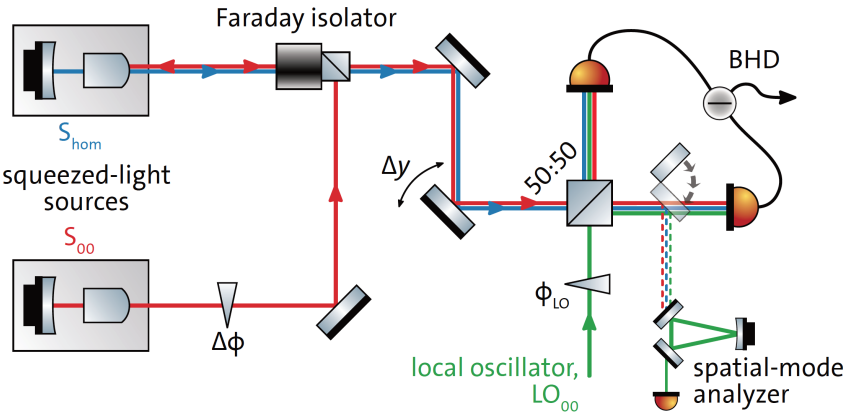

Figure 2.13: The figure shows the experimental setup used for verifying that squeezing multiple spatial modes can mitigate spatial mode mismatch induced squeeze degrations. The system has two squeezers, S_{00} and S_{hom} that squeeze the HG_{00} mode and the HG_{01} mode, respectively. The fields from these two squeezers are superimposed using a Faraday isolator, and propagated to a balanced homodyne dectector. The output of the homodyne detector is used to produce a power spectra at a sideband frequency of 5 MHz.

by 5.8 dB, and S_{hom} squeezes the HG_{01} mode by 4.8 dB. To superimpose the fields produced by the two squeezers, the field from S_{00} is sent through a Faraday isolator and then reflected off the S_{hom} cavity. In addition, there is an piezo-mounted mirror between the squeeze-light sources that can shift the relative phase between the two squeezed fields, which is necessary to obtain the optimal rotation of the squeeze ellipses at the readout. The combined field is then sent to a balanced homodyne detector where it is overlapped with a local oscillator that is in the fundamental mode HG_{00}. The balanced homodyne detector consists of a 50:50 beam splitter and two photodetectors

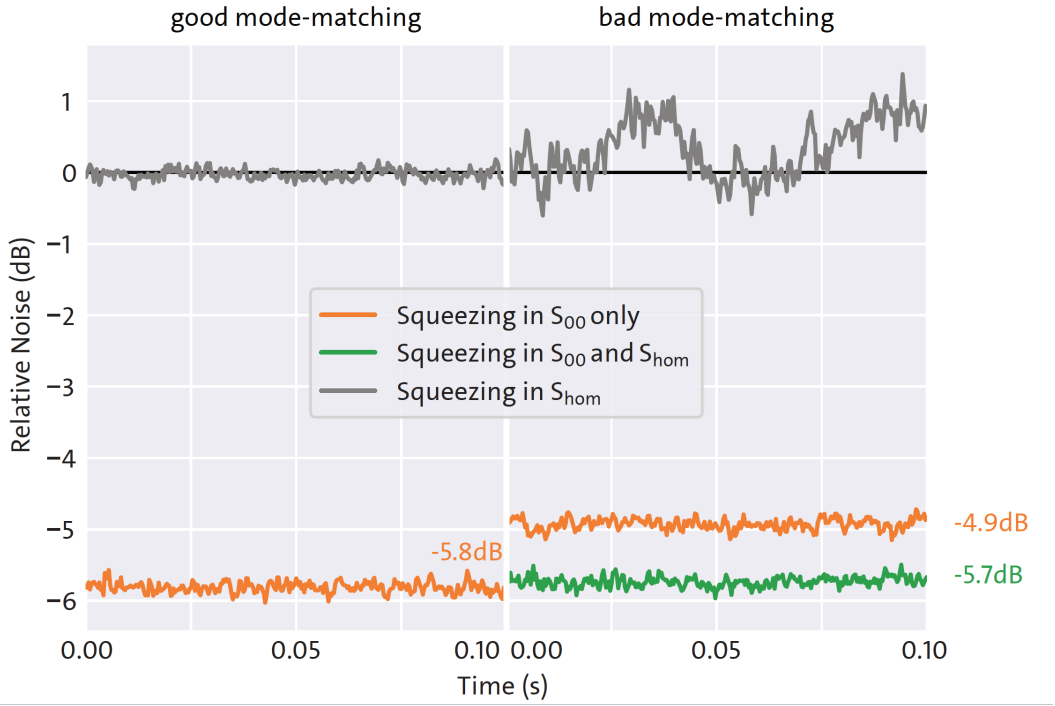

Figure 2.14: The left part shows the squeeze magnitudes for the aligned case. The obtained readout squeezeing in the fundamental mode is 5.8 dB, while the readout in the TEM_{01} mode show pure vacuum noise. In the right part the beam has been misaligned and we see that this results in a lower magnitude of squeezing in the fundamental mode (orange trace). After the HG_{01} squeezer (4.8 dB) has been engaged however, almost all of the readout squeezing in the fundamental mode is recovered (green trace).

that measure the power in the two beam splitter output paths. The measurements are subtracted and then a power spectrum is produced using a spectral analyser at a 5 MHz sideband frequency. The experiment was then performed in the following way:

(i) Firstly, only the squeezer S_{hom} is engaged, which generates pure vacuum noise, as seen from the grey trace in the left part of figure 2.14. This is because there is no spatial overlap between the squeezed HG_{01} mode and the local oscillator in the HG_{00} mode. Secondly, also the S_{00} squeezer is engaged, which yields a noise that is decreased by 5.8 dB, as shown from the orange trace in the left part of figure 2.14.

(ii) The squeezed field is misaligned by an angle Δy using the steering mirror between the Faraday isolator and the beam splitter of the homodyne detector. This creates

nonzero couplings between the fundamental mode and the HG_{01} mode. Now, when only the S_{hom} squeezer is engaged, a small amount of squeezing is shown by the grey trace in the right part of figure 2.14. The squeeze level is small since only a fraction of the squeezed HG_{01} mode scatters to the fundamental mode as the misalignment angle Δy is small. The phase of the local oscillator was swept to generate this trace in order to also show the anti-squeezing, as this is seen more clearly. When only the squeezer HG_{00} is engaged, the orange trace in the right part of figure 2.14 is produced, which shows 4.9 dB of squeezing. Thus, the misalignment has reduced the measured squeezing by 0.9 dB. When both squeezers are engaged however, the squeezing level is measured to be 5.7 dB, thus almost all of the squeezing that was lost due to the misalignment is recovered by adding the S_{hom} squeezer.

2.5 Conclusions

In this chapter, we have quantified and described how squeezed-light-enhanced interferometric gravitational-wave detectors are affected by spatial mode-mismatches between the interferometer, the filter cavity, and the squeezer. We have shown that spatial mode-mismatches potentially can cause significantly larger squeezing degradations than a pure optical loss, if multiple mode-mismatches allow squeezed states to coherently scatter back and forth between the fundamental mode and higher order modes. We can conclude that even with relatively large mode-mismatches, the injection of frequency dependent squeezed light is beneficial in our model.

Further, we have shown that the injection of a field with squeezed states, not only in the fundamental mode, but also in the second-order Hermite-Gaussian modes HG_{02} and HG_{20}, potentially can provide resilience to spatial mode-mismatches. This scheme requires independent optimization of the squeeze angles for all three involved spatial

modes, which can be challenging to implement. We experimentally show that the proposed multi-spatial squeeze scheme works when the mismatch is a misalignment, where the additional squeezed mode is a HG_{01}.

Further studies of how combinations of external and intra-interferometer spatial mode-mismatches affect the performance of squeezed light are needed to better understand how squeezed light would perform in gravitational wave detectors.

CHAPTER 3

LENGTH SENSING MODELLING FOR ADVANCED VIRGO

This chapter outlines modelling work on how the Advanced Virgo power recycling cavity length (PRCL) sensing signal performs when the power recycling mirror (PR) is misaligned. PRCL is defined as

$$\mathrm{PRCL} = l_{\mathrm{P}} + \frac{l_{\mathrm{N}} + l_{\mathrm{W}}}{2}, \tag{3.1}$$

where l_{P} is the optical path length between the highly reflective (HR) surface of PR to the HR-surface of the beam splitter (BS), l_{N} is the optical path length between the HR-surface of the BS and the HR-surface of the mirror NI, and l_{W} is the optical path length between the HR-surface of the BS and the HR-surface of the mirror WI. This work has mainly been carried out by using the simulation software FINESSE [32, 33, 27] accompanied with its Python wrapper PyKat [34]. The used model of Advanced Virgo is visualised in figure 3.1, and was kept as close as possible to the then current state of the interferometer.

To operate a gravitational wave detector in science mode, all the degrees of freedom need to be well controlled and kept at their operating points. This controlled state

is referred to as lock, and the process of bringing the detector to lock is referred to as lock acquisition. Advanced Virgo is designed to use a lock acquisition technique called variable finesse [59, 60]. In the lock acquisition phase where the PRCL control is first switched on, the interferometer is adiabatically brought from mid-fringe (half the laser power leaks out through the beam splitter) to the dark fringe (no light leaks out through the beam splitter), while the interferometer should remain controlled and the arms locked. Bringing the interferometer from the mid-fringe to the dark-fringe is done by slowly changing the Michelson degree of freedom (MICH), defined as the microscopic length difference

$$\text{MICH} = (l_{\text{N}} - l_{\text{W}}) \bmod \lambda_0. \tag{3.2}$$

During this phase of the lock acquisition, the PR-autoalignment system is not yet engaged, which here means that the PR can be misaligned up to around 1 μrad. Therefore, we have quantified how the PRCL sensing signal is affected by PR-misalignments. This was of special interest before the commissioning phase reached a state where this could be experimentally tested.

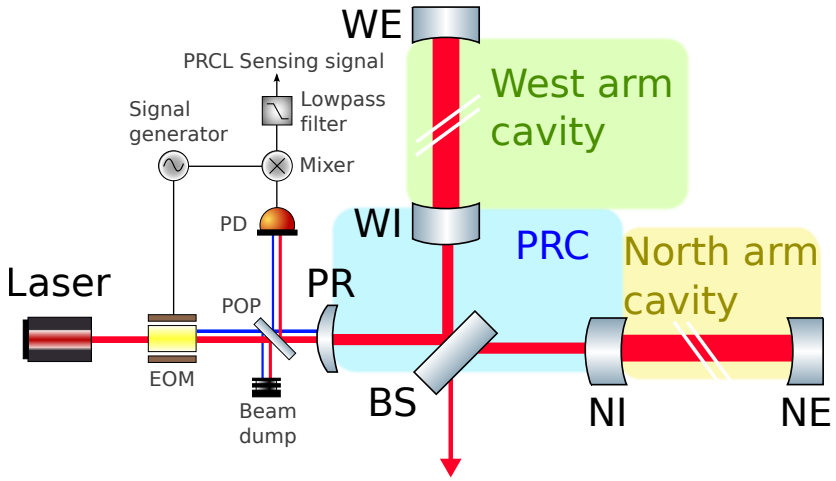

Figure 3.1: Model of Advanced Virgo with PRCL sensing. The core optics are named in black, and the PRCL sensing scheme is labelled in grey.

Since the Advanced Virgo PRC is near-unstable, this work also includes how to correctly model such a cavity in a realistic way. The main challenge here is the combination of a PR-misalignment that generates unwanted higher-order modes, and a near-unstable PRC that supports these modes. This combination may require that a large number of higher-order modes are included in the simulation for the results to be correct. However, as the computational cost increases with the number of included spatial modes, it is also of interest to not include more modes than necessary for the results to converge. Unfortunately, it is in general difficult to know how many higher-order modes that are needed beforehand. Therefore, we have investigated how to find the number of necessary higher-order modes, and which parameters this depends on. We show that this number depends strongly on the specific simulation at hand. E.g., the PRCL sensing signal requires relatively few spatial modes when there is no MICH-offset (i.e., at the dark fringe), while a large number of spatial modes are required when there is a significant MICH-offset, for example at the mid-fringe. In our case, it turns out that these variations depends on the PRC optical gain experienced by the higher-order modes of the rf-sidebands: the higher optical gain, the more spatial modes are required. We also show that when a large number of spatial modes play significant roles in the simulation, it may be necessary to include beam clipping effects due to the finite mirrors to keep the model realistic. Here, beam clipping effects include both that the part of the beam that falls outside a mirror is lost, and scattering from the edge of the mirror. The reason why these effects become significant is that the spatial mode distributions spread out more and more in the transverse directions with increasing mode number. In this work, clipping effects needed to be included when modes of about order 10 or higher were required.

In addition, we show that the modulation/demodulation frequency used to create the PRCL-sensing signal during lock acquisition could be changed from the designed 132 MHz to 119 MHz without significantly reduced PRCL sensitivity. The reason for in-

vestigating this change is that 132 MHz is too high for optimal performance of the installed electronics. This work facilitated the decision-making of going through with this change. However, it should be mentioned that after the end of this project, a different solution was implemented where neither of these two sideband frequencies were used.

This chapter is outlined as follows. In section 3.1, the Pound-Drever-Hall technique that is used to construct the PRCL sensing signal is described, and we show how the complexity of computing this signal increases significantly when a misalignment is included in the model. Section 3.3 describes how the PRCL sensing signal is affected by PR-misalignments at three different MICH-offsets: dark fringe, quarter fringe, and mid-fringe. Section 3.2 describes why realistic near-unstable cavities can be challenging to model, and we show how our PRCL sensing signal converges with increasing number of included spatial modes at the dark-fringe, the quarter-fringe and the mid-fringe for various PR-misalignments. In section 3.4 the sensing signals using the 132 MHz sidebands are shown, and we compare these to the ones using the 119 MHz sidebands.

3.1 The Pound-Drever-Hall length sensing technique

The power reflected off an optical cavity is an even function with respect to the resonance tuning of the cavity, as seen from the blue trace in figure 3.2. Thus, if the cavity is operated at resonance for the carrier field, this power signal cannot by itself convey information about in which direction to actuate on the cavity length, and would therefore not be a good length sensing signal. The phase of the reflected field on the other hand, is an odd function with respect to the carrier resonance tuning, as seen from the orange trace of figure 3.2, and would perform well as a length sensing signal.

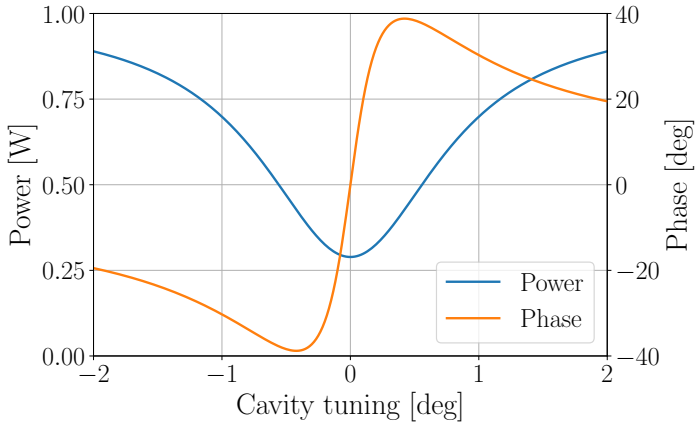

Figure 3.2: The figure shows the power and phase of a field reflected off a cavity. The field is resonating when the cavity tuning is zero.

However, since phase is not directly measurable, the phase information needs to be converted into power to utilise it in a feedback control loop. One way of doing this is by using the Pound-Drever-Hall (PDH) technique [61] that is described in this section by using a linear optical cavity as an example. The PDH-technique is implemented at numerous locations in all existing interferometric gravitational wave detectors for stabilising various lengths and laser frequencies [59, 62, 63], including the Advanced Virgo PRCL degree of freedom that is in focus in this chapter.

3.1.1 The ideal case

To describe how to sense the length of a cavity by using the PDH-technique, the setup shown in figure 3.3 is used. For simplicity, we let the cavity have a perfectly reflective end mirror and lossless input mirror. The PDH-technique requires at least two frequency components. One of these should serve as a phase reference and ideally be completely unaffected by cavity length fluctuations around the cavity resonance, while the other should be resonating in the cavity and experience a phase change similar to the one in figure 3.2. In this example, as well as for the Advanced Virgo PRC,

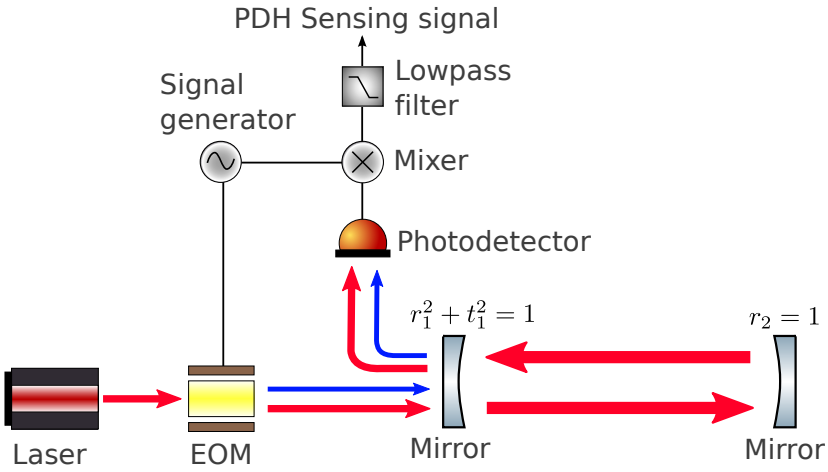

Figure 3.3: The figure shows a PDH-setup for sensing the length of a cavity. A carrier field (red) is phase modulated by an EOM, which creates modulation sidebands (blue) symmetrically spaced in frequency around the carrier. The modulation sidebands are anti-resonant in the cavity and are therefore effectively directly reflected off the input mirror. The reflected carrier on the other hand, has information about the cavity length encoded in its phase because it resonates in the cavity. This phase can be extracted by detecting the beat between the carrier and the sideband, which can be done by using a photodiode together with a mixer and a low pass filter.

the carrier resonates inside the cavity and therefore represents the latter frequency component. Thus, a second frequency component that ideally is off resonance in the PRC needs to be created. This can be achieved by phase modulating the carrier field using an electro-optic modulator (EOM). If the carrier is $E_c(t) = E_0\, e^{i\omega_0 t}$, then the phase modulated field can be described as

$$E(t) = E_c(t) e^{ih\sin(\Omega t+\theta)}, \tag{3.3}$$

where h, Ω and θ are are the modulation index, modulation frequency, and modulation phase, respectively. Assuming that $h \ll 1$, this can be Taylor-expanded to

$$\begin{aligned} E(t) &= E_0 e^{i\omega_0 t}\Big(1 + ih\sin(\Omega t+\theta) + \mathcal{O}(h^2)\Big) \\ &= E_0 e^{i\omega_0 t} + \frac{E_0 h}{2}\Big(e^{i((\omega_0+\Omega)t+\theta)} - e^{i((\omega_0-\Omega)t-\theta)}\Big) + \mathcal{O}(h^2) \\ &= E_c(t) + E_{sb}(t) + \mathcal{O}(h^2), \end{aligned} \tag{3.4}$$

where $E_{\mathrm{sb}}(t) = \frac{E_0 h}{2}\big(\mathrm{e}^{i((\omega_0+\Omega)t+\theta)} - \mathrm{e}^{i((\omega_0-\Omega)t-\theta)}\big)$. This shows that for a small modulation index h, the phase modulation of the carrier field can be described by adding two new frequency components with frequencies $\omega_0 \pm \Omega$. These are together referred to as a pair of sidebands. The phase the sidebands pick up relative to the carrier while co-propagating with the carrier can be included in the modulation phase θ, thus, there is no need to introduce another phase parameter to account for this.

Since the cavity is lossless and the end mirror has zero transmission, all of the incoming power is reflected off the cavity and we only need to consider the phase change of the three frequency components. This is given by

$$\arg\big(r_{\mathrm{FP}}(\Omega)\big) = \arg\left(\frac{r_1 - \mathrm{e}^{-2i\left(\phi+\frac{\Omega L}{c}\right)}}{1 - r_1 \mathrm{e}^{-2i\left(\phi+\frac{\Omega L}{c}\right)}}\right) \tag{3.5}$$

where $r_{\mathrm{FP}}(\Omega)$ is taken from equation B.1 in appendix B. Here, $L = k\lambda_0,\ k \in \mathbb{N}$, λ_0 is the carrier wavelength, and 2ϕ is the roundtrip phase change of the carrier. Assuming that the cavity remains nearly resonant for the carrier (i.e., ϕ is close to zero) and that the modulation frequency has been chosen such that $\frac{\Omega L}{c} = \frac{\pi}{2}$, then the reflected field becomes

$$E_{\mathrm{refl}}(t) = -E_{\mathrm{c}}(t)\mathrm{e}^{i\phi_c} + E_{\mathrm{sb}}(t) + \mathcal{O}(h^2). \tag{3.6}$$

Here, $\phi_{\mathrm{c}} = \arg\big(-r_{\mathrm{FP}}(0)\big)$. The photo detector output is proportional to the power in the reflected field, which is given by

$$\begin{aligned} S_0(t) &\propto |E_{\mathrm{refl}}|^2 \\ &= |E_0|^2 \left(1 + 2h\sin(\Omega t + \theta)\sin\phi\right) + \mathcal{O}(h^2). \end{aligned} \tag{3.7}$$

To construct the sensing signal from this photodiode signal, the field is demodulated at the frequency Ω, which is performed using an electronic mixer and a low pass filter.

The mixer can mathematically be described as a multiplication with $\sin(\Omega t+\varphi)$, where φ is called the demodulation phase, which gives us

$$\begin{aligned} S_1(t) &= S_0(t)\sin(\Omega t+\varphi) \\ &\propto |E_0|^2 \Big(\sin(\Omega t+\varphi) + h\sin\phi\big(\cos(\theta-\varphi) - \cos(2\Omega t+\theta+\varphi)\big)\Big) + \mathcal{O}(h^2) \end{aligned} \tag{3.8}$$

The low pass filter subsequently filters out all the oscillating terms, thus, the sensing signal is proportional to

$$S_{1,\mathrm{DC}} \propto h\,|E_0|^2 \cos(\theta-\varphi)\sin\phi + \mathcal{O}(h^3). \tag{3.9}$$

This sensing signal is linear in the neighbourhood of the resonance peak at $\phi = 0$ and its slope, or optical gain, is given by

$$\left.\frac{\mathrm{d}S_{1,\mathrm{DC}}}{\mathrm{d}\phi}\right|_{\phi=0} \propto h\,|E_0|^2\cos(\theta-\varphi) + \mathcal{O}(h^3). \tag{3.10}$$

By choosing the demodulation phase φ such that $\cos(\theta-\varphi) = \pm 1$, the signal is optimally sensitive to fluctuations around $\phi = 0$. As seen from this analysis, the length sensing signal in the ideal case without any optical defects is straight forward to compute by hand and has a simple analytic expression as seen in equation 3.9. However, already when introducing a relatively simple optical defects in the form of a misalignment, the calculations becomes time consuming and tedious, even for a simple and otherwise ideal optical cavity, as shown below in section 3.1.2.

3.1.2 The misaligned case

So far we have considered the ideal case where plane waves can be used, which is valid as long as there are no optical defects or spatial mismatches that introduces higher-order spatial modes. However, this condition is not in general satisfied, and certainly

not in the cases considered in this chapter. In the non-ideal general case, the field reflected off the cavity is not perfectly Gaussian and therefore needs a sum of spatial modes to be described:

$$E_{\mathrm{refl}}(t) = \sum_{j=0}^{2}\sum_{m=0}^{\infty}\sum_{n=0}^{\infty} b_{jmn}u_{mn}\exp(i\omega_j t) + \mathcal{O}(h^2) \tag{3.11}$$

Here, $\omega_1 = \omega_0 - \Omega$, $\omega_2 = \omega_0 + \Omega$, and b_{jmn} are complex amplitudes containing all phase information of the reflected field components. The power on the photodiode is given by

$$P_{\mathrm{refl}} \propto \iint_{-\infty}^{\infty} |E_{\mathrm{refl}}|^2 \,\mathrm{d}x\mathrm{d}y = \sum_{j=0}^{2}\sum_{j'=0}^{2}\sum_{m=0}^{\infty}\sum_{n=0}^{\infty} b_{jmn}b^*_{j'mn}\exp\big(i(\omega_j - \omega_{j'})t\big), \tag{3.12}$$

which after demodulation and low pass filtering results in

$$S_{1,\mathrm{DC}} = \mathrm{Re}\Big\{\mathrm{e}^{-i\varphi}\sum_{m=0}^{\infty}\sum_{n=0}^{\infty}\big(b_{0mn}b^*_{1mn} + b^*_{0mn}b_{2mn}\big)\Big\} + \mathcal{O}(h^3). \tag{3.13}$$

However, the main challenge is in general not to compute the sensing signal given the reflected complex amplitudes b_{jmn}, but to compute these complex amplitudes in the first place. For the case of a misaligned input mirror, the complex amplitudes

$$\mathbf{b}_j = \begin{bmatrix} b_{j00} & \cdots & b_{jmn} & \cdots & b_{jMN} \end{bmatrix}^{\mathrm{T}} \tag{3.14}$$

that describe the reflected field can be computed as

$$\mathbf{b}_j = \big(r\mathbf{K}_3 + t^2\mathrm{e}^{-i\frac{2\Omega L}{c}}\mathbf{K}_1^{-1}(\mathbf{1} + r\mathrm{e}^{-i\frac{2\Omega L}{c}}\mathbf{\Psi}\mathbf{K}_2)^{-1}\mathbf{\Psi}\mathbf{K}_1\big)\mathbf{a}_j \tag{3.15}$$

Here, the vectors

$$\mathbf{a}_j = \begin{bmatrix} a_{j00} & 0 & \cdots & 0 \end{bmatrix}^{\mathrm{T}}, \tag{3.16}$$

represent perfectly Gaussian input fields, and the matrices $\mathbf{K}_1$, $\mathbf{K}_2$ and $\mathbf{K}_3$ contain the coupling coefficients between the spatial modes when interacting with the misaligned input mirror. More specifically, these matrices represents couplings on transmission, reflection off the inner misaligned surface, and reflection off the outer misaligned surface, respectively. Each one of these coupling matrices are of the form

$$\mathbf{K} = \begin{bmatrix} K_{00,00} & \cdots & K_{00,mn} & \cdots & K_{00,MN} \\ \vdots & \ddots & \vdots & \ddots & \vdots \\ K_{mn,00} & \cdots & K_{mn,mn} & \cdots & K_{mn,MN} \\ \vdots & \ddots & \vdots & \ddots & \vdots \\ K_{MN,00} & \cdots & K_{MN,mn} & \cdots & K_{MN,MN} \end{bmatrix}, \tag{3.17}$$

with

$$K_{mn,m'n'} = \iint_{-\infty}^{\infty} u_{m'n'}(x,y,z) A(x,y,z) u^*_{mn}(x,y,z)\,\mathrm{d}x\mathrm{d}y. \tag{3.18}$$

Here, $A(x,y,z)$ characterises the optical defect. In the case of $\mathbf{K_2}$ for example, which represents a single reflection off the misaligned HR-surface of the input mirror,

$$A(x,y,z) = \mathrm{e}^{ik\left(2z\sin^2\frac{\beta}{2} + x\sin(\beta)\right)}. \tag{3.19}$$

For the other two coupling matrices, the function $A(x,y,z)$ is more complicated as the beam interacts with the misaligned AR-surface in addition to the HR-surface, which can be accounted for by combining multiple coupling matrices. The roundtrip phase

picked up due to Gouy-phase is included via the matrix

$$\mathbf{\Psi} = \begin{bmatrix} \Psi_{00} & 0 & \cdots & \cdots & 0 \\ 0 & \ddots & \ddots & & \vdots \\ \vdots & \ddots & \Psi_{mn} & \ddots & \vdots \\ \vdots & & \ddots & \ddots & 0 \\ 0 & \cdots & \cdots & 0 & \Psi_{MN} \end{bmatrix}, \tag{3.20}$$

where $\Psi_{mn} = \mathrm{e}^{i(m+n)\psi_{\mathrm{rt}}}$ and ψ_{rt} is the roundtrip Gouy-phase.

As seen from this analysis, computing the length sensing signal becomes time consuming and tedious already when introducing a relatively simple optical defect in the form of a misalignment. This motivates the development and use of the simulation software FINESSE and its Python wrapper PyKat, which are used for remainder of this chapter.

3.2 Modelling of a near-unstable cavity using Finesse

This section describes the challenges of modelling a near-unstable cavity with optical defects in general, and how to correctly compute the length sensing signal for the misaligned near-unstable PRC in Advanced Virgo in particular. The main challenge for a near-unstable cavity lies in that the resonance condition is near-degenerate for many spatial modes. Thus, if there are undesired higher-order modes present in the laser field, they will not be suppressed by the cavity. As a consequence, a large number of higher-order modes may need to be included to make sure that the simulation results converge. However, since the computational cost increases with the number of included spatial modes, it is also of interest to not include more higher-order modes than nec-

essary. We show how the number of spatial modes that is required for the PRCL sensing signal to converge grows with increasing PR-misalignment when the MICH degree of freedom is tuned to the dark fringe, the mid-fringe, and the quarter-fringe. We also explain why we expect the number of necessary included modes to increase with decreasing roundtrip Gouy-phase and cavity finesse. We also show that the finite mirrors sizes can play a significant role when the higher-order mode content grows.

3.2.1 Stability, Gouy-phase and mode separation

For an optical cavity to form a stable resonator, it must periodically refocus the intracavity beam. The propagation of the spatial properties of a laser beam that satisfies the paraxial approximation can be analysed using the linear ray transfer matrices [64, 65, 25, 26], which are also referred to as ABCD-matrices. If a roundtrip in a cavity is described by the ABCD-matrix

$$\mathbf{M} = \begin{bmatrix} A & B \\ C & D \end{bmatrix}, \tag{3.21}$$

then it can be shown [64] that this cavity periodically refocuses the beam—hence is stable—if the stability parameter

$$m = \frac{\mathrm{tr}(\mathbf{M})}{2} = \frac{A + D}{2} \tag{3.22}$$

satisfies the inequality

$$-1 \leq m \leq 1. \tag{3.23}$$

Thus, the cavity is called near-unstable if m is close to ± 1. Another common stability parameter is $g = (m+1)/2$, which is especially useful for two-mirror cavities as it then can be written as

$$g = g_1 g_2 = \left(1 - \frac{L}{R_1}\right)\left(1 - \frac{L}{R_2}\right), \tag{3.24}$$

where L is the length of the cavity and R_1 and R_2 are the radii of curvature of the two mirrors.

The accumulated roundtrip Gouy-phase can be expressed in terms of the roundtrip ABCD-matrix [66] with the formula

$$\Psi_{\mathrm{RT}}(\mathbf{M}) = 2\arccos\left(\mathrm{sgn}(B)\sqrt{\frac{A+D+2}{4}}\right) = 2\arccos\left(\mathrm{sgn}(B)\sqrt{g}\right). \tag{3.25}$$

This yields a roundtrip Gouy-phase between 0 and 360 degrees as seen in figure 3.4. The extra roundtrip phase picked up by a HG_{mn}-mode due to the Gouy-phase, is given by

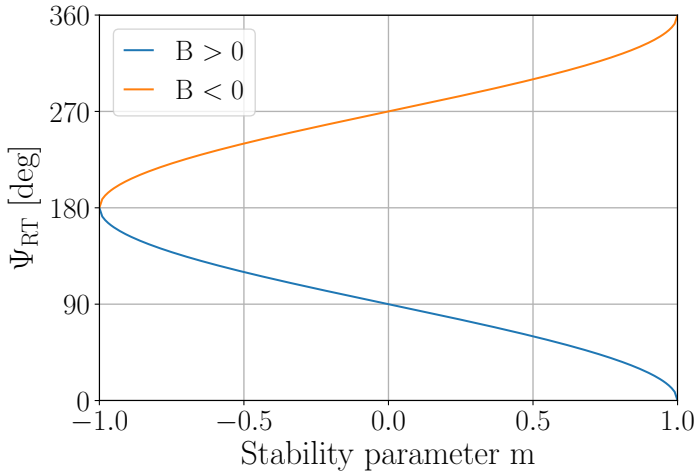

Figure 3.4: Depending on the stability of the cavity, and the sign of element B in the ABCD-matrix, the Gouy phase accumulated during a roundtrip in a cavity can be between 0 and 360 degrees.

$$\Psi_{mn} = (m + n + 1)\psi_{\mathrm{rt}}. \tag{3.26}$$

It is important to know the spacing of different spatial modes in terms of reference frequency, as one ideally does not want any unwanted spatial modes to be on resonance together with the fundamental mode. The mode separation frequency between cavity eigenmodes of consecutive order can be defined as

$$\delta f = \begin{cases} \frac{\psi_{\mathrm{rt}}}{2\pi}\,\Delta f, & \psi_{\mathrm{rt}} \leq \pi \\ \left(1 - \frac{\psi_{\mathrm{rt}}}{2\pi}\right)\Delta f, & \psi_{\mathrm{rt}} > \pi, \end{cases} \tag{3.27}$$

where Δf is the free spectral range of the cavity. However, since this does not involve the width of the resonance peaks, this number does not tell us how well the spatial mode peaks are resolved. A measure of this resolution can be formed by dividing the mode separation frequency by the linewidth [67], thus, one obtains

$$\mathcal{S} = \frac{\delta f}{\gamma} = \begin{cases} \frac{\psi_{\mathrm{rt}}}{2\pi}\,F, & \psi_{rt} \leq \pi \\ \left(1 - \frac{\psi_{\mathrm{rt}}}{2\pi}\right)F, & \psi_{rt} > \pi. \end{cases} \tag{3.28}$$

Here, $F = \Delta f/\gamma$ is the cavity finesse and γ is the FWHM of the intra cavity resonance peak. From this expression one can see that the resolution of the spatial modes depends on the cavity finesse in addition to the stability through the Gouy phase. Thus, we generally expect a simulation of a near-unstable cavity with low finesse to require the inclusion of a larger amount of higher order modes than a stable high-finesse cavity, assuming the optical defect is the same in both cases. Figure 3.5 highlights this by showing cavity scans of four cavities with different combinations of finesse and stability, all having the end mirror misaligned by 10 μrad. One can see that the mode separation factor decreases with decreased finesse and near-instability, and in addition, one can see that the ratio between the misalignment angle and the diffraction angle increases the closer to instability the cavity is. Thus, a near-unstable cavity also generates a

larger amount of higher-order modes than a stable cavity for the same misalignment angle.

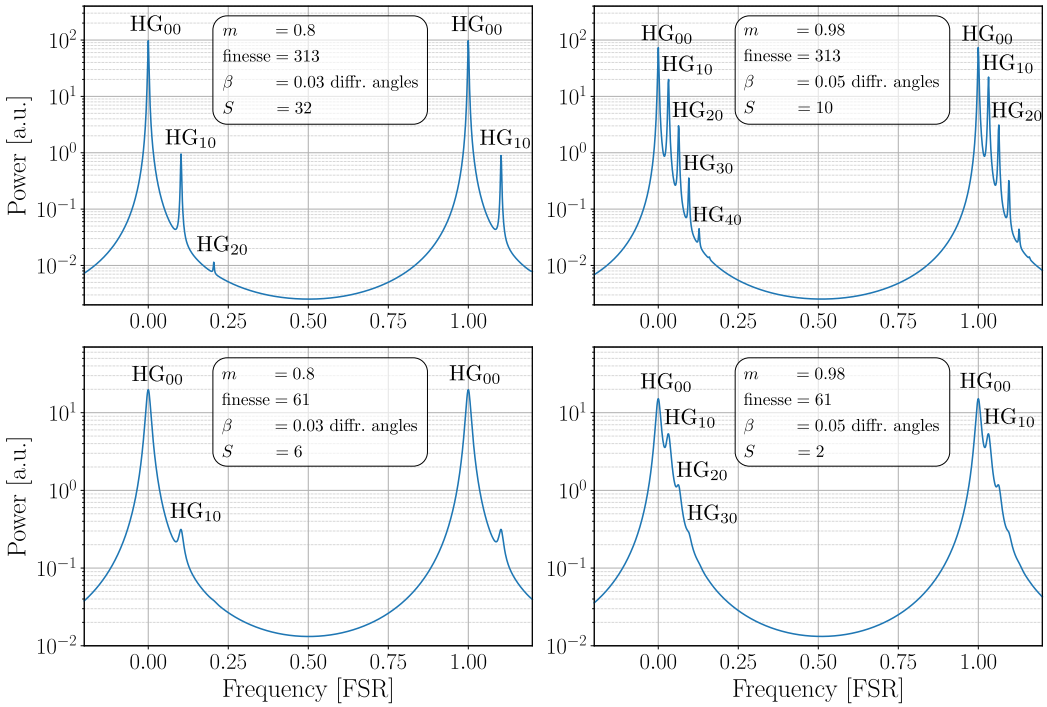

Figure 3.5: The figure shows simulated scans of four misaligned cavities with different combinations of cavity finesse and stability. The input power and the misalignment angle ($\beta_{\text{abs}} = 10$ μrad) are the same in all four cases.

The PRC mode separation factors for the frequencies and MICH-offsets of interest in the Advanced Virgo model are listed in table 3.1, and these were computed by using equation 3.28. The roundtrip Gouy phase is $\Psi_{\text{rt}} \approx 0.21$ deg, and the cavity finesse for the different frequencies and MICH-offsets are shown in table 3.3. The cavity finesse depends both on frequency due to the Schnupp asymmetry, and on the MICH tuning as these two together determine the fraction of the field that leaks out through the dark fringe. The listed mode separation factors are small, and indicate that many spatial modes overlap almost completely. However, bear in mind that for the carrier, there is an extra 180 degree phase shift between the fundamental mode and the higher-order modes as the fundamental mode is resonating in the arm cavities while the higher-order modes are not. Thus, the carrier higher-order modes are suppressed in the PRC.

Table 3.1: Mode separation factors in the Advanced Virgo power recycling cavity for the studied sidebands and fringes.

Symbol	Parameter	Dark fringe	Quarter fringe	Half fringe
Carrier				
$\mathcal{S}$	HOM separation factor	$5.4 \cdot 10^{-2}$	$1.0 \cdot 10^{-2}$	$4.7 \cdot 10^{-3}$
119 MHz sidebands				
$\mathcal{S}_{-119}$	HOM separation factor	$9.0 \cdot 10^{-3}$	$6.9 \cdot 10^{-2}$	$3.6 \cdot 10^{-2}$
$\mathcal{S}_{+119}$	HOM separation factor	$9.0 \cdot 10^{-3}$	$2.1 \cdot 10^{-3}$	$7.9 \cdot 10^{-4}$

3.2.2 Beam clipping

Another important aspect to keep in mind when modelling systems with relatively large optical defects is that the transverse distribution of the field can change significantly. The beam radius in the x-direction of an individual HG-mode can be defined [68, 69] as

$$w_{x,m}(z) = w_x(z)\sqrt{m+1}, \tag{3.29}$$

where $w_x(z)$ is the beam radius of the fundamental mode. The beam radius in the y-direction is defined in the same way by changing m into n. Thus, the HG-modes spread out more and more with increasing m and n, which is shown in figure 3.6. More specifically, the figure shows the power distribution of the HG-modes in the PRC, the size of the PR, WI and NI mirrors, and the rectangular beam size defined by equation 3.29. These mirrors have radii of 17.5 cm and the radius of the fundamental mode is about 4.9 cm at all these mirrors [59]. Thus, if the mode order is high enough, the mode is subjected to non-negligible clipping effects on the mirrors, which need to

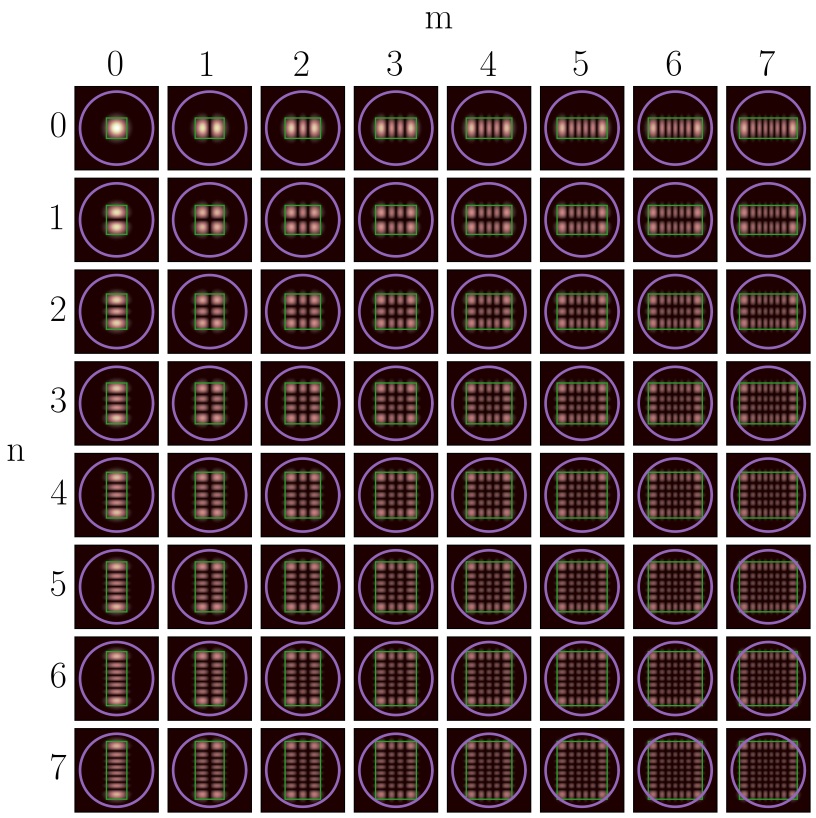

Figure 3.6: The figure shows the spatial power distribution for some HG-modes. The purple circle shows the size the of the PR and input test masses, and the green rectangle indicates the spot size defined by equation 3.29.

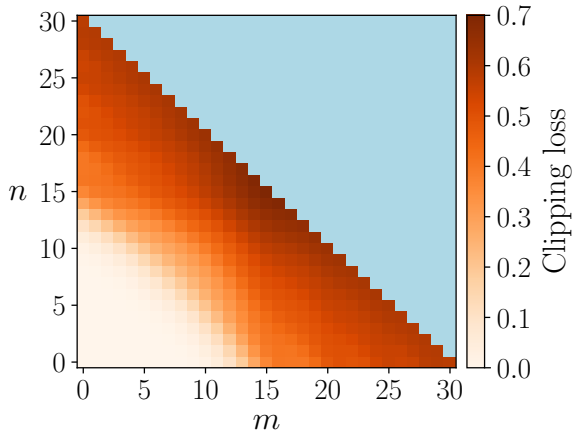

Figure 3.7: The figure shows the fraction of power lost due to clipping at a mirror for HG_{mn}-modes. The mirror radius was set to 17.5 cm, and the fundamental mode beam radius wast set to $w_{x,0} = w_{y,0} = 4.9$ cm.

be accounted for to keep the model realistic. Figure 3.7 shows the power lost due to beam clipping at a mirror of the same size as the PR, WI and NI for various HG_{mn}

modes in the Advanced Virgo PRC. However, power loss is not the only effect the finite mirrors have on the beam: the edge also scatters the light, effectively creating couplings between different spatial modes.

3.2.3 Convergence of PRCL sensing signal

To investigate how to correctly model the PRCL sensing signal for Advanced Virgo, a FINESSE model matching figure 3.1 was created. The PRCL sensing signal was computed with an increasing number of included spatial modes until the sensing signal satisfied a convergence criteria. The cost function used here is the Hausdorff [70] distance normalised by a characteristic length. I.e., for each maxtem value M, the sensing signal $y_M(x_i)$ was computed for N different PRCL-tunings x_i. Then we compute the normalised Hausdorff distance as

$$f_{M-1} = \max\left(\frac{|y_M(x_i) - y_{M-1}(x_i)|}{\frac{1}{N}\sum_{k=1}^{N}|y_{M-1}(x_k)|}\right), \tag{3.30}$$

and say that the simulation converged for maxtem $M-1$, if $f_{M-1} < 5 \cdot 10^{-3}$. This procedure was performed with both finite and infinite mirrors, and at three different MICH tunings: mid fringe, quarter fringe, and dark fringe. The results can be seen in figure 3.8. We can see that at the dark fringe, the sensing signal converges for $M < 14$ for misalignments up to at least 1.5 μrad, while at the quarter and mid fringes, the simulations fail to converge for $M < 24$, already for PR-misalignments of 0.25 μrad and 0.35 μrad, respectively. The reason for these huge differences is that:

(i) At the the dark fringe, the fundamental mode of the carrier has a high PRC-gain, while the carrier higher-order modes and the rf-sidebands experience low PRC-gains. Thus, the higher-order modes created by the the misalignment are suppressed by the PRC, which keeps the required number of higher-order modes

down.

(ii) At the quarter and the mid-fringes, the fundamental mode of the carrier has a low PRC gain, while the fundamental mode of one of the sidebands has a high PRC gain. Since many higher-order modes have essentially as high PRC-gains as the fundamental mode, a lot of higher-order modes play significant roles in the simulation.

In the figure, one can also see that the traces for finite and infinite mirrors are essentially identical for small maxtems, but diverge more and more as the maxtem is increased.

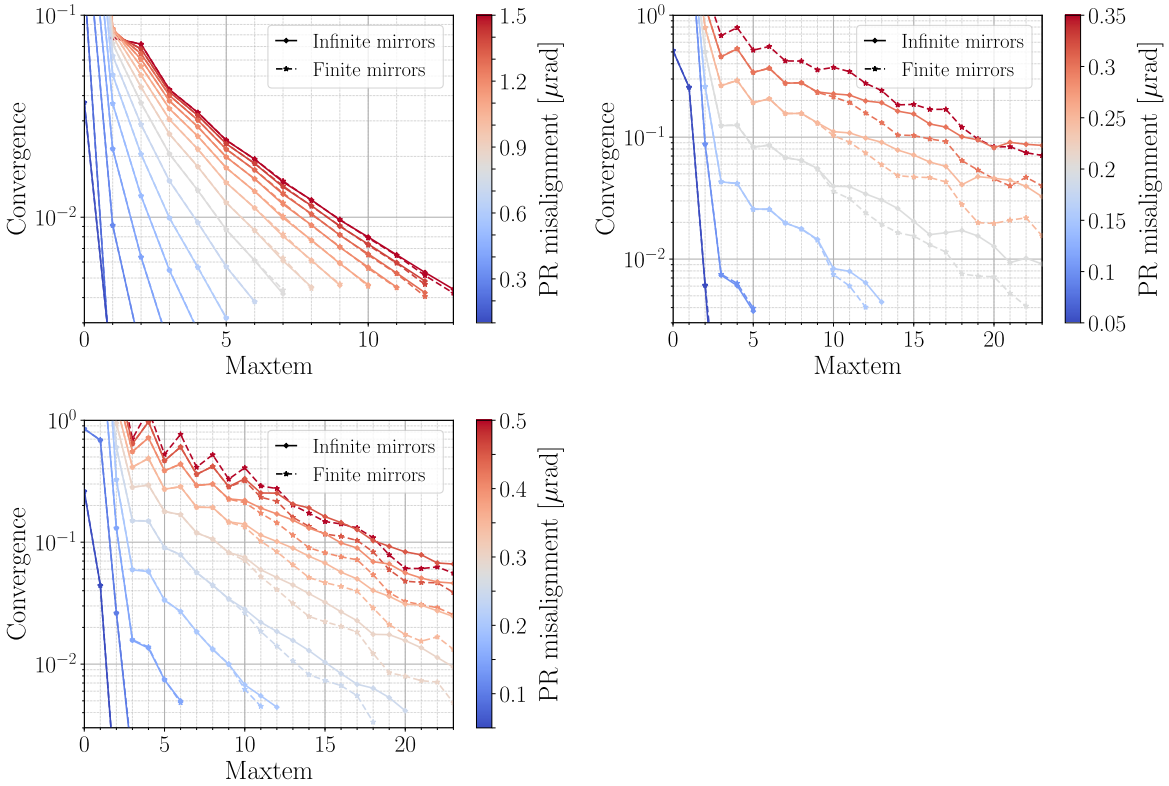

Figure 3.8: The figures shows how the PRCL sensing signal converges with increasing maxtem for various PR-misalignments when operating at dark-fringe (top left), the quarter-fringe (top right), and the mid-fringe (bottom left). The data points are are the normalised Hausdorff-distances, given by equation 3.30. We say that the simulation has converged if the value is less than $5 \cdot 10^{-3}$.

3.3 PR misalignment effects on lock acquisition PRCL sensing

This section focuses on the PRCL sensing during the lock acquisition phase called MICH offset reduction [59], during which the interferometer is adiabatically brought from the mid fringe to the dark fringe. At this stage, the PR alignment is only roughly controlled as the automatic alignment system is not switched on until MICH has been brought to its operating point. In this case, this means that PR can be misaligned up to around 1 μrad. To isolate the effect that the PR-misalignment has on the PRCL sensing signal, we assume that all other degrees of freedom are at their operating points, which should be close to true in the reality as well.

The PRCL sensing signal is constructed using the Pound-Drever-Hall technique [61] described in section 3.1. For Advanced Virgo, the modulation frequency chosen as phase reference for the PRCL sensing signal during lock acquisition was 119.144763 MHz ($\approx$ 119 MHz). This frequency actually satisfies the resonance condition of the PRC when operating at the dark fringe, nonetheless, the $\pm$119 MHz sidebands experience a very low cavity finesse. The reason is that a large fraction of these frequency components leaks out through the dark port due to the Schnupp-asymmetry, which is the macroscopic length difference between the two legs of the Michelson interferometer:

$$\Delta l_{\mathrm{M}} = l_{\mathrm{N}} - l_{\mathrm{W}} \tag{3.31}$$

For Advanced Virgo, the Schnupp-asymmetry is $\Delta l_{\mathrm{M}} = 0.23$ m [59]. As a consequence of the low PRC gain experienced by the sidebands, the dominating part of the modulation sidebands is directly reflected off the PR-mirror without entering the cavity, which means that these sidebands only are weakly affected by cavity length changes and serves as a good phase reference, even though they are technically on resonance.

The fact that the sidebands satisfy the resonance condition will prove to be of importance when moving away from the dark fringe by altering the MICH degree of freedom.

The FINESSE model used for simulating this, is shown in figure 3.1, and was built to match the real Advanced Virgo as well as possible. The PRC-parameters of the model are shown in table 3.2. The three cavities were made to be well mode matched, and all the degrees of freedoms where tuned to their operating points before introducing any PR-misalignment or MICH-offset. The mirrors PR, WI and NI were all given the finite radius of 17.5 cm to account for realistic clipping losses that become significant when the PR-misalignment grows relatively large, and it was made sure that enough spatial modes were included in the simulations for the computed sensing signals to converge. However, some of the figures below include traces that only nearly converged. These have been either dashed or given a different colour to clearly single them out. The convergence and the beam clippings are described in greater detail in section 3.2.

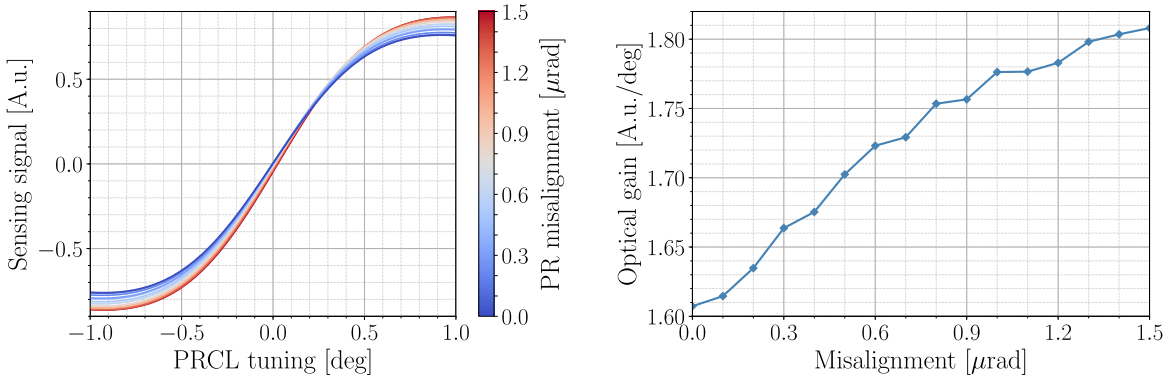

Figure 3.9: The left part shows simulated PRCL sensing signals for Advanced Virgo at dark-fringe, with PR-misalignments up to 1.5 μrad. The right part shows the optical gains of these sensing signals, computed at the zero crossings.

The dark fringe PRCL sensing signal for PR-misalignments up to 1.5 μrad is seen in the left part of figure 3.9. The y-axis is expressed in an arbitrary unit to emphasise that our numbers at best can be proportional to measured numbers as we did not include

the full path to the readout, nor the efficiency of the photo diode. The traces show that the sensing signal is only weakly affected by the misalignment, and that it—perhaps surprisingly—grows stronger with increasing misalignment. The latter effect is shown more clearly in the right part of figure 3.9, where the trace indicate the optical gain (the slope at the zero-crossing) of the sensing signal as a function of PR-misalignment. To understand this increasing optical gain, we break it down into how the different frequency components and their spatial modes are affected by the misaligned PRC:

(i) **The carrier.** The fundamental mode is resonant in the arms and in the PRC. The higher-order modes are off resonance in the arms, thus, they pick up a phase shift of about 180 degrees relative to the fundamental mode when reflected off the arm cavities. Because of this, and because the roundtrip Gouy-phase in the PRC is very small (close to zero), the higher-order modes are nearly anti-resonant in the PRC. Thus, the higher-order modes are strongly suppressed in the PRC, which makes the fundamental mode dominant at the carrier frequency even for relatively large misalignments. With other words, the carrier field is not affected much by PR-misalignments.

t

(ii) **The sidebands**. Both the fundamental mode and the higher-order modes are off resonance in the arm cavities, therefore they pick up roughly the same phase when reflected off the input mirrors of the arm cavities. Since, in addition, the Gouy-phase is very small, the fundamental mode and the higher-order modes essentially resonate together in the PRC, i.e., the higher-order modes are not suppressed relative to the fundamental mode. Therefore, as the PR-misalignment grows, more and more power is diverted from the fundamental mode to generate the higher-order modes, which decreases the effective PRC gain of the fundamental mode. This, in turn, makes the fundamental mode a better phase reference for the sensing signal, which consequently grows stronger with increasing PR-

misalignment.

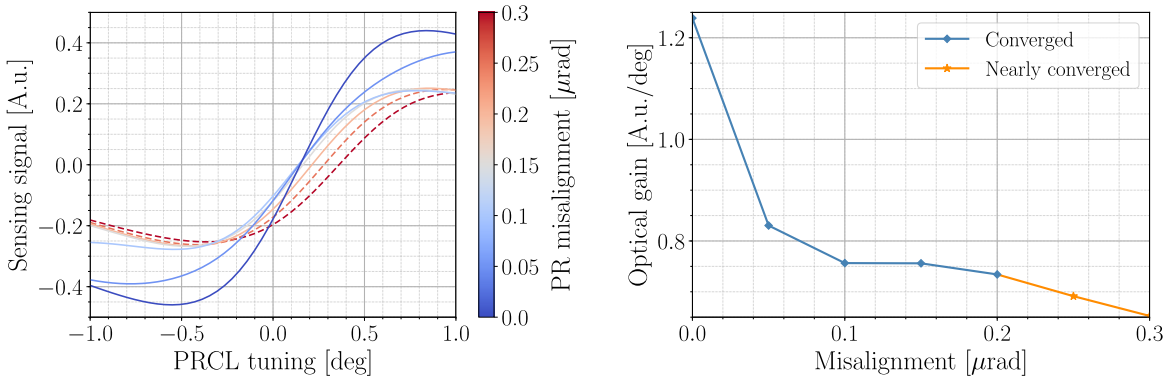

Figure 3.10: The left part of the figure shows simulated PRCL sensing signals for advanced Virgo at quarter-fringe with six different PR-misalignment values. A dashed trace indicate that the sensing signal did not satisfy the convergence criteria with spatial modes up to order 23 included. However, it was close enough to convergence to give a good indication of the actual trace. The right part shows the optical gain of the sensing signals, computed at the zero crossings.

The fraction of the field amplitude leaking out through the dark fringe is approximately given by $\sin\left(\Delta\phi_M + \frac{\Omega\Delta l_\mathrm{M}}{c}\right)$. Thus, as we move away from the dark fringe by increasing the magnitude of the MICH tuning $\Delta\phi_\mathrm{M}$, the carrier experiences an increasingly lossy PRC. As a consequence, the phase of the carrier that is reflected off the PRC is less and less affected by PRCL changes as the MICH-offset increases. For the pair of sidebands however, the non-zero MICH tuning together with the Schnupp-asymmetry of $\Delta l_\mathrm{M} = 0.23$ m, introduces a gain asymmetry between the two sidebands. Thus, the PRC gain of the upper sideband decreases, while it increases for the lower sideband until it reaches a maximum at $\Delta\phi_\mathrm{M} = \frac{\Omega\Delta l_\mathrm{M}}{c} \approx 0.18\pi$. The PRC gain, finesse and linewidth for each of the three frequency components when the interferometer is operated at dark, quarter and mid-fringe are listed in table 3.3.

At the quarter and mid-fringes, the carrier and the lower sidebands have switched roles compared to at the dark fringe: the lower sideband is now the frequency component that is most sensitive to PRCL changes, while the carrier phase is only weakly affected by PRCL and acts as the phase reference. Thus, for the same reason that the optical

gain of the sensing signal increased with increasing misalignment at the dark fringe, the optical gain decreases with increasing PR misalignment at the quarter and mid fringe, as seen in the figures 3.10 and 3.11.

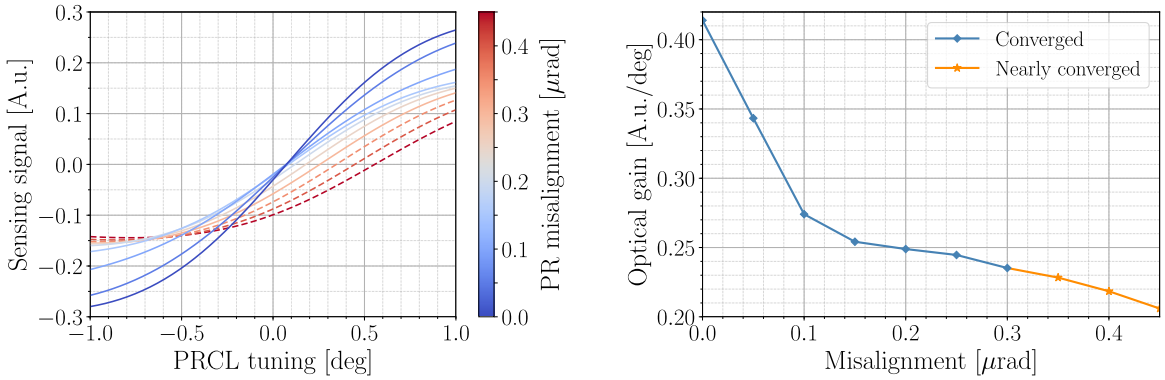

Figure 3.11: The left part of the figure shows simulated PRCL sensing signals for advanced Virgo at mid-fringe with nine different PR-misalignment values. A dashed trace indicate that the sensing signal did not satisfy the convergence criteria with spatial modes up to order 23 included. However, it was close enough to convergence to give a good indication of the actual trace. The right part shows the optical gain computed at the zero crossing of the sensing signal.

Further, it is of importance that the zero crossing of the sensing signal—that defines the operating point—is a continuous function of PR-misalignment. Any discontinuities could lead to the loss of lock. Figure 3.12 shows the zero crossings for the three investigated fringes, and does not indicate that there are any discontinuities within the investigated PR-misalignment domains.

Another interesting aspect of this study is that the simulated sensing signals failed to satisfy the convergence criteria for misalignments above 0.2 μrad and 0.3 μrad at the quarter and mid fringes, respectively, while there were no convergence issues at all at the dark fringe for misalignments up to at least 1.5 μrad. For the cases where the convergence failed, the simulations were tested with spatial modes up to order 24 included. The reason for these large convergence differences lies mainly in the PRC gain

of the sidebands. More on convergence and on how to correctly model and simulate the misaligned near-unstable PRC is found in section 3.2.

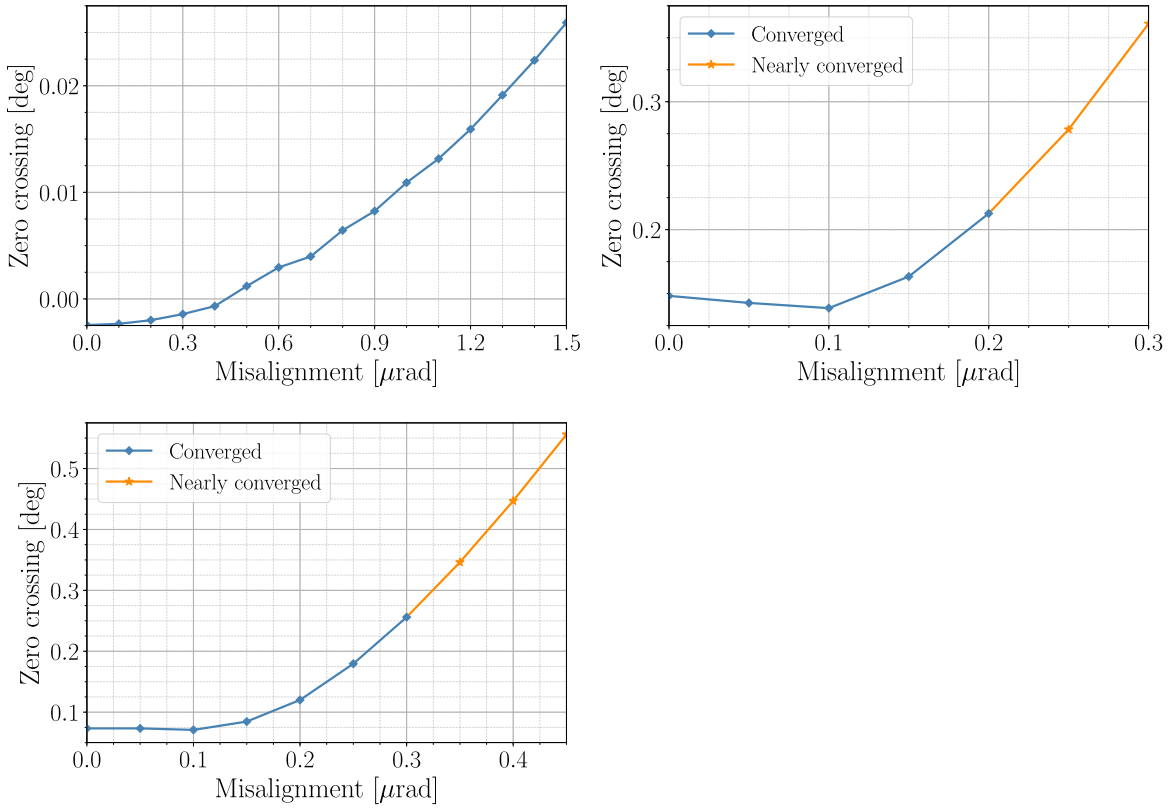

Figure 3.12: The zero-crossings of the PRCL sensing signals at the dark fringe (top left), quarter fringe (top right), and the mid-fringe (bottom left).

3.4 119 MHz vs. 132 MHz modulation frequency for PRCL sensing during lock acquisition in Advanced Virgo

Advanced Virgo was designed to use the beat signal between the carrier and a 131.686317 MHz ($\approx$ 132 MHz) modulation sideband for PRCL sensing during lock acquisition. However, this frequency is slightly too high for optimal performance of an electronic circuit in the installed electronics that is used to read out the sensing signal. Instead of changing the electronics, it was decided to use the 119 MHz modulation sideband

Table 3.2: Advanced Virgo PRC-parameters used in the FINESSE-model.

Symbol	Parameter	Value
L_{PRC}	Optical path length [m]	11.9515
ΔL	Schnupp asymmetry [m]	0.2301
m	Stability	0.999993
Ψ_{RT}	Roundtrip Gouy-phase [rad]	$3.64 \cdot 10^{-3}$
Δf	Free spectral range [MHz]	12.54

that also is used in the previous sections of this chapter. However, before the decision was taken, the difference in performance between the two frequencies was investigated to facilitate the decision making, and this is the work presented in this section. We show that the 132 MHz sidebands optically perform only slightly better than the 119 MHz sidebands, and that the two different pairs of sidebands are similarly affected by PR-misalignments.

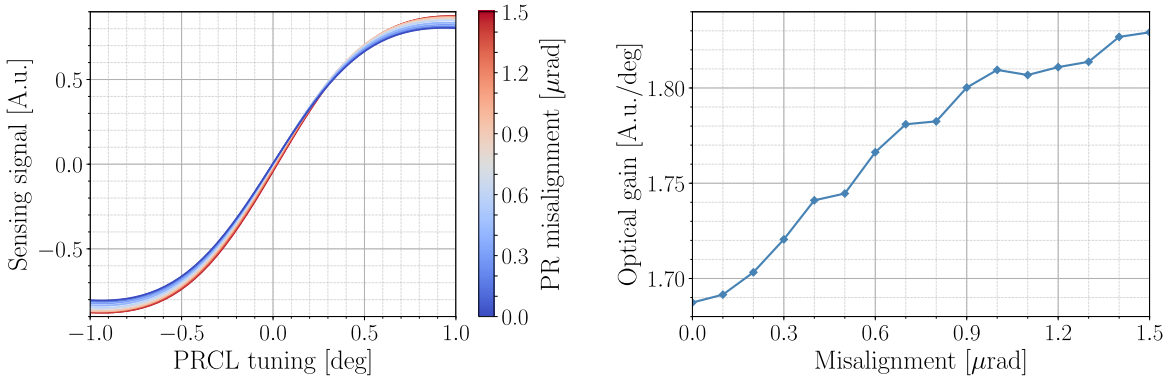

Figure 3.13: The left part shows simulated 132 MHz PRCL sensing signals for advanced Virgo at dark-fringe with six different PR-misalignment values, modelled with finite mirrors. The right part shows the optical gains of these sensing signals, computed at the zero crossings.

The fraction of the PRC field that leaks out through the dark port is approximately

Table 3.3: The table lists the gain, finesse and linewidth of the carrier and the pair of 119 MHz sidebands in the PRC when operated at the dark, quarter and mid-fringe. All values have been computed using the software FINESSE.

Symbol	Parameter	Dark fringe	Quarter fringe	Half fringe
Carrier				
γ	Carrier PRC FWHM [MHz]	0.1350	0.7112	1.538
F	PRC finesse $\left(\frac{\text{FSR}}{\text{FWHM}}\right)$	92.9	17.6	8.16
G	PRC gain $\left(\frac{P_{\text{cav}}}{P_{\text{in}}}\right)$	43.6	1.82	0.483
119 MHz sidebands				
γ_{-119}	-119 MHz PRC FWHM [MHz]	0.8030	0.1056	0.1990
γ_{+119}	$+119$ MHz PRC FWHM [MHz]	0.8030	3.499	9.132
F_{-119}	PRC finesse $\left(\frac{\Delta f}{\gamma_{-119}}\right)$	15.6	119	63.0
F_{+119}	PRC finesse $\left(\frac{\Delta f}{\gamma_{+119}}\right)$	15.6	3.58	1.37
G_{-119}	PRC gain $\left(\frac{P^{\text{cav}}_{-119}}{P^{\text{in}}_{-119}}\right)$	1.47	71.0	20.5
G_{+119}	PRC gain $\left(\frac{P^{\text{cav}}_{+119}}{P^{\text{in}}_{+119}}\right)$	1.47	0.153	$7.47 \cdot 10^{-2}$

given by

$$l_{\text{DP}}(\Omega) = \sin\left(\frac{\Omega \Delta l_M}{c} + \Delta\phi_M\right), \tag{3.32}$$

where Ω is the sideband frequency, $\Delta l_M = 0.23$ m is the Schnupp asymmetry, and $\Delta\phi_M$ is the MICH-offset. Thus, the two different pairs of sidebands experience different PRC gains due to the Schnupp-assymetry, i.e., the 23 cm optical path difference between the beam splitter and the input mirror in the north and west arms. This length asymmetry makes different frequency components interfere differently when recombined at the beam splitter, thus allowing for the frequency dependent leakage through the dark port seen in equation 3.32. At the dark fringe ($\Delta\phi_M = 0$), the PRC gain is symmetric around the carrier, thus, the upper and lower sidebands of the same pair experience

Table 3.4: The table shows the linewidth, cavity finesse, gain and higher-order mode separation factors for the 132 MHz sidebands in the PRC.

Symbol	Parameter	Dark fringe	Quarter fringe	Half fringe
γ_{-132}	-132 MHz PRC FWHM [MHz]	0.9720	0.1240	0.1518
γ_{+132}	$+132$ MHz PRC FWHM [MHz]	0.9720	4.133	$> \Delta f$
F_{-132}	PRC finesse $\left(\frac{\Delta f}{\gamma_{-132}}\right)$	12.9	101	82.6
F_{+132}	PRC finesse $\left(\frac{\Delta f}{\gamma_{+132}}\right)$	12.9	3.04	< 1
G_{-132}	PRC gain $\left(\frac{P^{\mathrm{cav}}_{-132}}{P^{\mathrm{in}}_{-132}}\right)$	1.04	51.7	34.7
G_{+132}	PRC gain $\left(\frac{P^{\mathrm{cav}}_{+132}}{P^{\mathrm{in}}_{+132}}\right)$	1.04	0.128	$6.51 \cdot 10^{-2}$
$\mathcal{S}_{-132}$	HOM separation factor	$7.5 \cdot 10^{-3}$	$5.9 \cdot 10^{-2}$	$4.8 \cdot 10^{-2}$
$\mathcal{S}_{+132}$	HOM separation factor	$7.5 \cdot 10^{-3}$	$1.8 \cdot 10^{-3}$	$< 5.8 \cdot 10^{-4}$

the same PRC gain. The dark fringe optical gain—along with the linewidth, cavity finesse and HOM separation factor—of the ±132 MHz sidebands can be seen in the dark fringe column of table 3.4. If we compare these numbers to the optical gains of the ±119 MHz sidebands shown in table 3.3 in section 3.3, we see that the ±132 MHz sidebands have the lower PRC gain. As a consequence, the ±132 MHz sidebands produce a slightly better sensing signal than the ±119 MHz sidebands, as seen by comparing figure 3.13 to figure 3.9 in section 3.3. We can also see that the two modulation frequencies produce sensing signals that are similarly affected by misalignments.

As we move away from the dark fringe by increasing the MICH offset, the PRC gain of the carrier and the upper sideband decreases, while it increases for the lower sideband. At the quarter and mid fringes, the lower sideband is the frequency component with the highest PRC gain—for both modulation frequencies—while the carrier gain is low. This can be seen in the quarter and mid fringe columns of tables 3.4 and 3.3, where we also can see that the -132 MHz sideband has a lower gain than the -119 MHz

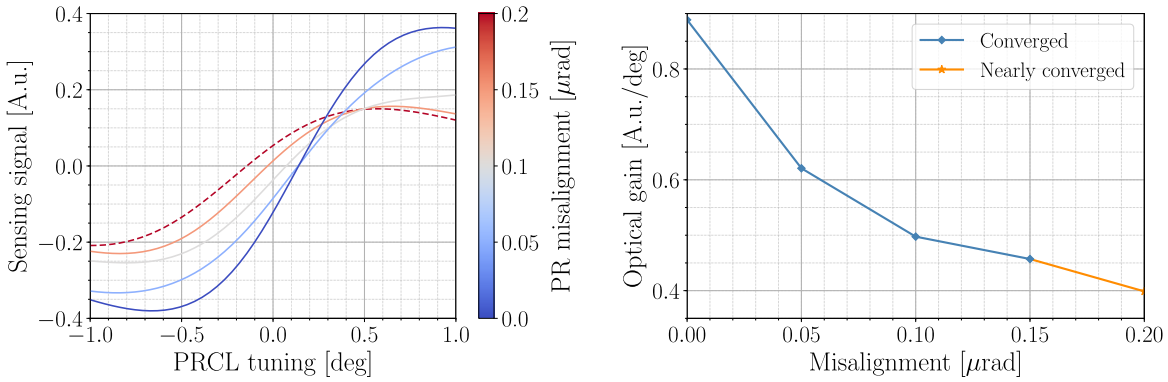

Figure 3.14: The figure shows simulated 132 MHz PRCL sensing signals for advanced Virgo at quarter-fringe with six different PR-misalignment values, modelled with finite mirrors. The right part shows the optical gains of these sensing signals, computed at the zero crossings.

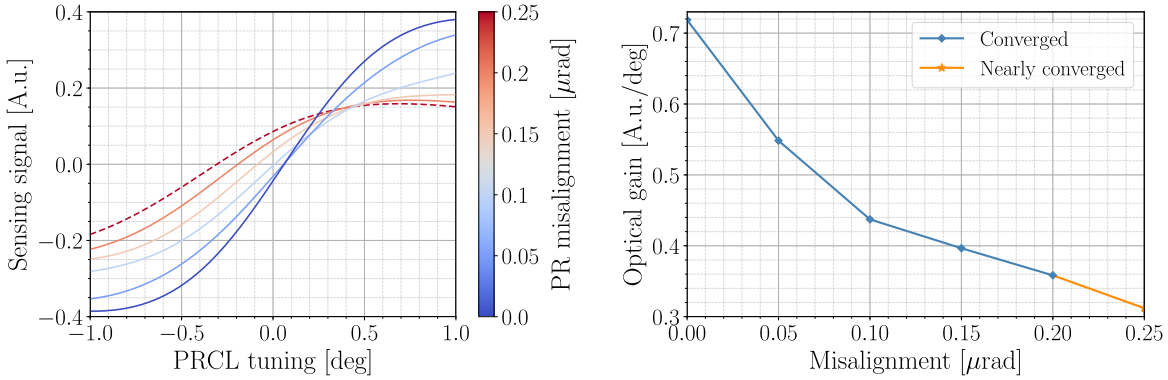

Figure 3.15: The figure shows simulated 132 MHz PRCL sensing signals for advanced Virgo at half-fringe with six different PR-misalignment values, modelled with finite mirrors. The right part shows the optical gains of these sensing signals, computed at the zero crossings.

sideband at the quarter fringe, while the opposite is true at the mid fringe. Therefore, the 132 MHz sidebands produces the better sensing signal at the mid fringe while the 119 MHz sidebands gives the better sensing signal at the quarter fringe, which can be confirmed by comparing figures 3.14 and 3.15 to figures 3.10 and 3.11 in section 3.3. From these figures we can also see that the PR-misalignments similarly affects the two pairs of sideband frequencies.

The procedure of computing the PRCL sensing signal by using the 132 MHz sidebands

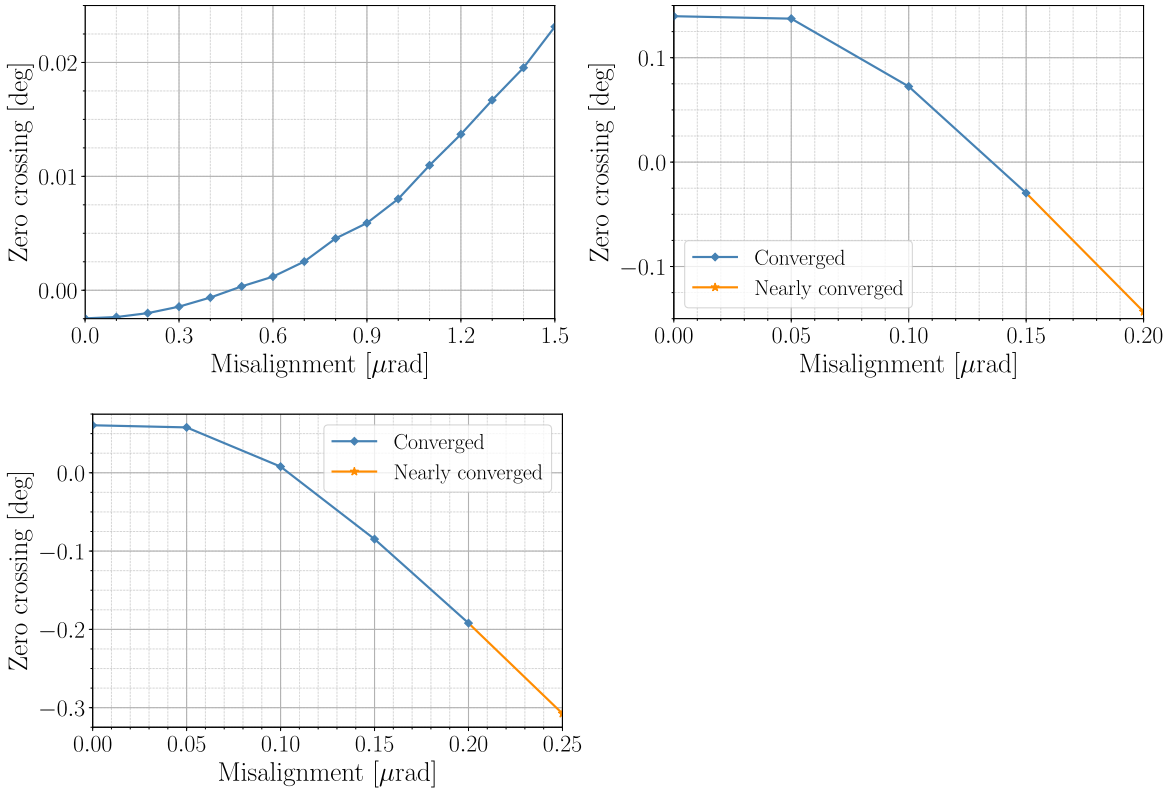

Figure 3.16: The figure shows how the zero-crossing—measured in PRCL tuning—varies with PR-misalignment magnitude. The upper left part shows the dark fringe, the upper right part shows the quarter fringe, and the bottom left part shows the mid fringe.

was the same as by using the 119 MHz sidebands, which is detailed in section 3.3. In short, finite PR, WI and NI mirrors were used, and it was made sure that enough spatial modes were included in the model for the sensing signals to converge. However—just as in 3.3—some sensing signals that only nearly satisfied the convergence condition are displayed in the figures in this section, which in these cases are clearly indicated.

As seen in figures 3.16, the zero-crossings of the 132 MHz sensing signals varies smoothly with respect to PR-misalignment magnitude, just as their 119 MHz counterparts shown in figure 3.12 in section 3.3.

3.5 Conclusion

In this chapter we have quantified how the Advanced Virgo PRCL sensing signal is affected by PR-misalignments during the lock acquisition phase where the MICH-offset is brought from the mid-fringe to the dark fringe. We have also studied the required number of included spatial higher-order modes in these simulations, where the aim was to better understand how this number is affected by the combination of a near-unstable cavity—like the Advanced Virgo PRC—and a misalignment. In the Virgo PRC, it turns out that the misalignment susceptibility of the sensing signal, and the required amount of higher-order modes for a given misalignment, depend on the same parameters: the PRC gains of the involved frequency components, and in particular their higher-order modes. Here, the involved frequency components are the carrier and the first-order pair of modulation sidebands. At the dark fringe, only the fundamental mode of the carrier has a high PRC-gain, therefore, the sensing signal is resilient to PR-misalignments and relatively few spatial modes are required. With a significant MICH-offset however, the sensing signal is highly susceptible to PR-misalignments, and relatively many higher-order modes are required. The reason is that the fundamental mode and many higher-order modes of one of the sidebands experience large PRC gains, while the carrier has a low PRC gain.

We also show that mirror clipping effects become significant when the required number of higher-order modes increases, which is because the spatial modes increasingly spread out in the transverse directions with increasing mode number. In our case, the threshold is around a mode order of 10.

In addition, we have shown that 119 MHz modulation sidebands do not perform significantly worse than the 132 MHz modulation sidebands for PRCL sensing, and that

they are similarly affected by PR-misalignments. This facilitated the decision making of switching from phase modulating on 132 MHz to 119 MHz.

CHAPTER 4

ALIGNMENT SENSING MODELLING FOR ADVANCED LIGO

The aim of the work described in this chapter was to create an up to date FINESSE [32, 33, 27] model of the LIGO Livingston gravitational wave detector that includes the alignment sensing scheme, and to develop accompanying tools in PyKat [34] that facilitate alignment related modelling for commissioning and design. The alignment sensing signals of the created model show relatively good agreement to measured data and to the modelling software Optickle [71].

To operate a gravitational wave detector in a stable manner, all mirrors must be well aligned with respect to each other and the laser beam. For example, the angular motion of the test masses should be suppressed to the order of 1 nrad RMS to maintain high detector sensitivity [72, 73]. An active alignment sensing and control (ASC) system is used to achieve this, however, it also allows noise in the angular degrees of freedom to couple to the gravitational wave channel DARM. ASC noise was in fact limiting the low frequency (10-15 Hz) displacement sensitivity of LIGO Livingston during the second observation run [74], which is one of the reasons for building this model.

The alignment sensing and control system used by Advanced LIGO is highly complex and its behaviour can be challenging to understand by experimenting on the detectors themselves. A numerical modelling software like FINESSE can be used to study the effects of a certain perturbation in the model, and therefore be useful in tracking down and explaining the cause of an observed effect. The FINESSE model is particularly suited for simulating transfer functions, where for example the ones mapping the Fourier-transforms of the degree-of-freedom motions, to the Fourier-transforms of the sensor outputs, can be used for investigating ASC noise couplings to the DARM channel.

The sensors of the ASC system consist of quadrant photo detectors (QPDs) and wavefront sensors (WFSs). A QPD is a photodetector that is split into four area elements (quadrants) which enables for measuring the beam position by comparing the amount of light power incident on the elements. A WFS is formed by demodulating the QPD signal at a modulation frequency. Such a device is sensitive to the angle difference between the two incident frequency components that are used to form the beat signal. Both QPD and WFS signals depend on the relative accumulated Gouy-phase between the fundamental mode and the first-order modes. As the Gouy-phase is a function of the longitudinal path between the misaligned optic and the photodetector, the misalignments of the different optics can be distinguished by placing QPDs and WFSs at different positions along the optical axis. Advanced LIGO uses both QPDs and WFSs, and their signals are used in control systems that filter and convert them into new signals that are fed back to the actuators that keep the mirrors aligned. However, here we solely focus on the sensing part of the scheme.

The core of the optical model that was created and used for the simulations described in this chapter, includes the dual-recycled Fabry-Perot Michelson interferometer, the in-

put and output mode cleaners, the main laser and two electro-optic phase modulators. These parts are included in the LIGO Livingston FINESSE-file distributed together with PyKat. Each alignment sensing port and the associated WFSs or QPDs, and the paths to these can be added to the model by a PyKat function. In addition, PyKat provides numerous functions that facilitate setting up and altering models, as well as performing various simulation tasks. For example, the main misalignment degrees of freedom are pre-defined objects with methods that can be used to quickly simulate both sensing signals due to static misalignments and frequency dependent transfer functions.

In section 4.1, the basics of misalignments and misalignment sensing are described in the modal picture. The misalignment degrees of freedom in general, and the eigenmodes of the arm cavities in particular, are explained in section 4.2. In section 4.3, the details of the created model are described, and in sections 4.4 and 4.5, the model is tested against measured data from LIGO Livingston, and against the simulation software Optickle.

4.1 Alignment sensing in the modal picture

If the axis defined by an optical structure (e.g. an optical cavity) does not coincide with the propagation axis of the laser beam, the beam and the optical structure are said to be misaligned with respect to each other. Any such misalignment can be described by a combination of an offset in the transverse plane and by a tilt of the same, as shown in

Figure 4.1: Any misalignment can be described by a combination of an offset and a tilt, as seen in left and right figures, respectively.

figure 4.1. As long as the paraxial approximation holds, the offset Δx is smaller than the beam size w, and the tilt β is smaller than the diffraction angle θ_D, any misaligned Gaussian beam can be described in the eigenbasis of the optical structure by using an infinite sum of Hermite-Gaussian modes. Thus, we can change the basis from the frame where the beam propagates along the z'-axis to a frame defined by the optical structure:

$$u_0'(x', z')\mathrm{e}^{-ikz'} = \sum_{m=0}^{\infty} k_{0m} u_m(x, z)\mathrm{e}^{-ikz}, \tag{4.1}$$

where the coupling coefficients k_{0m} are given by

$$k_{m'm} = \int_{-\infty}^{\infty} u_{m'}'(x', z') u_m^*(x, z)\mathrm{e}^{ik(z-z')}\,\mathrm{d}x. \tag{4.2}$$

This integral can be solved analytically even in the generic case [75], however, for simplicity we here assume that the waist of the two fundamental modes coincide at $z = 0$, and we perform the basis change at the waist position. This means that the curvature of the wavefront is $R_c(z') = R_c(z) = \infty$, the Gouy phase is $\psi(z') = \psi(z) = 0$, and the beam radius is $w(z') = w(z) = w_0$. For the case of an offset, the transformation between the two coordinate systems is described by

$$\begin{aligned} x' &= x - \Delta x \\ z' &= z. \end{aligned} \tag{4.3}$$

Thus, in the coordinate system defined by the optical structure, the spatial distribution of the beam in the plane of the waist is given by

$$\begin{aligned} u_0'(x - \Delta x, 0) = &\left(1 - \frac{1}{2}\frac{\Delta x^2}{w_0^2}\right) u_0(x, 0) + \left(\frac{\Delta x}{w_0} - \frac{1}{2}\frac{\Delta x^3}{w_0^3}\right) u_1(x, 0) + \frac{1}{\sqrt{2}}\frac{\Delta x^2}{w_0^2} u_2(x, 0) \\ &+ \frac{1}{\sqrt{6}}\frac{\Delta x^3}{w_0^3} u_3(x, 0) + \mathcal{O}\left(\frac{\Delta x^4}{w_0^4}\right), \end{aligned} \tag{4.4}$$

which is shown in appendix D, where the functions $u_m(x,z)$ are also found. In the case of a tilt, the coordinates are transformed according to

$$\begin{aligned} x' &= x\cos\beta \\ z' &= x\sin\beta. \end{aligned} \tag{4.5}$$

Note that this transformation is valid only at $z = 0$. By Taylor-expanding around $\beta = 0$, and keeping in mind that $\beta < \theta_D \ll 1$, we obtain

$$\begin{aligned} u_0'(x\cos\beta, x\sin\beta) = \left(1 - \frac{1}{2}\frac{\beta^2}{\theta_D^2}\right)u_0(x,0) - i\left(\frac{\beta}{\theta_D} - \frac{1}{2}\frac{\beta^3}{\theta_D^3}\right)u_1(x,0) - \frac{1}{\sqrt{2}}\frac{\beta^2}{\theta_D^2}u_2(x,0) \\ + i\frac{1}{\sqrt{6}}\frac{\beta^3}{\theta_D^3}u_3(x,0) + \mathcal{O}\left(\frac{\beta^4}{\theta_D^4}\right). \end{aligned} \tag{4.6}$$

Thus, to first-order, a misaligned Gaussian beam can be described by combining equations 4.4 and 4.6 into

$$\begin{aligned} u_0'(x\cos\beta - \Delta x,\, x\sin\beta) &\approx u_0(x,0) + \left(\frac{\Delta x}{w_0} - i\frac{\beta}{\theta_D}\right)u_1(x,0) \\ &= u_0(x,0) + (\kappa_1 + i\kappa_2)u_1(x,0), \end{aligned} \tag{4.7}$$

where $\kappa_1 = \frac{\Delta x}{w_0}$ and $\kappa_2 = -\frac{\beta}{\theta_D}$. By defining $\kappa = \sqrt{\kappa_1^2 + \kappa_2^2}$ and $\Theta = \tan^{-1}(\kappa_2/\kappa_1)$, the misaligned field can be written

$$u_0'(x\cos\beta - \Delta x,\, x\sin\beta) \approx u_0(x,0) + \kappa e^{i\Theta}u_1(x,0), \tag{4.8}$$

where $\Theta = 0$ gives a purely displaced beam ($\beta = 0$) and $\Theta = \pm\pi/2$ gives purely tilted beam ($\Delta x = 0$). As the beam propagates away from the waist, it can be shown that both κ_1 and κ_2 must be scaled by the factor $\frac{w_0}{w(z)}$ [76]. Hence, Θ remains constant during propagation while the magnitude κ can be redefined as $\kappa(z) \equiv \kappa\frac{w_0}{w(z)}$.

To describe the alignment sensing, an example of a laser field reflected off a misaligned cavity is used. The laser field incident on the input mirror of the cavity consists of three frequency components: a carrier with frequency ω, and two phase modulation sidebands with frequencies $\omega \pm \Omega$. The cavity has a small misalignment that is "seen" only from within the cavity. The carrier resonates in the cavity and is therefore susceptible to the misalignment, while the sidebands are anti-resonant and unaffected by it. If the cavity is lossless and the end mirror is perfectly reflective, the field reflected off the cavity is approximately given by

$$E_r(x,y) = a_0 \mathrm{e}^{i\omega t}\left[\left(\frac{ih}{2}\left(\mathrm{e}^{i(\Omega t+\phi_h)} + \mathrm{e}^{-i(\Omega t+\phi_h)}\right) - 1\right) u_0(x,z) - \kappa(z)\mathrm{e}^{i(\psi(z)+\Theta)} u_1(x,z)\right]. \tag{4.9}$$

Here, h is the modulation index and ϕ_h is the modulation phase plus any phase that the sidebands have picked up relative to the carrier due to propagation. This reflected field is detected by a QPD that integrates the intensities on the upper and lower parts of it. The intensity of this field is $I(x,z) = |E_r(x,z)|^2$, thus, the total powers at the upper and lower areas of the split photo detector are given by

$$\begin{aligned} P_1(z) &= \int_{-\infty}^{0} I(x,z)\,\mathrm{d}x \qquad \text{and} \\ P_2(z) &= \int_{0}^{\infty} I(x,z)\,\mathrm{d}x. \end{aligned} \tag{4.10}$$

Thus, the QPD output signal becomes

$$S = P_2(z) - P_1(z) = \frac{2\sqrt{2}\kappa P_0}{\sqrt{\pi} w(z)}\Big(\cos\big(\psi(z)+\Theta\big) - h\sin\big(\psi(z)+\Theta\big)\cos(\Omega t + \phi_h)\Big). \tag{4.11}$$

If this is a DC-detector, the signal is low pass filtered, i.e., the time dependent term

oscillating around zero is removed and one obtains

$$S_{\mathrm{QPD}} = \frac{2\sqrt{2}\kappa(z)P_0}{\sqrt{\pi}w(z)} \cos\big(\psi(z) + \Theta\big). \tag{4.12}$$

To generate a wavefront sensor signal, S is demodulated at the frequency Ω, which can be described as multiplying S with $\cos(\Omega t + \varphi_x)$ and subsequently applying a low pass filter. Thus, the WFS signal is given by the DC-terms of

$$S_1 = \frac{2\sqrt{2}\kappa P_0}{\sqrt{\pi}w(z)} \Big(\cos\big(\psi(z) + \Theta\big) - h \sin\big(\psi(z) + \Theta\big) \cos(\Omega t + \phi_h) \Big) \cos(\Omega t + \varphi_x), \tag{4.13}$$

where φ_x is the demodulation phase. The final expression for the WFS signal becomes:

$$S_{\mathrm{WFS}} = -\frac{\sqrt{2}P_0\kappa(z)h}{\sqrt{\pi}w(z)} \sin\big(\psi(z) + \Theta\big) \cos(\varphi_x - \phi_h). \tag{4.14}$$

By performing QPD or WFS measurement at two different locations along the z-axis that have a Gouy-phase difference of 90 degrees, and by using two different demodulation phases at each location, one can make the detectors sensitive to misalignments of specific optics.

4.2 Angular degrees of freedom

To define the angular degrees of freedom, LIGO uses a local coordinate system for each mirror, defined by three orthogonal unit vectors:

$\hat{\mathbf{z}}$ = normal to the HR-surface at the intersection with the optical axis, pointing towards the center of curvature,

$\hat{\mathbf{y}}$ = vertical and oriented upwards, and

$\hat{\mathbf{x}} = \hat{\mathbf{y}} \times \hat{\mathbf{z}}$. (4.15)

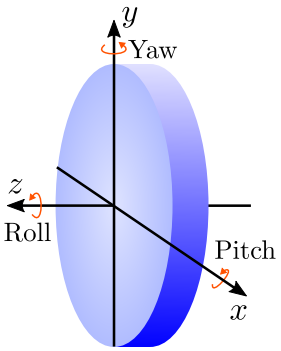

Figure 4.2: The figure shows the local coordinate system used for the LIGO mirrors, and the definitions of the angular degrees of freedom. The left hand side mirror surface is a concave HR-surface, and the origin is placed where this surface intersects the optical axis.

Each optic has three degrees of rotational freedom: pitch, yaw and roll. Pitch is a rotation about the x-axis (horizontal transverse axis), yaw is a rotation about the y-axis (vertical axis), and roll is a rotation about the z-axis (optical or longitudinal axis), as seen in figure 4.2. The roll-degree of freedom is not dealt with here as it does not give rise to misalignments of the beam, assuming the optics are symmetric around the z-axis.

The degrees of freedom of the test masses are commonly combined into degrees of freedom of the arm cavities. The definitions and the reason for using these, are described below. The focus here is on the pitch degree of freedom, although the same formalism applies to the yaw degree of freedom.

If the high-power beam in an arm cavity is vertically off-centre when impinging on a suspended test mass, it exerts a non-negligible radiation pressure torque about the x-axis. The two test masses in each arm cavity can be described as torsional pendulums, coupled via the laser-field induced radiation pressure that acts like a spring. Thus, the radiation pressure torque on the test masses can be written as a function of the pitch

misalignments:

$$\boldsymbol{\tau} = -\mathbf{K}\,\boldsymbol{\theta}, \tag{4.16}$$

where the torque vector $\boldsymbol{\tau}$, the alignment vector $\boldsymbol{\theta}$, and the torsional stiffness matrix $\mathbf{K}$ [77, 72, 78, 79] are defined as

$$\boldsymbol{\tau} = \begin{bmatrix} \tau_{\mathrm{ETM}} \\ \tau_{\mathrm{ITM}} \end{bmatrix}, \qquad \boldsymbol{\theta} = \begin{bmatrix} \theta_{\mathrm{ETM}} \\ \theta_{\mathrm{ITM}} \end{bmatrix}, \quad \text{and} \quad \mathbf{K} = \frac{2PL}{c(g_{\mathrm{ITM}} g_{\mathrm{ETM}} - 1)} \begin{bmatrix} g_{\mathrm{ITM}} & 1 \\ 1 & g_{\mathrm{ETM}} \end{bmatrix}. \tag{4.17}$$

Here, τ_{ETM} and τ_{ITM} are the radiation pressure torques on the mirrors when they are statically misaligned by pitch angles θ_{ETM} and θ_{ITM}, P is the intra-cavity power, L is the cavity length, c is the speed of light, and g_{ETM} and g_{ITM} are the geometric stability parameters of the cavity, given by

$$g_{\mathrm{ETM}} = 1 - \frac{L}{R_{\mathrm{ETM}}} \quad \text{and} \quad g_{\mathrm{ITM}} = 1 - \frac{L}{R_{\mathrm{ITM}}}. \tag{4.18}$$

The eigenvalues of $\mathbf{K}$ are

$$\begin{aligned} k_{\mathrm{S}} &= \frac{PL}{c\big(g_{\mathrm{ETM}} g_{\mathrm{ITM}} - 1\big)} \Big(g_{\mathrm{ETM}} + g_{\mathrm{ITM}} + \sqrt{(g_{\mathrm{ETM}} - g_{\mathrm{ETM}})^2 + 4} \Big) \\ k_{\mathrm{H}} &= \frac{PL}{c\big(g_{\mathrm{ETM}} g_{\mathrm{ITM}} - 1\big)} \Big(g_{\mathrm{ETM}} + g_{\mathrm{ITM}} - \sqrt{(g_{\mathrm{ETM}} - g_{\mathrm{ETM}})^2 + 4} \Big), \end{aligned} \tag{4.19}$$

and the corresponding eigenvectors are given by

$$v_{\mathrm{S}} = \begin{bmatrix} 1 \\ r \end{bmatrix} \quad \text{and} \quad v_{\mathrm{H}} = \begin{bmatrix} r \\ -1 \end{bmatrix}, \quad \text{where} \quad r = \frac{1}{2} \Big(g_{\mathrm{ETM}} - g_{\mathrm{ITM}} + \sqrt{\big(g_{\mathrm{ETM}} - g_{\mathrm{ITM}}\big)^2 + 4} \Big). \tag{4.20}$$

These two cavity eigenmodes are visualised in figure 4.3. The subscripts S and H on

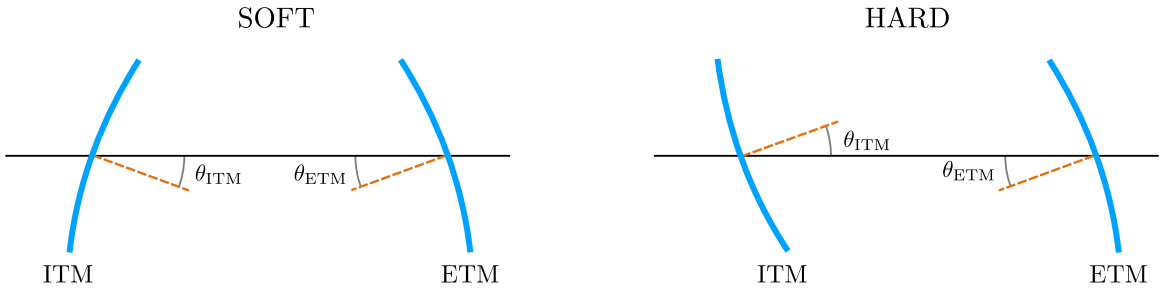

Figure 4.3: The figure shows the two independent eigenmodes of the torsional stiffness matrix $\mathbf{K}$. The soft mode is unstable and becomes less stiff with increasing radiation pressure torque and therefore relies on the restoring force from the suspension system, while the hard mode is stable and becomes stiffer with increasing radiation pressure torque.

the eigenvalues and eigenvectors stand for soft and hard, and are adopted from [72]. The names come from the fact that the radiation pressure makes the hard mode stiffer ($k_{\mathrm{H}} > 0$) , while it softens the soft mode ($k_{\mathrm{S}} < 0$). The soft mode becomes unstable if $k_{\mathrm{S}} + k_{\mathrm{sus}} < 0$, where $k_{\mathrm{sus}}^{\mathrm{P}} = 9.72$ Nm/rad is the restoring spring constant for the pitch mode due to the suspension [72]. This happens if the power in the arm cavities reach about 700 kW, which is below the design value of 750 kW [17]. To compute this limit, the parameter values $g_{\mathrm{ETM}} = -0.782$, $g_{\mathrm{ITM}} = -1.060$, and $L = 3994.4692$ m were used.

It follows from the eigenvectors in equation 4.20 that the hard and soft modes are related to the individual mirror rotations through

$$\begin{bmatrix} \theta_{\mathrm{S}} \\ \theta_{\mathrm{H}} \end{bmatrix} = \frac{1}{r^2+1} \begin{bmatrix} 1 & r \\ r & -1 \end{bmatrix} \begin{bmatrix} \theta_{\mathrm{ETM}} \\ \theta_{\mathrm{ITM}} \end{bmatrix}, \tag{4.21}$$

and in this eigenbasis, equation 4.16 takes the form

$$\begin{bmatrix} \tau_{\mathrm{S}} \\ \tau_{\mathrm{H}} \end{bmatrix} = - \begin{bmatrix} k_S & 0 \\ 0 & k_H \end{bmatrix} \begin{bmatrix} \theta_{\mathrm{S}} \\ \theta_{\mathrm{H}} \end{bmatrix}, \tag{4.22}$$

where the torsional stiffness matrix is diagonal. Since interferometer naturally dis-

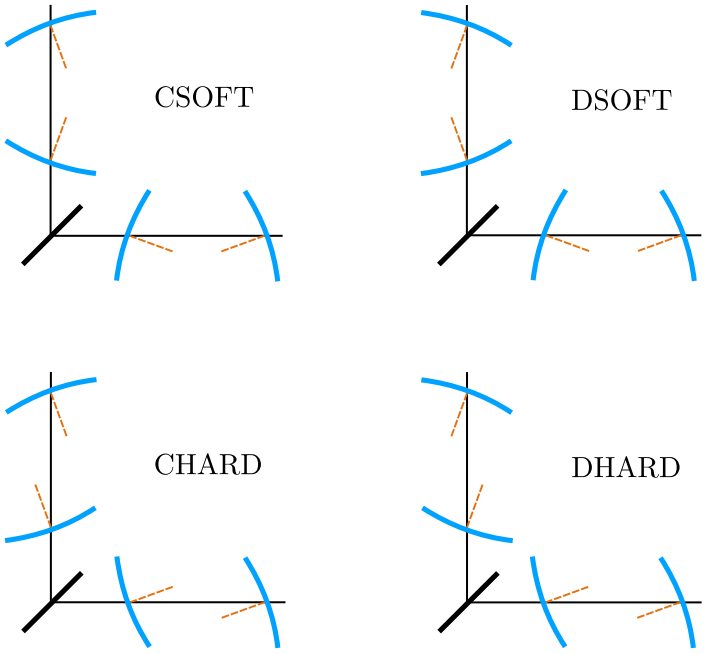

Figure 4.4: The figure shows the definitions of the four pitch or yaw degrees of freedom of the arm cavities.

tinguishes between common and differential motions of the arm cavities, the soft and hard modes are further combined into the common and differential hard and soft modes, which are defined as

$$\begin{bmatrix} \theta_{\mathrm{CS}} \\ \theta_{\mathrm{CH}} \\ \theta_{\mathrm{DS}} \\ \theta_{\mathrm{DH}} \end{bmatrix} = \frac{1}{2(r^2+1)} \begin{bmatrix} 1 & 1 & r & r \\ r & r & -1 & -1 \\ 1 & -1 & r & -r \\ r & -r & -1 & 1 \end{bmatrix} \begin{bmatrix} \theta_{\mathrm{EX}} \\ \theta_{\mathrm{EY}} \\ \theta_{\mathrm{IX}} \\ \theta_{\mathrm{IY}} \end{bmatrix}. \tag{4.23}$$

The subscripts CS and DH stand for common soft, and differential hard, respectively. These four modes of the arm cavities are shown in figure 4.4.

In addition to the modes of the arm cavities, the BS, PRM, SRM and the four telescope mirrors are also free to rotate. Thus, altogether there are 11 pitch degrees of freedom in the main interferometer, and just as many yaw degrees of freedom.

4.3 The Advanced LIGO Livingston Finesse-model with alignment sensing

The created model, shown in figure 4.5, is distributed together with PyKat within the IFO package. Here one finds the FINESSE-file that contains the dual-recycled Fabry-Perot Michelson interferometer, the input and output mode cleaners, the main laser, and two electro-optic modulators that generate the RF-sidebands used for sensing and control. One also finds a set of functions that add the various alignment and longitudinal sensing ports, and the paths to these, into the model. The IFO package also includes functions that facilitate setting up and modifying models and performing

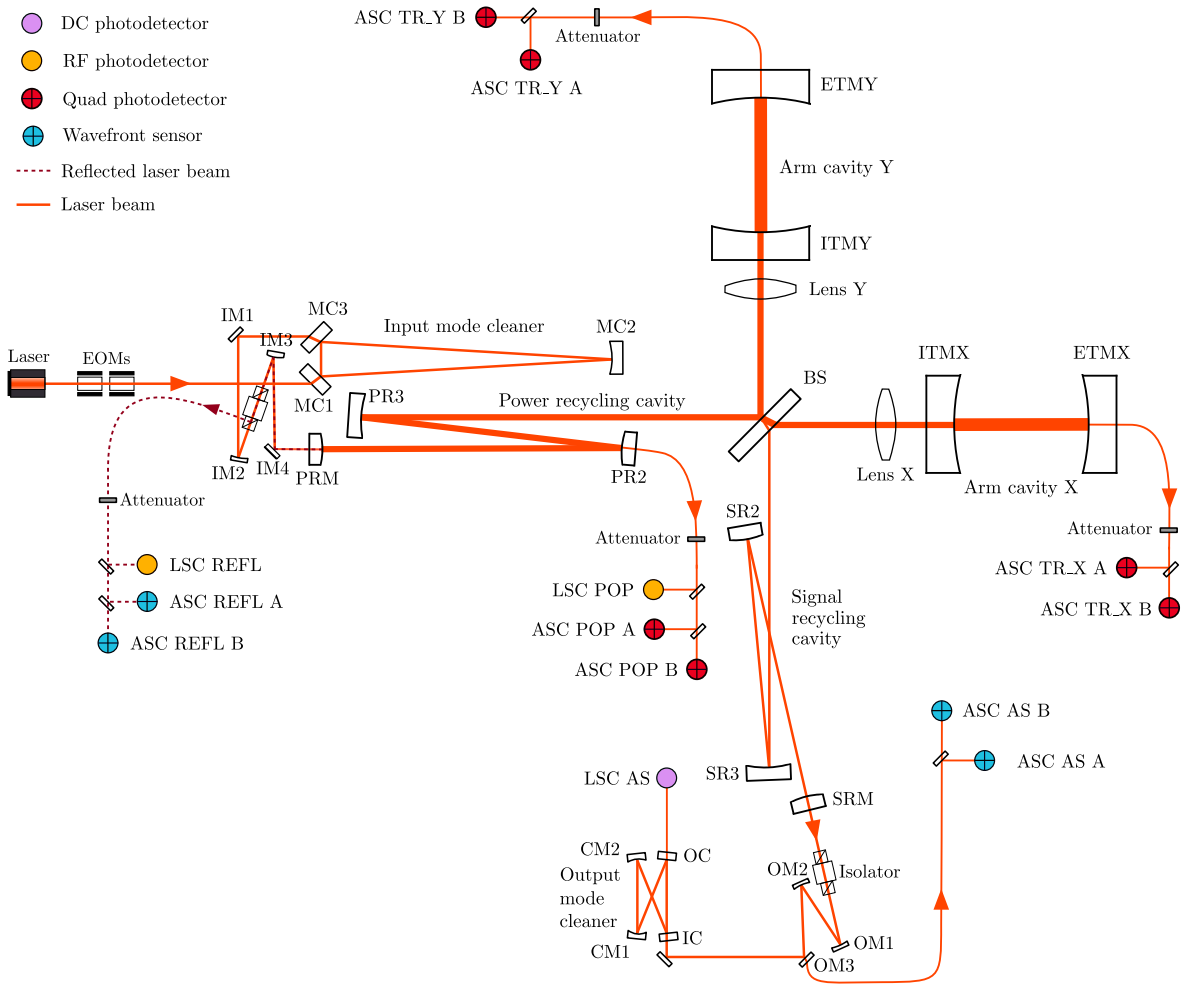

Figure 4.5: The figure is a visual representation of the LIGO Livingston FINESSE-model. The distances and the optics are not to scale.

simulations tasks, e.g., computing transfer function of the degrees of freedom to the sensing ports. The aim is to keep this model as up to date with the LIGO Livingston observatory as possible so that it can be used for commissioning. The parameters that are set in the model come from numerous sources such as logbook entries [80], the LIGO document control center (DCC) [81] and interferometer commissioners on site, of which Marie Kasprzack and Karla Ramirez were particularly valuable sources of information during this work. The PyKat IFO package was developed in collaboration with Daniel Brown, Andreas Freise and Anna Green, where I especially have contributed to the alignment modelling features.

4.3.1 Distances

The roundtrip lengths of the optical cavities are shown in table 4.1, and the optical path lengths between the optics that are used in the model are listed in table 4.2. The distance between PRM and PR2 was altered slightly compared to the official length [82] to match the FSR of the PRC to the measured value [83, 84]. Similarly, the distance between SR2 and SRM was tuned to match the listed total SRC length [82].

Table 4.1: Parameters of the optical cavities in the model. The PRC gain is with respect to the carrier, and m is the stability parameter.

	Roundtrip length [m]	FSR	FWHM [kHz]	Gain (Finesse)	m
X-arm	7988.9700 [82]	37.5258 kHz	0.0896	264.7 (418.6)	0.66
Y-arm	7988.9700 [82]	37.5258 kHz	0.0896	264.7 (418.6)	0.65
PRC	115.3174 [83, 84]	2.5997 MHz		37.1	0.64
SRC	112.0158 [82]	2.6763 MHz			0.78
IMC	32.9461 [85]	9.0995 MHz	17.4	166.6 (522.0)	-0.21
OMC	1.1314 [86]	264.97 MHz	645.6	122.8 (397.5)	0.19

Table 4.2: Optical path lengths used in the model. Based on [87, 82, 88].

Notation	Distance	Value [m]	Note
l_{im1}	MC3 $\leftrightarrow$ IM1	0.4282	
l_{im2}	IM1 $\leftrightarrow$ IM2	1.2938	Path from the IMC the the PRC. Based on [87].
l_{im3}	IM2 $\leftrightarrow$ IM3	1.17	
l_{im4}	IM3 $\leftrightarrow$ IM4	1.21	
l_{im4}	IM4 $\leftrightarrow$ PRM HR	0.5203	
L_{y}	ITMY HR $\leftrightarrow$ ETMY HR	3994.4850	
L_{x}	ITMX HR $\leftrightarrow$ ETMX HR	3994.4850	
l_{p1}	PRM $\leftrightarrow$ PR2	16.6130	The main interferometer distances. These are based on [82], but l_{p1} has been adjusted to match the FSR of the PRC [83, 84], and l_{s1} has been adjusted to match the listed SRC length [82].
l_{p2}	PR2 $\leftrightarrow$ PR3	16.1648	
l_{p3}	PR3 $\leftrightarrow$ BS HR	19.5380	
l_{y}	BS HR $\leftrightarrow$ ITMY HR	5.3020	
l_{x}	BS HR $\leftrightarrow$ ITMX HR	5.3838	
l_{s3}	BS HR $\leftrightarrow$ SR3	19.4652	
l_{s2}	SR3 $\leftrightarrow$ SR2	15.4435	
l_{s1}	SR2 $\leftrightarrow$ SRM	15.7563	
l_{om1}	SRM HR $\leftrightarrow$ OM1	3.7683	Path to the OMC. Based on [88], but some lengths have been altered to achieve a better spatial overlap between the OMC and the main interferometer.
l_{om2}	OM1 $\leftrightarrow$ OM2	1.395	
l_{om3}	OM2 $\leftrightarrow$ OM3	0.631	
l_{om4}	OM3 $\leftrightarrow$ IC	0.2034	
l_{pr}	$l_{\mathrm{p1}} + l_{\mathrm{p2}} + l_{\mathrm{p3}}$	52.3158	
l_{sr}	$l_{\mathrm{s1}} + l_{\mathrm{s2}} + l_{\mathrm{s3}}$	50.6650	
l_{M}	$(l_{\mathrm{x}} + l_{\mathrm{y}})/2$	5.3429	
Δl_{M}	$l_{\mathrm{x}} - l_{\mathrm{y}}$	0.0818	

4.3.2 Transmissivities, reflectivities and losses

The transmissivities, reflectivities, and losses used in the model are listed in tables 4.3 and 4.4. Since the AR-surfaces are wedged in reality, the listed AR-surface reflectivities are set as AR-surface losses in the model. The losses of the test masses and the BS have been altered compared to the values listed in [89], to reduce the PRC gain from around 80 to the measured value that is around 37 [90, 91]. The power gains and cavity finesses of the cavities are shown in table 4.1.

4.3.3 RoCs and spatial mode matching

The cavities in the model are spatially mode matched to each other to a level of 99.9 % or better, and the mode matching between the arm cavities and the PRC exceed 99.99 %. To achieve this, the ITM lenses (Lens X and Lens Y) were used to slightly improve the mode matching between the arms, the RoCs of PR3 and SR3 were used to mode match the recycling cavities to the arms, and the RoCs of OM1, OM2, IM2 and IM3 were used to match the mode cleaners to the main interferometer. The radii of curvature and focal lengths used in the FINESSE-model are listed in table 4.3.

Table 4.3: Radii of curvature (RoC), transmissivities (T), reflectivities (R), losses (L), masses (M), and thicknesses (Th) of the core opticsl. All values except the thicknesses are from [89]. The values marked with asterisks (*) were altered to mode match the PRC and SRC to the arms, and to match measured cavity gains. The compensation plates are excluded from the model, but their reflectivities and losses are included as extra losses in ITM AR surfaces. The lenses are included to model ITM thermal and substrate lensing. The listed focal lengths were chosen to match the arms to each other.

Optic	Surface	RoC [m]	R [ppm]	T	L [ppm]	M [kg]	Th [cm]
ETMX	HR	2239.7		3.7 ppm	31*	39.620	19.992 [92]
	AR	∞	200		-		
ETMY	HR	2242.4		3.6 ppm	31*	39.564	20.0 [89]
	AR	∞	230		-		
ITMX	HR	-1937.9		0.0148	62*	39.603	19.996 [93]
	AR	∞	164		0.5		
ITMY	HR	-1940.7		0.0148	62*	39.420	19.929 [94]
	AR	∞	250		0.6		
BS	HR	∞		0.5	8.6	14.211	6.012 [95]
	AR	∞	30		1.7		
PRM	HR	11.009		0.031	5.9	2.890	7.37 [96]
	AR		26		11.45		
SRM	HR	-5.673		0.324	7.4	2.898	7.355 [97]
	AR		21.5		0.6		
CPX	S1	∞	33		0.6		10.01 [98]
	S2	∞	8		0.6		
CPY	S1	∞	67		0.55		10.00 [99]
	S2	∞	15		0.57		
PR2	HR	-4.545		243 ppm	8.6	2.899	
PR3	HR	36.016*		5.3 ppm	17	12.145	
SR2	HR	-6.406		18.3 ppm	6.1	2.888	
SR3	HR	35.958*		5 ppm	19.1	12.069	
Lens X		$f = 108$ km	0	1	0		0
Lens Y		$f = 124$ km	0	1	0		0

Table 4.4: Auxiliary optics used in the model. The losses of the OMC optics were picked so that the cavity finesse matches the measured value of 397 [86]. The RoCs of IM2, IM3, and OM1 have been optimised to maximise the spatial mode matching of the IMC and OMC to the arm cavities. The values with asterisks (*) were arbitrarily picked.

Optic	RoC [m]	R	T	L	Source
IC	∞		0.00760	134 ppm	[86]
OC	∞		0.00754	134 ppm	
CM1	2.57321		36.0 ppm	134 ppm	
CM2	2.57369		35.9 ppm	134 ppm	
MC1	101.609 km		6150 ppm	10 ppm*	[89]
MC2	27.178		3.5 ppm	12 ppm	
MC3	171.747 km		6130 ppm	10 ppm*	
IM1	∞	1*			[100]
IM2	12.418	1*			
IM3	-6.108	1*			
IM4	∞	1*			
OM1	4.444		800 ppm	37.5*	[88]
OM2	1.7		10 ppm*	37.5*	
OM2	∞	0.99		37.5*	

4.3.4 Tunings and resonances

The PyKat IFO package includes functions for tuning the model to its operating point in three steps:

1. The microscopic positions (tunings) of the test masses, the PRM, and the SRM are optimised to (i) maximise the carrier power in the arm cavities and the PRC,

(ii) minimise the power in the asymmetric port, and (iii) to make the carrier anti-resonant in the SRC.

2. A DARM offset of δEX$-\delta$EY $= 10^{-11}$ m was added to allow for some of the carrier field to leak out through the dark port, which is necessary for DC readout [22] at the asymmetric port. Here, δEX and δEY are the microscopic positions of the end test masses.

3. The model should now be close to its operating point. The longitudinal sensing signals are added and used to iteratively bring the model to a state where all sensing signals are sufficiently close to their zero crossings. The operating point is found.

4.3.5 The alignment sensing ports

Each alignment sensing port has either two QPDs or two WFSs labelled A and B, and a beam splitter dividing the beam between the two detectors. There are also various optics that together serve several purposes, of which two were of interest for this work: attenuating the beam and especially accumulating the desired Gouy-phase in the path to the detectors. FINESSE has the feature of assigning the property of accumulated Gouy-phase directly to the space-components, which overwrites the Gouy-phase that otherwise would have been accumulated. Thus, to lower the complexity of the model, the optics in the path were reduced to comprise the beam splitter and one lossy optic. Gouy-phases are assigned to three different space components: ψ_{A} to the space between the beam splitter and detector A, ψ_{B} to the space between the beam splitter and detector B, and ψ_{C} to the path between the lossy optic and the beam splitter. Ideally, the Gouy-phase difference between the locations of the two detectors should be $\psi_{\mathrm{B}} - \psi_{\mathrm{A}} = 90$ deg, and ψ_{C} should be set such that the response of detector A or B is maximised or minimised for some degree of freedom. The losses and Gouy-phases

used for the particular ASC ports are described below, and summarised in table 4.5.

Table 4.5: The table shows the parameters used in the alignment sensing paths. The attenuations are from the main interferometer to the ASC beam spitters. The total accumulated Gouy-phase from the main interferometer to detectors A and B are given by $\psi_A + \psi_C$ and $\psi_B + \psi_C$.

ASC Port	Attenuation	ψ_A [deg]	ψ_B [deg]	ψ_C [deg]
REFL	0.9775	0	80	126.4
AS	0	0	90	22
POP	0.9	0	90	32
TR X	0.95	0	90	32
TR Y	0.95	0	90	32

For the ASC REFL port, the beam reflected off the PRM is obtained from the Faraday isolator between IM3 and IM2 in Horizontal Access Module 2 (HAM2) [101] (note that the mirrors IM1, IM2, IM3, and IM4 are referred to as SM1, PMMT1, PMMT2 and SM2 in [101]) and is sent to HAM1 [102] where the ASC REFL WFSs are located. This path is modelled using a power loss of 0.9775 [103] from the isolator to the WFS beam splitter. The accumulated Gouy-phases were set to $\Delta\psi_{\mathrm{REFL,A}} = 0$, $\Delta\psi_{\mathrm{REFL,B}} = 80$ and $\Delta\psi_{\mathrm{REFL,C}} = 126.4$. The first two were picked to have a difference of 80 deg [91] between the A and B sensors, and the value of $\Delta\psi_{\mathrm{REFL,C}}$ was unknown and was therefore optimised to give the best match to measured alignment sensing signals, as shown in section 4.4. The REFL wavefront sensors use demodulation frequencies of 9.099471 MHz (9 MHz) and 45.497355 MHz (45 MHz) [104].

The beam used in the ASC AS port is transmitted through OM3, and there are no lossy elements in this path [88]. We had no knowledge of measured Gouy-phases in this path, so the design values [87] of $\Delta\psi_{\mathrm{AS,A}} = 0$, $\Delta\psi_{\mathrm{AS,B}} = 90$ and $\Delta\psi_{\mathrm{AS,C}} = 22$ were

used. The WFSs use demodulation frequencies of 36.397884 MHz (36 MHz) and 45 MHz [104].

In the ASC POP port, QPDs are used to detect the DC signal. The beam is transmitted through PR2 in HAM3 [105] before it is guided to HAM1 [102] where the QPDs are located. The total loss from PR2 to the beam splitter is 0.9 [103], and the Gouy phases are set to the design values $\Delta\psi_{\mathrm{POP,A}} = 0$, $\Delta\psi_{\mathrm{POP,B}} = 90$ and $\Delta\psi_{\mathrm{POP,C}} = 32$ [87].

The ASC TR_X and TR_Y QPDs that are located in TRANSMON EX [106, 107] and TRANSMON EY [108, 107] use the beams transmitted through ETMX and ETMY, respectively. These beams experience a power loss of 0.95 between the ETMs and the ASC beam splitter [103], and the Gouy-phases were set to $\Delta\psi_{\mathrm{TR\_X,A}} = \Delta\psi_{\mathrm{TR\_Y,A}} = 0$ deg, $\Delta\psi_{\mathrm{TR\_X,B}} = \Delta\psi_{\mathrm{TR\_Y,B}} = 90$ deg and $\Delta\psi_{\mathrm{TR\_X,C}} = \Delta\psi_{\mathrm{TR\_Y,C}} = 32$ deg [87].

4.4 Comparison between the Finesse-model and measured data

To test the model, it was compared to measured LIGO Livingston data [91]. This data comprises the responses of the REFL WFSs to the PRC2, CHARD and CSOFT pitch degrees of freedom, where PRC2 refers to the angular degree of freedom of PR2. The REFL WFSs use 9 MHz and 45 MHz as demodulation frequencies, and their in-phase demodulation phases were set to maximise the response to CHARD. All measurements were made in the in-phase demodulation quadrature, at 7.125 Hz, and with 10 W input laser power.

Before generating the corresponding data with the FINESSE-model, the losses in the REFL path were adjusted to reduce the power on the REFL WFSs from 1.5 mW to the measured 1.0 mW on REFL A and 1.1 mW on REFL B [91]. This was done by increasing the attenuation factor between the interferometer and the ASC REFL beam spitter from 0.9775 to 0.98375, and by adding an extra loss of 0.04 in the path to REFL A.

The absolute accumulated Gouy-phase was to the best of my knowledge not known at the time of this work. Therefore, the parameter ψ_{C} of the model was optimised to achieve the best fit to the measured data by means of the standard method of least squares. Thus, the cost function that was minimised is given by

$$D(\psi_{\mathrm{C}}) = \frac{1}{11}\sqrt{\sum_{i=1}^{4}\sum_{j=1}^{3}\frac{\left(y_{ij}(\psi_{\mathrm{C}}) - \bar{y}_{ij}\right)^2}{\bar{y}_{ij}^2}}, \tag{4.24}$$

where $y_{ij}(\psi_{\mathrm{C}})$ and $\bar{y}_{ij}$ are the simulated and measured data points, and i and j label the sensors and the degrees of freedom. The response of REFL B to CSOFT, demodulated

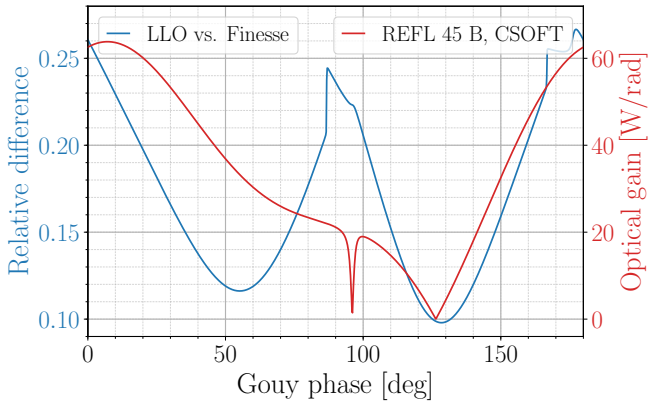

Figure 4.6: The blue trace shows the relative difference between the measured and simulated sensing matrices, plotted against the Gouy-phase picked up between the interferometer and the ASC REFL beam splitter. The relative differences are computed using equation 4.24. The red trace shows the response of REFL B 45 MHz to CSOFT, which is excluded from the blue trace as the measured value is zero.

at 45 MHz, was omitted in the cost function as the measured value was listed as zero [91]. Having this response close to zero was instead added as a second condition in the search for an optimal ψ_C. Figure 4.6 shows the cost function (blue trace) and the magnitude of the REFL B 45 MHz response to CSOFT (red trace) as functions of the common Gouy-phase ψ_C, and one can see that the global minima of the two functions nearly coincide. From this, an accumulated Gouy-phase of $\psi_C = 126.4$ deg was chosen and used in the simulations that generated the data in table 4.6. The relative differences between the measured and simulated data are shown in table 4.7,

WFS \ DoF	PRC2	CHARD	CSOFT
REFL A, 9 MHz	-83.18	3714.24	552.84
REFL A, 45 MHz	28.60	1958.96	-36.48
REFL B, 9 MHz	-60.86	4010.30	466.38
REFL B, 45 MHz	16.91	1414.93	0.002

Table 4.6: Simulated responses of the in-phase REFL alignment sensing signals to three different pitch degrees of freedom. For each detector, the demodulation phase is set such that CHARD is maximised. The unit is W/rad.

and were computed by using the formula

$$d_{ij} = \frac{y_{ij} - \bar{y}_{ij}}{\bar{y}_{ij}}. \tag{4.25}$$

Since $y_{ij}\bar{y}_{ij} \geq 0$ for all i and j, the relative difference d_{ij} is positive (negative) if the magnitude of the simulated value y_{ij} is greater (less) than the magnitude of the measured value $\bar{y}_{ij}$. The element in the lower right corner of table 4.7 was omitted because the measured value is listed as zero, however, one can see from table 4.6 that the simulated value is close to zero as well. All measured non-zero values have relative uncertainties below 6 % [91].

WFS \ DoF	PRC2	CHARD	CSOFT
REFL A, 9 MHz	-0.160	-0.165	0.108
REFL A, 45 MHz	0.589	-0.202	-0.668
REFL B, 9 MHz	-0.002	0.062	0.234
REFL B, 45 MHz	-0.471	-0.015	

Table 4.7: Relative differences between the measured [91] and FINESSE-generated (see table 4.6) REFL responses to three different pitch degrees of freedom.

4.5 Comparison between Finesse and Optickle

To test the responses of more WFSs to additional degrees of freedom, a second comparison was made to the simulation software Optickle [71], using a modified version of a model created and provided by Marie Kasprzack and Karla Ramirez. Optickle is frequency domain simulation software developed independently of FINESSE , but uses a similar approach to simulate interferometers. It is capable of generating first-order

HG-modes for misalignment modelling, but otherwise propagates plane waves through the optical system. Thus, Optickle is unaffected by spatial mode mismatches and therefore a perfect agreement between FINESSE and Optickle is impossible unless the optical cavities in the model are perfectly spatially mode matched. The model used here has well matched optical cavities (> 99.99 %), but even such small mismatches affect the alignment signals. Further, the FINESSE model has realistic thick mirrors and accounts for composite mirror effects [109] when generating the higher-order modes due to misalignments, which the thin mirrors used by Optickle does not account for. This effect however, is small for the optics used here. Besides these inherent differences, the parameters of the models were made identical for this comparison.

The comparison was made by computing the responses of the WFSs in the REFL and AS ports to quasi-static (low frequency) motions of the pitch eigenmodes of the arm cavities. The demodulation phases were set such that the in-phase responses to CHARD were maximised in the REFL WFSs and the in-phase responses to DHARD are maximised in the AS WFSs. For each combination of WFS and degree of freedom, the in-phase and quadrature responses S_I and S_Q can be combined into the complex number

$$S = S_I + iS_Q, \tag{4.26}$$

that contains information on the optimal demodulation phase and the maximum optical gain. Graphical representations of these complex numbers, obtained using FINESSE (black solid bars) and Optickle (red dashed bars), are shown in figure 4.7. The length of each bar is given by $\log_{10}(|S|)$ and the angle by $\arg(S)$. As a result of having optimised the in-phase optical gain for CHARD in the REFL port, and for DHARD in the AS port, the CHARD bars for FINESSE and Optickle perfectly coincide at 0 deg for all REFL WFSs, as do the DHARD bars for all AS WFSs. The relative magni-

tude differences between FINESSE and Optickle are shown in table 4.8, and the phase differences in table 4.9. The most eye-catching differences are the nearly 180 degree phase differences for DSOFT at the REFL 9 MHz sensor and for CSOFT at the AS 45 MHz sensor. These are however, relatively weak responses, and the differences arise from small relative differences between large responses to individual mirror motions that compose the pitch eigenmodes. This is backed up by figure 4.8, which shows the WFS responses to individual test mass motions. The relative magnitude differences and the absolute phase differences between FINESSE and Optickle are listed in tables 4.10 and 4.11. The differences between FINESSE and Optickle are believed to be explained by the fact that FINESSE is affected by the spatial mode mismatches, while Optickle is not. An indication of this is that the relative differences changes in the order of 10^{-2} when switching between including spatial modes up to order one and two in the FINESSE simulations.

WFS \ DoF	CSOFT	CHARD	DSOFT	DHARD
REFL A, 45 MHz	5.1×10^{-3}	6.5×10^{-3}	-2.5×10^{-3}	1.4×10^{-2}
REFL B, 45 MHz	-6.8×10^{-3}	5.9×10^{-3}	4.3×10^{-2}	-1.8×10^{-1}
REFL A, 9 MHz	5.3×10^{-3}	4.3×10^{-3}	-1.3×10^{-1}	1.9×10^{-1}
REFL B, 9 MHz	5.9×10^{-3}	4.1×10^{-3}	7.7×10^{-2}	-3.7×10^{-1}
AS A, 36 MHz	-4.6×10^{-2}	-4.6×10^{-2}	8.8×10^{-2}	9.4×10^{-2}
AS B, 36 MHz	-4.5×10^{-1}	-4.6×10^{-1}	1.9×10^{-2}	2.0×10^{-2}
AS A, 45 MHz	-3.4×10^{-2}	1.2	-6.2×10^{-2}	-5.9×10^{-2}
AS B, 45 MHz	4.2×10^{-1}	-2.5×10^{-1}	-1.5×10^{-1}	-1.5×10^{-1}

Table 4.8: Relative magnitude differences between the FINESSE and Optickle simulated WFS responses to the pitch eigenmodes of the arm cavities.

WFS \ DoF	CSOFT	CHARD	DSOFT	DHARD
REFL A, 45 MHz	-0.550	0.000	5.904	3.411
REFL B, 45 MHz	-0.411	0.000	8.183	-11.346
REFL A, 9 MHz	0.032	0.000	174.934	0.187
REFL B, 9 MHz	0.035	0.000	-164.752	0.313
AS A, 36 MHz	4.721	4.767	-0.679	0.000
AS B, 36 MHz	12.607	13.887	0.004	0.000
AS A, 45 MHz	179.199	-0.153	-11.405	0.000
AS B, 45 MHz	178.472	-0.353	-12.053	0.000

Table 4.9: The phase differences between the FINESSE and Optickle simulated WFS responses to the pitch eigenmodes of the arm cavities. The unit is degrees.

WFS \ DoF	ETMX	ETMY	ITMX	ITMY
REFL A, 45 MHz	5.4×10^{-3}	7.5×10^{-3}	1.2×10^{-2}	1.2×10^{-3}
REFL B, 45 MHz	-3.0×10^{-3}	1.6×10^{-2}	2.3×10^{-3}	8.8×10^{-3}
REFL A, 9 MHz	3.4×10^{-3}	5.5×10^{-3}	1.2×10^{-2}	-3.5×10^{-3}
REFL B, 9 MHz	-5.0×10^{-3}	1.4×10^{-2}	5.8×10^{-4}	7.2×10^{-3}
AS A, 36 MHz	-1.5×10^{-1}	-1.5×10^{-1}	5.6×10^{-2}	1.6×10^{-1}
AS B, 36 MHz	-3.5×10^{-2}	-3.3×10^{-2}	1.6×10^{-2}	2.3×10^{-2}
AS A, 45 MHz	-5.7×10^{-2}	-6.1×10^{-2}	-4.2×10^{-2}	-7.5×10^{-2}
AS B, 45 MHz	-1.5×10^{-1}	-1.5×10^{-1}	-1.5×10^{-1}	-1.5×10^{-1}

Table 4.10: Relative magnitude differences between the FINESSE and Optickle simulated WFS responses to test mass motions.

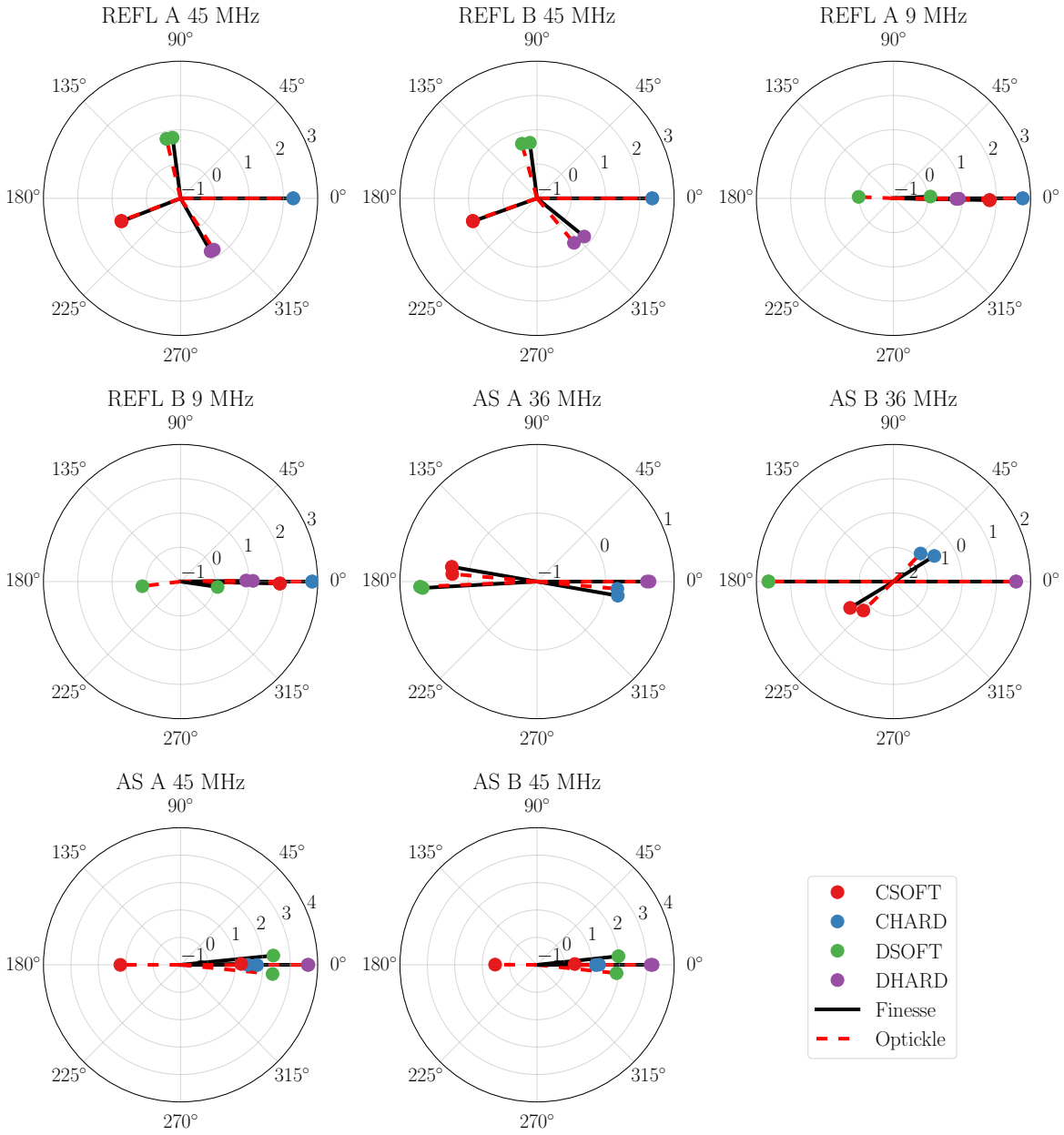

Figure 4.7: Each of the 8 polar plots represents the responses to quasi-static motions of the arm cavities' pitch eigenmodes of a particular WFS, as indicated by the labels. The data is obtained by FINESSE (black solid bars) and Optickle (red dashed bars). The length and angle of each bar is given by the logarithm of the optical gain (W/rad), and the demodulation phase (degrees) that maximises the in-phase response, respectively.

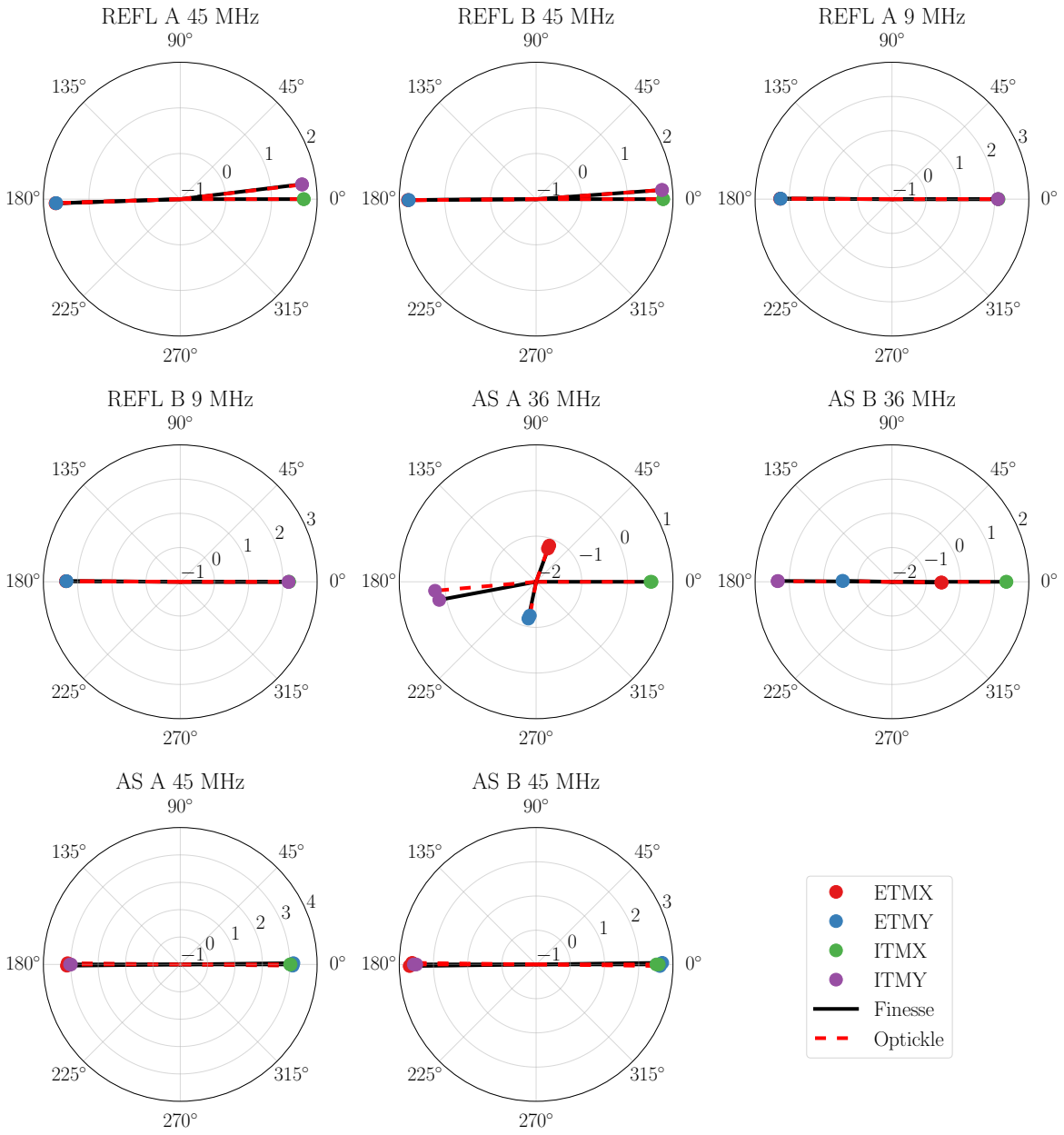

Figure 4.8: The figure represents the WFS responses to quasi-static test mass motions, as simulated by FINESSE (black solid bars) and Optickle (red dashed bars). The length and angle of each bar is given by the logarithm of the optical gain (W/rad), and the demodulation phase (degrees) that maximises the in-phase response, respectively.

WFS \ DoF	CSOFT	CHARD	DSOFT	DHARD
REFL A, 45 MHz	-0.069	-0.068	0.000	-0.185
REFL B, 45 MHz	0.066	0.066	0.000	0.012
REFL A, 9 MHz	0.004	0.004	0.000	-0.005
REFL B, 9 MHz	0.010	0.010	0.000	0.004
AS A, 36 MHz	0.462	1.430	0.000	-5.535
AS B, 36 MHz	0.130	0.181	0.000	0.117
AS A, 45 MHz	-1.262	-1.262	0.000	0.014
AS B, 45 MHz	-1.448	-1.450	0.000	0.026

Table 4.11: The phase differences between the FINESSE and Optickle simulated WFS responses to test mass motions. The unit is degrees.

4.6 Conclusion

A FINESSE-model of the Advanced LIGO Livingston observatory that includes the alignment sensing scheme was built, and accompanying tools were developed within the PyKat-package to facilitate the use of the model for commissioning and design modelling. The model was tested against measured data and the average relative difference was 24 %, however, 8 out of the 11 values were below the average.

proved to agree relatively well with it. The comparison however, only included the responses of the REFL WFSs to three different degrees of freedom. For this reason, the result of this limited test should not be exaggerated. In addition, the model was compared to a nearly identical model in the simulation software Optickle, which allowed for testing more readout ports, and their responses to all arm cavity degrees of freedom. The two simulation softwares showed a good agreement, and the small differences can likely be explained by the spatial mode mismatches between the optical cavities that FINESSE is susceptible to, while Optickle is not.

Future work includes exploring alternative sensing schemes, and using the model to try to mitigate the ASC noise couplings into DARM, which currently limits LIGO Livingston at low frequencies.

CHAPTER 5

SUMMARY, CONCLUSIONS AND FUTURE WORK

This thesis reports on the effects that higher-order modes, arising due to spatial mismatches and misalignments, have on interferometric gravitational wave detectors. All of the work presented is related to commissioning and/or design modelling of these detectors, either directly through modelling work, or by developing numerical tools that enable or facilitate commissioning and design modelling for others.

Chapter 2 shows how a gravitational wave detector, enhanced by frequency-dependent squeezed light, is affected by spatial mode mismatches between the squeezer, the filter cavity, and the interferometer. We show that spatial mismatches can turn squeezed light into anti-squeezed light by scattering from the fundamental mode to a higher-order mode, and then back. This can degrade the squeezed field by significantly more than an equivalent loss. We also propose a way of mitigating spatial mismatch induced squeeze degradation by injecting squeezed higher-order modes in addition to the squeezed fundamental mode. The reason for this is that a mode mismatch would then make the fundamental mode trade squeezed light for squeezed light, instead of trading squeezed light for vacuum noise. This is shown using a realistic model of Advanced

LIGO. To use multiple squeezed modes in reality, multiple squeezers are needed, and the multiple squeezed beams need to be superimposed on each other without too much loss. We also experimentally show that the proposed scheme works when the mismatch is a misalignment, and the additional squeezed mode is a first order mode.

Chapter 3 reports on the effects that power recycling mirror misalignments have on the power recycling cavity length sensing signal during lock acquisition at Virgo. During the lock acquisition phase, the interferometer is brought from mid-fringe to the dark fringe, without the auto-alignment system for the power recycling mirror being engaged. It turns out that the optical gain of the sensing signal grows slightly with increasing misalignment at the dark fringe, while it decreases quickly with increasing misalignment when far off from the dark fringe. The reason is related to the fact that the power recycling cavity is near-unstable, and that the carrier field is resonant in the arm cavities, while the RF-sidebands are not. This chapter also shows the importance of making sure that enough higher-order modes are included in the model for the simulation to converge, and in which situations the required number of included spatial modes are expected to be particularly high. Future work includes using the Virgo model and the developed PyKat tools to investigate if there are potentially better ways of using the information from the longitudinal sensors in the the longitudinal control scheme.

Chapter 4 describes the FINESSE model of LIGO Livingston that was developed mainly for the purpose of commissioning and design modelling of the alignment sensing system. It can, however, be used for any other LIGO Livingston modelling work that FINESSE is capable of. The model consists of the FINESSE-file, that contains the core optics, and a set of PyKat functions that facilitate making modifications, such as adding/removing readout ports, and performing simulations. This chapter also reports on a successful test against measured data on how the REFL wavefront sensors respond to motions of

the misalignment degrees of freedom. In addition, the model was successfully tested against the simulation software Optickle, which allowed for comparing more combinations of readout ports and misalignment degrees of freedom. One of the reasons for building this model is that LIGO Livingston currently is limited by misalignment couplings into the gravitational wave channel at the low end of the gravitational wave bandwidth. Future work includes using the FINESSE model to look into the reason for this, and exploring the available information in the alignment sensing matrix to see if there are better ways of controlling the interferometer.

Appendices

APPENDIX A

NOISE SCALING OF THE COHERENT SCATTERING EFFECT

In this section we derive how the noise due to the coherent scattering effect scales with the coupling coefficient. We use a simplified version of the system considered in section 2.1.2 where the filter cavity is mode-mismatched to the interferometer and the squeezer, while the squeezer and the interferometer are kept mode matched. Here, we only use two fields, i.e., $N = 1$ in the mathematical framework in section 2.1.2. The relation between the output field and the input field is given by equation 2.18, but where the matrices are simplified.

Only one of the two fields is squeezed, thus, the squeezing matrix can be written as

$$S = \begin{bmatrix} \mathrm{e}^{r} & 0 & 0 & 0 \\ 0 & \mathrm{e}^{-r} & 0 & 0 \\ 0 & 0 & 1 & 0 \\ 0 & 0 & 0 & 1 \end{bmatrix}. \tag{A.1}$$

The scattering matrix is given by

$$\mathcal{K} = \begin{bmatrix} \cos\kappa & 0 & -\sin\kappa & 0 \\ 0 & \cos\kappa & 0 & -\sin\kappa \\ \sin\kappa & 0 & \cos\kappa & 0 \\ 0 & \sin\kappa & 0 & \cos\kappa \end{bmatrix}, \tag{A.2}$$

where $\sin\kappa$ is the coupling between the two fields. For the propagation, only the relative phase shift between the two fields is of importance, hence it can be represented by the matrix

$$\mathcal{T} = \begin{bmatrix} 1 & 0 & 0 & 0 \\ 0 & 1 & 0 & 0 \\ 0 & 0 & \cos\phi & -\sin\phi \\ 0 & 0 & \sin\phi & \cos\phi \end{bmatrix}, \tag{A.3}$$

where ϕ is the relative phase shift. Assuming we are squeezing the readout quadrature, the noise is proportional to the element $\mathcal{M}(2,2)$, where

$$\begin{aligned} \mathcal{M} &= \mathcal{K}^{-1}\mathcal{T}\mathcal{K}\mathcal{S}\big(\mathcal{K}^{-1}\mathcal{T}\mathcal{K}\mathcal{S}\big)^{\mathrm{T}} \\ &= \mathcal{K}^{-1}\mathcal{T}\mathcal{K}\mathcal{S}^2\mathcal{K}^{-1}\mathcal{T}^{\mathrm{T}}\mathcal{K}. \end{aligned} \tag{A.4}$$

Assuming the coupling magnitude $\sin\kappa$ is small, then

$$\mathcal{M}(2,2) = \mathrm{e}^{-2r} - 2\kappa^2\mathrm{e}^{-2r}\big(\mathrm{e}^{2r}-1\big)\big(\cos\phi - 1\big) + \mathcal{O}(\kappa^3). \tag{A.5}$$

Thus, the worst case scenario is if the propagation gives rise to a relative phase shift between the two fields of $\phi = \pi$, in which case the noise arising due to the coherent

scattering effect scales as

$$\mathrm{e}^{-2r} + 4\kappa^2\left(1 - \mathrm{e}^{-2r}\right) + \mathcal{O}(\kappa^3). \tag{A.6}$$

For large squeeze magnitudes, this is a factor of two worse than if these two scattering points would have been exchanged for two optics with small losses κ.

APPENDIX B

FIELD PROPAGATION

This appendix derives how a Hermite-Gaussian-shaped field component with frequency ω propagates in a gravitational wave detector and its optical subsystems. The Hermite-Gaussian mode is assumed to be an eigenmode of the cavities of this system, thus, the optical cavities are assumed to be spatially mode matched.

B.1 Fabry-Perot cavity

A Fabry-Perot cavity is a linear optical resonator that consists of two mirrors separated by some distance, as seen in figure B.1. Here, the distance is split into two parts: the macroscopical length L, which is an integer multiple of the reference wavelength λ_0, and the microscopical lengths δL_1 and δL_2, which are associated with the mirror positions. In the convention used in this work, a field transmitted through a thin mirror is phase shifted by $\pi/2$ and the reflected field is not phase shifted at all. Assuming that there is only one incoming field, here called a_0, the field components are related to each other

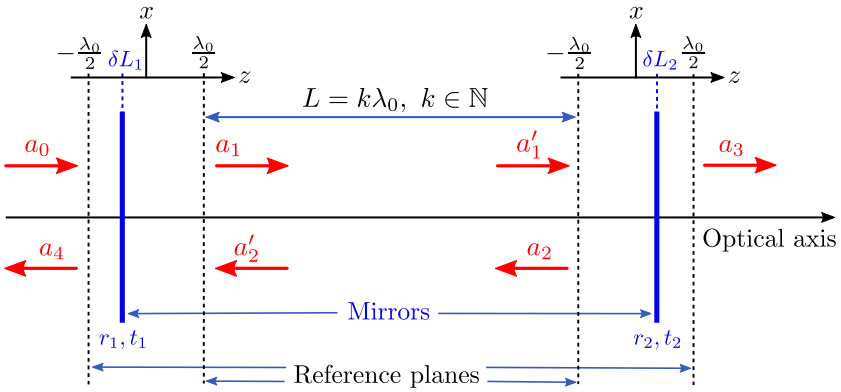

Figure B.1: The figure shows a model of a Fabry-Perot cavity in vacuum, and its field components. The distance between the two thin mirrors have contributions from the exact mirror positions δL_1 and δL_2 and the macroscopical length L, which is an integer multiple of the reference wavelength λ_0.

as

$$
\begin{aligned}
a_1 &= it_1 a_0 + r_1 \mathrm{e}^{i\frac{2\delta L_1 \omega_0}{c}} a_2' \\
a_1' &= \mathrm{e}^{-i\left(\frac{\Omega L}{c} - (m+n)\psi_L\right)} a_1 \\
a_2 &= r_2 \mathrm{e}^{-i\frac{2\delta L_2 \omega_0}{c}} a_1' \\
a_2' &= \mathrm{e}^{-i\left(\frac{\Omega L}{c} - (m+n)\psi_L\right)} a_2 \\
a_3 &= it_2 a_1' \\
a_4 &= r_1 \mathrm{e}^{-i\frac{2\delta L_1 \omega_0}{c}} a_0 + it_1 a_2',
\end{aligned}
\tag{B.1}
$$

where t_k and r_k are the amplitude transmission and reflection coefficients of the mirrors, L is the macroscopic length of the cavity, $\omega = \omega_0 + \Omega$, m and n labels the Hermite-Gaussian mode, and ψ_L is the half-trip Gouy-phase. From these equations, it follows that the circulating, transmitted and reflected transfer functions are given by

$$
\begin{aligned}
\frac{a_1}{a_0} &= \frac{it_1}{1 - r_1 r_2 \mathrm{e}^{-2i\left(\phi + \frac{\Omega L}{c} - (m+n)\psi_L\right)}}, \\
\frac{a_3}{a_0} &= \frac{-t_1 t_2 \mathrm{e}^{-i\left(\frac{\Omega L}{c} - (m+n)\psi_L\right)}}{1 - r_1 r_2 \mathrm{e}^{-2i\left(\phi + \frac{\Omega L}{c} - (m+n)\psi_L\right)}}, \text{ and} \\
\frac{a_4}{a_0} &= \frac{r_1 - r_2(t_1^2 + r_1^2)\mathrm{e}^{-2i\left(\phi + \frac{\Omega L}{c} - (m+n)\psi_L\right)}}{1 - r_1 r_2 \mathrm{e}^{-2i\left(\phi + \frac{\Omega L}{c} - (m+n)\psi_L\right)}} \mathrm{e}^{-2i\phi_1},
\end{aligned}
\tag{B.2}
$$

respectively. Here, $\phi_1 = \frac{\omega_0 \delta L_1}{c}$, $\phi_2 = \frac{\omega_0 \delta L_2}{c}$, $\delta L = \delta L_2 - \delta L_1$, and $\phi = \phi_2 - \phi_1$.

B.2 Michelson interferometer

The Michelson interferometer consists of a beam splitter and two mirrors, one in the end of each beam splitter path, as seen in figure B.2. The macroscopic path lengths

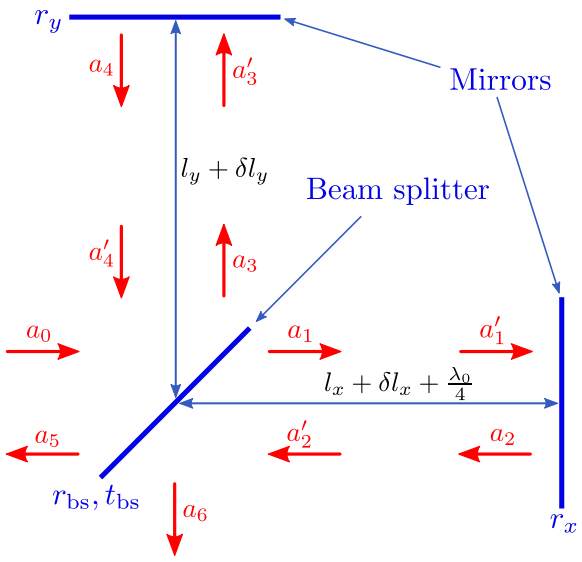

Figure B.2: The figure shows a Michelson interferometer and the field components used in equation B.3.

are called l_x and l_y, and the microscopic lengths associated with the mirror positions are called δl_x and δl_y. The x-path has been given an offset of $\lambda_0/4$ such that $a_6 = 0$ if $\Omega = 0$ and $\delta l_x = \delta l_y$. Assuming that the beam splitter perfectly splits the field in two

parts, i.e., $r_{\rm bs} = t_{\rm bs} = \frac{1}{\sqrt{2}}$, then the fields components seen in figure B.2 are related as:

$$
\begin{aligned}
a_1 &= \frac{i}{\sqrt{2}} a_0 \\
a_1' &= -i \mathrm{e}^{-i\left(\frac{\omega_0 \delta l_x}{c} + \frac{\Omega l_x}{c} - (m+n)\psi_{l_x}\right)} a_1 \\
a_2 &= r_x a_1' \\
a_2' &= -i \mathrm{e}^{-i\left(\frac{\omega_0 \delta l_x}{c} + \frac{\Omega l_x}{c} - (m+n)\psi_{l_x}\right)} a_2 \\
a_3 &= \frac{1}{\sqrt{2}} a_0 \\
a_3' &= \mathrm{e}^{-i\left(\frac{\omega_0 \delta l_y}{c} + \frac{\Omega l_y}{c} - (m+n)\psi_{l_y}\right)} a_3 \\
a_4 &= r_y a_3' \\
a_4' &= \mathrm{e}^{-i\left(\frac{\omega_0 \delta l_y}{c} + \frac{\Omega l_y}{c} - (m+n)\psi_{l_y}\right)} a_4 \\
a_5 &= \frac{i}{\sqrt{2}} a_2' + \frac{1}{\sqrt{2}} a_4' \\
a_6 &= \frac{1}{\sqrt{2}} a_2' + \frac{i}{\sqrt{2}} a_4',
\end{aligned}
\tag{B.3}
$$

where ψ_x and ψ_x are the Gouy-phases picked up when propagating the paths between the beam splitter and the mirrors X and Y, respectively. Hence, the reflection and transmission transfer functions for the Michelson interferometer becomes

$$
\begin{aligned}
\frac{a_5}{a_0} &= \frac{1}{2} \mathrm{e}^{-i\left(\phi_M + \frac{\Omega l_M}{c} - (m+n)\psi_M\right)} \left(r_y \mathrm{e}^{i\left(\Delta\phi_M + \frac{\Omega \Delta l_M}{c} - (m+n)\Delta\psi_M\right)} + r_x \mathrm{e}^{-i\left(\Delta\phi_M + \frac{\Omega \Delta l_M}{c} - (m+n)\Delta\psi_M\right)} \right), \\
\frac{a_6}{a_0} &= \frac{i}{2} \mathrm{e}^{-i\left(\phi_M + \frac{\Omega l_M}{c} - (m+n)\psi_M\right)} \left(r_y \mathrm{e}^{i\left(\Delta\phi_M + \frac{\Omega \Delta l_M}{c} - (m+n)\Delta\psi_M\right)} - r_x \mathrm{e}^{-i\left(\Delta\phi_M + \frac{\Omega \Delta l_M}{c} - (m+n)\Delta\psi_M\right)} \right),
\end{aligned}
\tag{B.4}
$$

where $\phi_M = \phi_{l_x} + \phi_{l_y}$, $\Delta\phi_M = \phi_{l_x} - \phi_{l_y}$, $\phi_{l_{x/y}} = \frac{\omega_0 \delta l_{x/y}}{c}$, $l_M = l_x + l_y$, $\Delta l_M = l_x - l_y$, $\psi_M = \psi_{l_x} + \psi_{l_y}$, and $\Delta\psi_M = \psi_{l_x} - \psi_{l_y}$. Thus, the sum of the phases picked up in the two different paths only contribute to the overall phase of the reflected and transmitted fields, while the differential phase shifts completely determine how much power that is transmitted and reflected.

B.3 Power recycled Michelson interferometer with arm cavities

A power recycled Michelson interferometer is obtained by combining the Michelson interferometer and two FP-cavities, and adding a power recycling mirror in front of the beam splitter, as seen in figure B.3. Since the the fields in the Michelson and the FP-

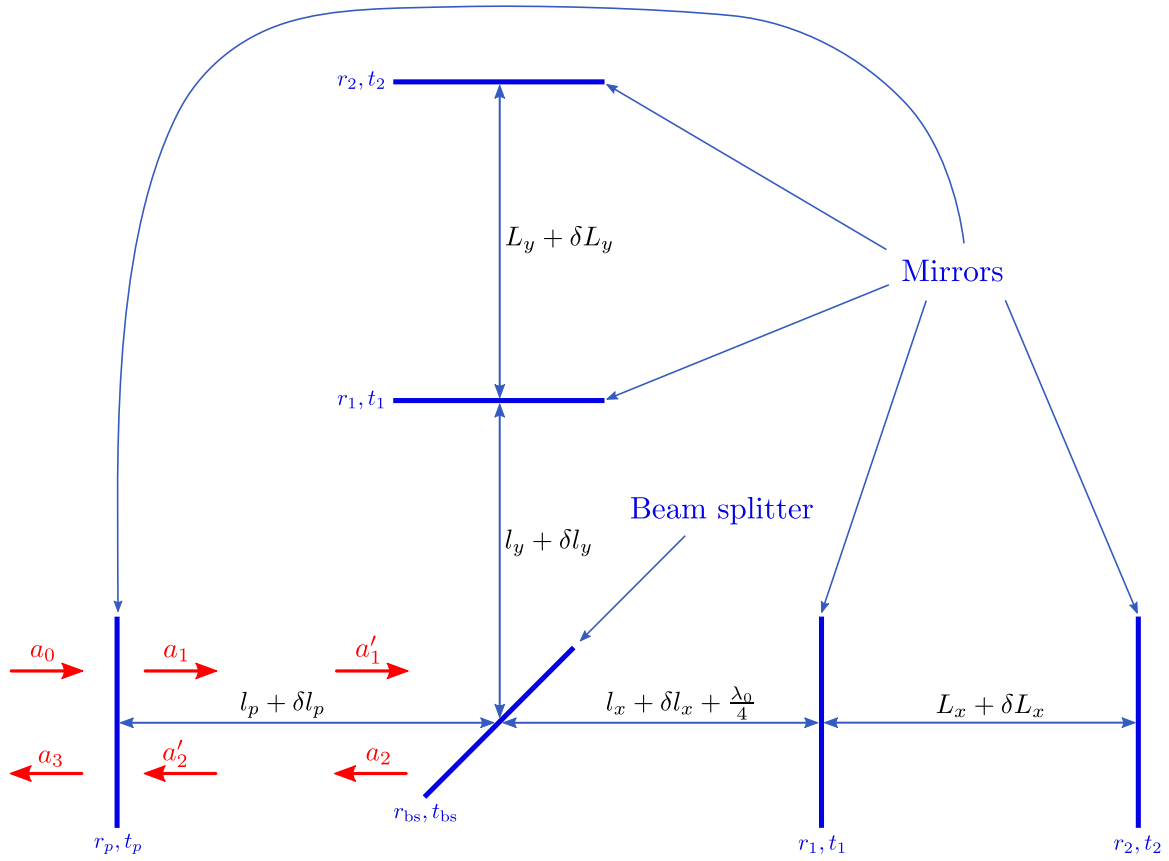

Figure B.3: The figure shows a power recycled Michelson interferometer with Fabry-Perot arm cavities, and the field components in the power recycling cavity that used in equation B.5.

cavities already have been derived, only the fields of the PRC are explicitly considered

here. The fields of the PRC are given by

$$\begin{aligned}
a_1 &= it_p a_0 + r_p a_2' \\
a_1' &= \mathrm{e}^{-i\left(\frac{\omega_0 \delta l_p}{c} + \frac{\Omega l_p}{c} - (m+n)\psi_{l_p}\right)} a_1 \\
a_2 &= r_M a_1' \\
a_2' &= \mathrm{e}^{-i\left(\frac{\omega_0 \delta l_p}{c} + \frac{\Omega l_p}{c} - (m+n)\psi_{l_p}\right)} a_2 \\
a_3 &= r_p a_0 + it_p a_2', \qquad \text{(B.5)}
\end{aligned}$$

where the reflection coefficients for the Michelson and the arm cavities are obtained from equations B.4 and B.2, and becomes

$$\begin{aligned}
r_M &= \frac{1}{2}\mathrm{e}^{-i\left(\phi_M + \frac{\Omega l_M}{c} - (m+n)\psi_M\right)}\left(r_y \mathrm{e}^{i\left(\Delta\phi_M + \frac{\Omega \Delta l_M}{c} - (m+n)\Delta\psi_M\right)} + r_x \mathrm{e}^{-i\left(\Delta\phi_M + \frac{\Omega \Delta l_M}{c} - (m+n)\Delta\psi_M\right)}\right) \\
r_x &= \frac{r_1 - r_2(t_1^2 + r_1^2)\mathrm{e}^{-2i\left(\phi_X + \frac{\Omega L}{c} - (m+n)\psi_L\right)}}{1 - r_1 r_2 \mathrm{e}^{-2i\left(\phi_X + \frac{\Omega L}{c} - (m+n)\psi_L\right)}} \\
r_y &= \frac{r_1 - r_2(t_1^2 + r_1^2)\mathrm{e}^{-2i\left(\phi_Y + \frac{\Omega L}{c} - (m+n)\psi_L\right)}}{1 - r_1 r_2 \mathrm{e}^{-2i\left(\phi_Y + \frac{\Omega L}{c} - (m+n)\psi_L\right)}}. \qquad \text{(B.6)}
\end{aligned}$$

The reflection coefficient for the PRC is given by

$$\frac{a_3}{a_0} = \frac{2r_p - (r_p^2 + t_p^2)\left(r_y \mathrm{e}^{i\Delta\varphi_M} + r_x \mathrm{e}^{-i\Delta\varphi_M}\right)\mathrm{e}^{-2i\varphi_{\mathrm{prc}}}}{2 - r_p \mathrm{e}^{-2i\varphi_{\mathrm{prc}}}\left(r_y \mathrm{e}^{i\Delta\varphi_M} + r_x \mathrm{e}^{-i\Delta\varphi_M}\right)}, \qquad \text{(B.7)}$$

where

$$\begin{aligned}
\varphi_{\mathrm{prc}} &= \phi_{\mathrm{prc}} + \frac{\Omega l_{\mathrm{prc}}}{c} - (m+n)\psi_{l_{\mathrm{prc}}} \\
\Delta\varphi_M &= \Delta\phi_M + \frac{\Omega \Delta l_M}{c} - (m+n)\Delta\psi_M \\
\phi_{\mathrm{prc}} &= \frac{\omega_0\left(\delta l_p + (\delta l_x + \delta l_y)/2\right)}{c} \\
l_{\mathrm{prc}} &= l_p + \frac{l_x + l_y}{2} \\
\psi_{\mathrm{prc}} &= \psi_{l_p} + \frac{\psi_{l_x} + \psi_{l_y}}{2}. \qquad \text{(B.8)}
\end{aligned}$$

APPENDIX C

ANGULAR DEGREES OF FREEDOM: LIGO AND FINESSE DEFINITIONS

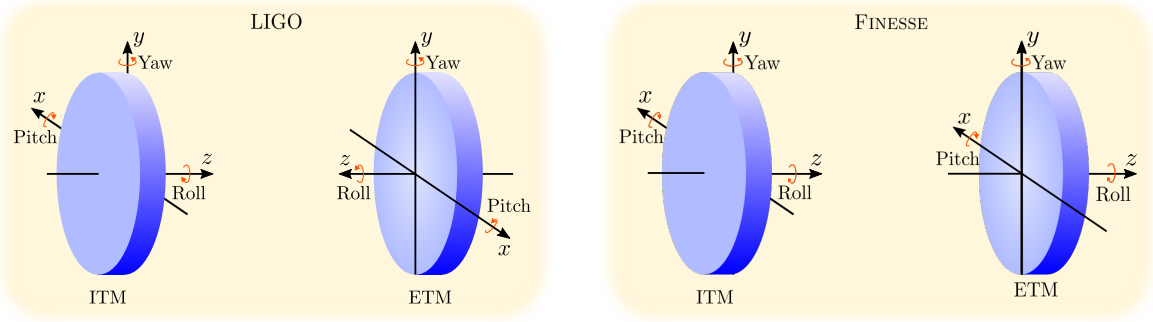

Figure C.1: The figure shows the mirror angular degrees of freedom, as defined by LIGO (left) and FINESSE (right).

To define the angular degrees of freedom, LIGO uses a local coordinate system for each mirror, defined by three orthogonal unit vectors:

$\hat{\mathbf{z}}$ = normal to the HR-surface at the intersection with the optical axis, pointing towards the center of curvature,

$\hat{\mathbf{y}}$ = vertical and oriented upwards, and

$$\hat{\mathbf{x}} = \hat{\mathbf{y}} \times \hat{\mathbf{z}}. \tag{C.1}$$

This LIGO convention is in the left hand side of figure C.1. FINESSE also defines $\hat{\mathbf{x}}$

and $\hat{\mathbf{y}}$ as above, but $\hat{\mathbf{z}}$ is instead defined as pointing from node 1 to node 2 for a mirror component and from node 1 to node 3 for a beam splitter. Following the FINESSE convention of placing the components such that node 1 is closest to the main laser along the optical axis, the coordinate systems for the two mirrors in an arm cavity are as shown on the right hand side of figure C.1.

Thus, if the basis sets for the ITM and the ETM in the LIGO convention are $\{\hat{\mathbf{x}}_1, \hat{\mathbf{y}}_1, \hat{\mathbf{z}}_1\}$ and $\{\hat{\mathbf{x}}_2, \hat{\mathbf{y}}_2, \hat{\mathbf{z}}_2\}$, then

$$\begin{aligned} \hat{\mathbf{x}}_1 &= -\hat{\mathbf{x}}_2 \\ \hat{\mathbf{y}}_1 &= \hat{\mathbf{y}}_2 \\ \hat{\mathbf{z}}_1 &= -\hat{\mathbf{z}}_2, \end{aligned} \tag{C.2}$$

where $\{\hat{\mathbf{x}}_1, \hat{\mathbf{y}}_1, \hat{\mathbf{z}}_1\}$ also is the basis set for both mirrors in the FINESSE convention. If θ^{F} denotes a pitch rotation in the FINESSE convention and θ^{L} denotes the equivalent angle in the LIGO convention, then a rotation about the radiation pressure eigenmodes can be defined as

$$\begin{aligned} \begin{bmatrix} \theta_{\mathrm{S}} \\ \theta_{\mathrm{H}} \end{bmatrix} &= \frac{1}{r^2+1} \begin{bmatrix} 1 & r \\ r & -1 \end{bmatrix} \begin{bmatrix} \theta^{\mathrm{L}}_{\mathrm{ETM}} \\ \theta^{\mathrm{L}}_{\mathrm{ITM}} \end{bmatrix} \\ &= \frac{1}{r^2+1} \begin{bmatrix} -1 & r \\ -r & -1 \end{bmatrix} \begin{bmatrix} \theta^{\mathrm{F}}_{\mathrm{ETM}} \\ \theta^{\mathrm{F}}_{\mathrm{ITM}} \end{bmatrix}, \end{aligned} \tag{C.3}$$

where

$$r = \frac{1}{2}\left(g_{\mathrm{ETM}} - g_{\mathrm{ITM}} + \sqrt{\left(g_{\mathrm{ETM}} - g_{\mathrm{ITM}}\right)^2 + 4} \right). \tag{C.4}$$

The transformation back to the mirror basis is given by

$$\begin{bmatrix} \theta^{\mathrm{F}}_{\mathrm{ETM}} \\ \theta^{\mathrm{F}}_{\mathrm{ITM}} \end{bmatrix} = \begin{bmatrix} -\theta^{\mathrm{L}}_{\mathrm{ETM}} \\ \theta^{\mathrm{L}}_{\mathrm{ITM}} \end{bmatrix} = \begin{bmatrix} -1 & -r \\ r & -1 \end{bmatrix} \begin{bmatrix} \theta_{\mathrm{S}} \\ \theta_{\mathrm{H}} \end{bmatrix},$$

which is used in the PyKat tools. For the yaw degrees of freedom, the FINESSE and LIGO conventions agree as both have the y-axis pointing vertically upwards. The transformations to the eigenmode coordinates θ_S and θ_H are given by

$$\begin{aligned} \begin{bmatrix} \theta_{\mathrm{S}} \\ \theta_{\mathrm{H}} \end{bmatrix} &= \frac{1}{r^2+1} \begin{bmatrix} 1 & -r \\ r & 1 \end{bmatrix} \begin{bmatrix} \theta^{\mathrm{L}}_{\mathrm{ETM}} \\ \theta^{\mathrm{L}}_{\mathrm{ITM}} \end{bmatrix} \\ &= \frac{1}{r^2+1} \begin{bmatrix} 1 & -r \\ r & 1 \end{bmatrix} \begin{bmatrix} \theta^{\mathrm{F}}_{\mathrm{ETM}} \\ \theta^{\mathrm{F}}_{\mathrm{ITM}} \end{bmatrix}, \end{aligned} \tag{C.5}$$

The transformation back to the mirror basis is given by

$$\begin{bmatrix} \theta^{\mathrm{F}}_{\mathrm{ETM}} \\ \theta^{\mathrm{F}}_{\mathrm{ITM}} t \end{bmatrix} = \begin{bmatrix} \theta^{\mathrm{L}}_{\mathrm{ETM}} \\ \theta^{\mathrm{L}}_{\mathrm{ITM}} \end{bmatrix} = \begin{bmatrix} 1 & r \\ -r & 1 \end{bmatrix} \begin{bmatrix} \theta_{\mathrm{S}} \\ \theta_{\mathrm{H}} \end{bmatrix},$$

which is used in the PyKat tools.

APPENDIX D

MISALIGNMENT COUPLINGS

In this appendix the misalignment-induced coupling coefficients between the fundamental mode and higher-order spatial modes are derived. Each higher-order mode can be written as a product of the fundamental mode and a polynomial. The equations for the first three higher-order modes are given by:

$$
\begin{aligned}
u_0(x,z) &= \left(\frac{\sqrt{2}}{\sqrt{\pi}w(z)}\right)^{1/2} \mathrm{e}^{\frac{i}{2}\psi(z)} \mathrm{e}^{-\frac{x^2}{w^2(z)}} \mathrm{e}^{-i\frac{kx^2}{2R_c(z)}} \\
u_1(x,z) &= \left(\frac{\sqrt{2}}{\sqrt{\pi}w(z)}\right)^{1/2} \mathrm{e}^{\frac{3i}{2}\psi(z)} \frac{2x}{w(z)} \mathrm{e}^{-\frac{x^2}{w^2(z)}} \mathrm{e}^{-i\frac{kx^2}{2R_c(z)}} \\
&= \frac{2x}{w(z)} \mathrm{e}^{i\psi(z)} u_0(x,z) \\
u_2(x,z) &= \frac{1}{\sqrt{2}} \left(\frac{\sqrt{2}}{\sqrt{\pi}w(z)}\right)^{1/2} \mathrm{e}^{\frac{5i}{2}\psi(z)} \left(\frac{4x^2}{w^2(z)} - 1\right) \mathrm{e}^{-\frac{x^2}{w^2(z)}} \mathrm{e}^{-i\frac{kx^2}{2R_c(z)}} \\
&= \frac{1}{\sqrt{2}} \mathrm{e}^{2i\psi(z)} \left(\frac{4x^2}{w^2(z)} - 1\right) u_0(x,z) \\
u_3(x,z) &= \sqrt{\frac{2}{3}} \left(\frac{\sqrt{2}}{\sqrt{\pi}w(z)}\right)^{1/2} \mathrm{e}^{\frac{7i}{2}\psi(z)} \left(\frac{4x^3}{w^3(z)} - \frac{3x}{w(z)}\right) \mathrm{e}^{-\frac{x^2}{w^2(z)}} \mathrm{e}^{-i\frac{kx^2}{2R_c(z)}} \\
&= \sqrt{\frac{2}{3}} \mathrm{e}^{3i\psi(z)} \left(\frac{4x^3}{w^3(z)} - \frac{3x}{w(z)}\right) u_0(x,z),
\end{aligned}
\tag{D.1}
$$

where x is the transverse coordinate, z is the longitudinal coordinate, $w(z)$ is the beam radius, $R_c(z)$ is the radius of curvature of the wavefront, and $\psi(z)$ is the Gouy-phase. Any misalignment can be described by a combination of an offset and a tilt in the transverse plane, as seen in figure 4.1 in section 4.1, and the coupling coefficients for these two cases are derived below. It is assumed that the beam is in the fundamental mode u_0 in the coordinate system defined by the beam axis.

D.1 Transverse offset

If the coordinates of the coordinate systems defined by the optical axis and the beam axis are (x, z) and (x', z'), respectively, then the the transformation between the two systems is given by

$$\begin{aligned} x' &= x - \Delta x \\ z' &= z \end{aligned} \tag{D.2}$$

Assuming that the waist of the beam and the waist of the cavity eigenmode are located in the plane $z = z' = 0$, then $R_c(z' = 0) = R_c(z = 0) = \infty$ and $\psi(z' = 0) = \psi(z = 0) = 0$. Thus, the only contributions to higher-order modes couplings come from the factor $\mathrm{e}^{-x'^2/w_0^2}$. Taylor expansion of the incoming fundamental mode gives

$$\begin{aligned} u_0'(x', 0) &= u_0(x, 0)\left[1 - \frac{\Delta x^2}{w_0^2} + 2\left(\frac{\Delta x}{w_0} - \frac{\Delta x^3}{w_0^3}\right)\frac{x}{w_0} + 2\frac{\Delta x^2}{w_0^2}\frac{x^2}{w_0^2} + \frac{4}{3}\frac{\Delta x^3}{w_0^3}\frac{x^3}{w_0^3} + \mathcal{O}\left(\frac{\Delta x^4}{w_0^4}\right)\right] \\ &= \left(1 - \frac{1}{2}\frac{\Delta x^2}{w_0^2}\right)u_0(x, 0) + \left(\frac{\Delta x}{w_0} - \frac{1}{2}\frac{\Delta x^3}{w_0^3}\right)u_1(x, 0) + \frac{1}{\sqrt{2}}\frac{\Delta x^2}{w_0^2}u_2(x, 0) \\ &\quad + \frac{1}{\sqrt{6}}\frac{\Delta x^3}{w_0^3}u_3(x, 0) + \mathcal{O}\left(\frac{\Delta x^4}{w_0^4}\right), \end{aligned} \tag{D.3}$$

where equation D.1 has been used to obtain the last equality.

D.2 Tilted beam

For a beam tiled by an angle β with respect to the optical axis, the transformation of the coordinates is given by

$$\begin{aligned} x' &= x\cos\beta - z\sin\beta \\ z' &= x\sin\beta + z\cos\beta, \end{aligned} \tag{D.4}$$

where z can be expressed as

$$z = z_R\sqrt{\frac{w^2(z)}{w_0^2} - 1}. \tag{D.5}$$

Here, we perform the basis change at the waist of the eigenmode, i.e., in the plane defined by $z = 0$, which means that $x' = x\cos\beta$ and $z' = x\sin\beta$. Thus, the magnitude of the incoming mode can be expanded in β as

$$\begin{aligned} \left(\frac{\sqrt{2}}{\sqrt{\pi}w(z')}\right)^{1/2} \mathrm{e}^{-\frac{x'^2}{w^2(z')}} &= \left(\frac{\sqrt{2}}{\sqrt{\pi}w(z)}\right)^{1/2} \mathrm{e}^{-\frac{x^2}{w^2(z)}}\left[1 + \left(\beta^2 - \frac{\beta^2\theta_D^2}{4}\right)\frac{x^2}{w_0^2} + \beta^2\theta_D^2\frac{x^4}{w_0^4} + \mathcal{O}(\beta^4)\right] \\ &= \left(\frac{\sqrt{2}}{\sqrt{\pi}w(z)}\right)^{1/2} \mathrm{e}^{-\frac{x^2}{w^2(z)}}\left[1 + \beta^2\frac{x^2}{w_0^2} + \mathcal{O}(\beta^2\theta_D^2)\right] \\ &= \left(\frac{\sqrt{2}}{\sqrt{\pi}w(z)}\right)^{1/2} \mathrm{e}^{-\frac{x^2}{w^2(z)}} + \mathcal{O}(\beta^2), \end{aligned} \tag{D.6}$$

where $\theta_D = \tan^{-1}(w_0/z_R) \approx w_0/z_R$ is the diffraction angle, and it is assumed throughout this section that $\beta < \theta_D \ll 1$. The phase factor due to the Gouy-phase can be expanded in β as

$$\begin{aligned} \mathrm{e}^{\frac{i\psi(z')}{2}} &= 1 + i\Big(\frac{\beta\theta_D}{2} - \frac{\beta^3\theta_D}{12}\Big)\frac{x}{w_0} - \frac{\beta^2\theta_D^2}{8}\frac{x^2}{w_0^2} - i\frac{3\beta^3\theta_D^3}{16}\frac{x^3}{w_0^3} + \mathcal{O}\big(\beta^4\theta_D^2\big) \\ &= 1 + \mathcal{O}(\beta\theta_D). \end{aligned} \tag{D.7}$$

Similarly, the curvature of the phase-front can be expanded as

$$\begin{aligned} \mathrm{e}^{\frac{-ikx'^2}{2R_c(z')}} &= 1 - i\Big(\beta\theta_D - \frac{7\beta^3\theta_D}{6}\Big)\frac{x^3}{w_0^3} - \frac{\beta^2\theta_D^2}{2}\frac{x^6}{w_0^6} + \mathcal{O}(\beta^3\theta_D^3) \\ &= 1 + \mathcal{O}(\beta\theta_D) \end{aligned} \tag{D.8}$$

Thus, the contribution to couplings to higher-order modes from these two phase factors can be omitted as long as the paraxial approximation holds ($\theta_D \ll 1$). The expansion of the phase due to propagation is given by

$$\mathrm{e}^{-ikz'} = 1 - 2i\frac{\beta}{\theta_D}\frac{x}{w_0} - 2\frac{\beta^2}{\theta_D^2}\frac{x^2}{w_0^2} + i\frac{4}{3}\frac{\beta^3}{\theta_D^3}\frac{x^3}{w_0^3} + \mathcal{O}\left(\frac{\beta^4}{\theta_D^4}\right), \tag{D.9}$$

thus, from here one obtains non-vanishing couplings to higher-order modes. By using equations D.1, D.6, D.7, D.8 and D.9, the incoming beam can be described by

$$\begin{aligned} u_0'(x',z') =& \left(1 - \frac{1}{2}\frac{\beta^2}{\theta_D^2}\right)u_0(x,0) - i\left(\frac{\beta}{\theta_D} - \frac{1}{2}\frac{\beta^3}{\theta_D^3}\right)u_1(x,0) - \frac{1}{\sqrt{2}}\frac{\beta^2}{\theta_D^2}u_2(x,0) + \\ & i\frac{1}{\sqrt{6}}\frac{\beta^3}{\theta_D^3}u_3(x,0) + \mathcal{O}\left(\frac{\beta^4}{\theta_D^4}\right). \end{aligned} \tag{D.10}$$

BIBLIOGRAPHY

1. Abbott, B. P. *et al.* Observation of Gravitational Waves from a Binary Black Hole Merger. *Phys. Rev. Lett.* **116,** 061102 (2016).

2. Abbott, B. P. *et al.* GW151226: Observation of Gravitational Waves from a 22-Solar-Mass Binary Black Hole Coalescence. *Phys. Rev. Lett.* **116,** 241103 (2016).

3. Abbott, B. P. *et al.* GW170104: Observation of a 50-Solar-Mass Binary Black Hole Coalescence at Redshift 0.2. *Phys. Rev. Lett.* **118,** 221101 (2017).

4. Abbott, B. P. *et al.* GW170608: Observation of a 19 Solar-mass Binary Black Hole Coalescence. *The Astrophysical Journal Letters* **851,** L35 (2017).

5. Abbott, B. P. *et al.* GW170814: A Three-Detector Observation of Gravitational Waves from a Binary Black Hole Coalescence. *Phys. Rev. Lett.* **119,** 141101 (2017).

6. Abbott, B. P. *et al.* GW170817: Observation of Gravitational Waves from a Binary Neutron Star Inspiral. *Phys. Rev. Lett.* **119,** 161101 (2017).

7. Abbott, B. P. *et al.* Multi-messenger Observations of a Binary Neutron Star Merger. *The Astrophysical Journal Letters* **848,** L12 (2017).

8. Goldstein, A. *et al.* An Ordinary Short Gamma-Ray Burst with Extraordinary Implications: Fermi -GBM Detection of GRB 170817A. *The Astrophysical Journal Letters* **848,** L14 (2017).

9. Savchenko, V. *et al.* INTEGRAL Detection of the First Prompt Gamma-Ray Signal Coincident with the Gravitational-wave Event GW170817. *The Astrophysical Journal Letters* **848,** L15 (2017).

10. Markakis, C. *et al.* Neutron star equation of state via gravitational wave observations. *Journal of Physics: Conference Series* **189,** 012024 (2009).

11. Annala, E., Gorda, T., Kurkela, A. & Vuorinen, A. Gravitational-Wave Constraints on the Neutron-Star-Matter Equation of State. *Phys. Rev. Lett.* **120,** 172703 (17 Apr. 2018).

12. Abbott, B. P. *et al.* Gravitational Waves and Gamma-Rays from a Binary Neutron Star Merger: GW170817 and GRB 170817A. *The Astrophysical Journal Letters* **848,** L13 (2017).

13. Abbott, B. P. *et al.* Tests of General Relativity with GW150914. *Phys. Rev. Lett.* **116,** 221101 (22 2016).

14. Abbott, B. P. *et al.* A gravitational-wave standard siren measurement of the Hubble constant. *Nature* **551,** 85 (2017).

15. Einstein, A. Näherungsweise Integration der Feldgleichungen der Gravitation. *Sitzungsberichte der Königlich Preußischen Akademie der Wissenschaften* **1,** 688 (1916).

16. Sathyaprakash, B. S. & Schutz, B. F. Physics, Astrophysics and Cosmology with Gravitational Waves. *Living Reviews in Relativity* **12,** 1 (2009).

17. Aasi, J. *et al.* Advanced LIGO. *Classical and Quantum Gravity* **32,** 074001 (2015).

18. Acernese, F. *et al.* Advanced Virgo: a second-generation interferometric gravitational wave detector. *Classical and Quantum Gravity* **32,** 024001 (2015).

19. Lück, H. *et al.* Status of the GEO600 detector. *Classical and Quantum Gravity* **23,** S71 (2006).

20. Akutsu, T. *et al.* Construction of KAGRA: an underground gravitational-wave observatory. *Progress of Theoretical and Experimental Physics* **2018,** 013F01 (2018).

21. Hild, S. *et al.* DC-readout of a signal-recycled gravitational wave detector. *Classical and Quantum Gravity* **26,** 055012 (2009).

22. Fricke, T. T. *et al.* DC readout experiment in Enhanced LIGO. *Classical and Quantum Gravity* **29,** 065005 (2012).

23. Smith-Lefebvre, N. M. *Techniques for Improving the Readout Sensitivity of Gravitational Wave Antennae* PhD thesis (Massachusetts institute of technology, 2012).

24. Kogelnik, H. Matching of Optical Modes. *The Bell System Technical Journal* **43,** 334 (1964).

25. Kogelnik, H. Imaging of Optical Modes — Resonators with Internal Lenses. *The Bell System Technical Journal* **44,** 455 (1965).

26. Kogelnik, H. & Li, T. Laser Beams and Resonators. *Applied optics* **5,** 1550 (1966).

27. Bond, C., Brown, D., Freise, A. & Strain, K. A. Interferometer techniques for gravitational-wave detection. *Living Reviews in Relativity* **19,** 3 (17, 2017).

28. Caves, C. M. & Schumaker, B. L. New formalism for two-photon quantum optics. I - Quadrature phases and squeezed states. *Physical Review A* **31,** 3068 (1985).

29. Schumaker, B. L. & Caves, C. M. New formalism for two-photon quantum optics. II. Mathematical foundation and compact notation. *Phys. Rev. A* **31,** 3093 (1985).

30. Kimble, H. J., Levin, Y., Matsko, A. B., Thorne, K. S. & Vyatchanin, S. P. Conversion of conventional gravitational-wave interferometers into quantum nondemolition interferometers by modifying their input and/or output optics. *Physical Review D* **65,** 022002–+ (2001).

31. Blow, K. J., Loudon, R. & Phoenix, S. J. D. Continuum fields in quantum optics. *Physical Review A* **42,** 4102 (1990).

32. Freise, A. *et al.* Frequency-domain interferometer simulation with higher-order spatial modes. *Classical and Quantum Gravity* **21.** Finesse is available at `http://www.gwoptics.org/finesse`., S1067 (2004).

33. Freise, A., Brown, D. & Bond, C. *FINESSE 2.0 User manual* University of Birmingham (2014). <`http://arxiv.org/abs/1306.2973`>.

34. Brown, D. & Freise, A. PYKAT*, Python interface and tools for Finesse* `http://www.gwoptics.org/pykat/`. Accessed: 2018-08-17. <`http://www.gwoptics.org/pykat/`>.

35. Töyrä, D. *et al.* Multi-spatial-mode effects in squeezed-light-enhanced interferometric gravitational wave detectors. *Physical Review D* **96,** 022006 (2017).

36. Caves, C. M. Quantum-mechanical noise in an Interferometer. *Physical Review D* **23,** 1693 (1981).

37. Unruh, W. G. in (eds P. Meystre, P. & Scully, M. O.) 647 (Plenum Press, New York, 1983).

38. Harms, J. *et al.* Squeezed-input, optical-spring, signal-recycled gravitational-wave detectors. *Physical Review D* **68,** 042001 (2003).

39. Chelkowski, S. *et al.* Experimental characterization of frequency-dependent squeezed light. *Physical Review A* **71,** 013806 (2005).

40. Evans, M., Barsotti, L., Kwee, P., Harms, J. & Miao, H. Realistic filter cavities for advanced gravitational wave detectors. *Phys. Rev. D* **88,** 022002 (2 2013).

41. Kwee, P., Miller, J., Isogai, T., Barsotti, L. & Evans, M. Decoherence and degradation of squeezed states in quantum filter cavities. *Phys. Rev. D* **90,** 062006 (2014).

42. Yonezawa, H. *et al.* Quantum-Enhanced Optical-Phase Tracking. *Science* **337,** 1514–1517. ISSN: 0036-8075 (2012).

43. Dwyer, S. *et al.* Squeezed quadrature fluctuations in a gravitational wave detector using squeezed light. *Opt. Express* **21,** 19047–19060 (Aug. 2013).

44. Kolobov, M. & Sokolov, I. Squeezed states of light and noise-free optical images. *Physics Letters A* **140,** 101–104. ISSN: 0375-9601 (1989).

45. Lugiato, L. A. & Gatti, A. Spatial structure of a squeezed vacuum. *Phys. Rev. Lett.* **70,** 3868–3871 (25 June 1993).

46. Lugiato, L. A., Gatti, A. & Brambilla, E. Quantum imaging. *Journal of Optics B: Quantum and Semiclassical Optics* **4,** S176 (2002).

47. Lassen, M. *et al.* Generation of squeezing in higher order Hermite-Gaussian modes with an optical parametric amplifier. *Journal of the European Optical Society - Rapid publications* **1,** 06003 (2006).

48. Morizur, J.-F., Armstrong, S., Treps, N., Janousek, J. & Bachor, H.-A. Spatial reshaping of a squeezed state of light. *The European Physical Journal D* **61,** 237–239. ISSN: 1434-6079 (2011).

49. Semmler, M. *et al.* Single-mode squeezing in arbitrary spatial modes. *Opt. Express* **24,** 7633–7642 (Apr. 2016).

50. Treps, N. *et al.* A Quantum Laser Pointer. *Science* **301,** 940–943. ISSN: 0036-8075 (2003).

51. Brown, D. D. *Interaction of light and mirrors: Advanced techniques for modelling future gravitational wave detectors* PhD thesis (University of Birmingham, 2015). <http://etheses.bham.ac.uk/6500/9/BrownD16PhD_Final.pdf>.

52. Harms, J., Cochrane, P. & Freise, A. Quantum-noise power spectrum of fields with discrete classical components. *Physical Review A* **76,** 023803 (2007).

53. Zhang, T. *et al.* Effects of static and dynamic higher-order optical modes in balanced homodyne readout for future gravitational waves detectors. *Phys. Rev. D* **95,** 062001 (6 Mar. 2017).

54. Corbitt, T., Chen, Y. & Mavalvala, N. Mathematical framework for simulation of quantum fields in complex interferometers using the two-photon formalism. *Physical Review A* **72,** 013818 (2005).

55. Khalili, F. Y. Quantum variational measurement in the next generation gravitational-wave detectors. *Phys. Rev. D* **76,** 102002 (10 Nov. 2007).

56. Khalili, F. Y. Optimal configurations of filter cavity in future gravitational-wave detectors. *Physical Review D* **81,** 122002 (2010).

57. Punturo, M. *et al.* The Einstein Telescope: a third-generation gravitational wave observatory. *Classical and Quantum Gravity* **27,** 194002 (2010).

58. Steinlechner, S., Korobko, M., Schnabel, R., Töyrä, D. & Freise, A. Mitigating mode-matching loss with squeezed higher-order modes. *To be submitted.* <https://dcc.ligo.org/LIGO-G1801607> (2018).

59. Accadia, T. *et al. Advanced Virgo Technical Design Report* tech. rep. (2012). <https://tds.ego-gw.it/?content=3&r=9317>.

60. Acernese, F. *et al.* Lock acquisition of the Virgo gravitational wave detector. *Astroparticle Physics* **30,** 29 (2008).

61. Drever, R. W. *et al.* Laser phase and frequency stabilization using an optical resonator. *Applied Physics B* **31,** 97 (1983).

62. Izumi, K. & Sigg, D. Advanced LIGO: length sensing and control in a dual recycled interferometric gravitational wave antenna. *Classical and Quantum Gravity* **34,** 015001 (2017).

63. Aso, Y. *et al.* Interferometer design of the KAGRA gravitational wave detector. *Phys. Rev. D* **88,** 043007 (4 2013).

64. Bertolotti, M. Matrix representation of geometrical properties of laser cavities. *Il Nuovo Cimento (1955-1965)* **32,** 1242 (1964).

65. Herriot, D., Kogelnik, H. & Kompfner, R. Off-Axis Paths in Spherical Mirror Interferometers. *Applied optics* **3,** 523 (1964).

66. Arai, K. *On the accumulated round-trip Gouy phase shift for a general optical cavity* tech. rep. T1300189-v1 (LIGO Scientific Collaboration, 2013). <https://dcc.ligo.org/LIGO-T1300189/public>.

67. Wang, H. *Beware of warped surfaces: near-unstable cavities for future gravitational wave detectors* PhD thesis (University of Birmingham, 2017). <http://etheses.bham.ac.uk/7874/5/Wang_Haoyu17PhD.pdf>.

68. Carter, W. H. Spot size and divergence for Hermite Gaussian beams of any order. *Applied Optics* **19,** 1027 (1980).

69. Luxon, J. T. & Parker, D. E. Higher-order CO2 laser beam spot size and depth of focus determined. *Applied Optics* **20,** 1933 (1981).

70. Hausdorff, F. *Grundzüge der Mengenlehre* <https://openlibrary.org/books/OL25477375M/Grundz%C3%83%C2%BCge_der_Mengenlehre> (Leipzig Viet, 1914).

71. Evans, M. *Optickle2 - MATLAB based, frequency domain, quantum-opto-mechanics simulation of optical interferometers* https://git.ligo.org/IFOsim/Optickle2. Accessed: 2017-05-21. <https://git.ligo.org/IFOsim/Optickle2>.

72. Barsotti, L., Evans, M. & Fritschel, P. Alignment sensing and control in advanced LIGO. *Classical and Quantum Gravity* **27,** 084026 (2010).

73. Mueller, G. Beam jitter coupling in advanced LIGO. *Optics Express* **13,** 7118 (2005).

74. Seymour, B., Kasprzack, A. P. M. & Mullavey, A. *Non-Linear Angular Noise Coupling into Differential Arm Length* tech. rep. (2017). <https://dcc.ligo.org/LIGO-T1700343>.

75. Bayer-Helms, F. Coupling coefficients of an incident wave and the modes of spherical optical resonator in the case of mismatching and misalignment. *Applied Optics* **23,** 1369 (1984).

76. Heinzel, G. *Advanced optical techniques for laser-interferometric gravitational-wave detectors* PhD thesis (MPI für Quantenoptik, 1999).

77. Sidles, J. A. & Sigg, D. Optical torques in suspended Fabry Perot interferometers. *Physics Letters A* **354,** 167 (2006).

78. Dooley, K. L. *et al.* Angular control of optical cavities in a radiation-pressure-dominated regime: the Enhanced LIGO case. *J. Opt. Soc. Am. A* **30,** 2618 (2013).

79. Dooley, K. L. *Design and performance of high laser power Interferometers for gravitaional-wave detection* PhD thesis (University of Florida, 2011).

80. LIGO Laboratory. *aLIGO LLO Loggbook* <https://alog.ligo-la.caltech.edu>.

81. LIGO Laboratory. *LIGO document control center* <https://dcc.ligo.org/dcc>.

82. Smith, M. & Coyne, D. *Advanced LIGO L1 Optical Layout, ZEMAX* tech. rep. (2016). <https://dcc.ligo.org/LIGO-D0902216-v8>.

83. Mueller, C. L. *Techniques for Resonant Optical Interferometry with Applications to the Advanced LIGO Gravitaional Wave Detectors* PhD thesis (University of Florida, 2014). <https://dcc.ligo.org/LIGO-P1400148>.

84. Mullavey, A. *IMC FSR measurement (alog 24782)* aLIGO LLO Logbook. 2016. <https://alog.ligo-la.caltech.edu/aLOG/index.php?callRep=24782>.

85. Fritschel, P. & Gustafson, E. *Advanced LIGO Optical Layout* tech. rep. (2016). <https://dcc.ligo.org/LIGO-D0902838>.

86. Korth, W., Arai, K. & Lewis, J. *aLIGO L1 OMC as-built diagram* tech. rep. (2013). <https://dcc.ligo.org/LIGO-D1300507>.

87. Waldman, S. *ISC Gouy phase telescopes* tech. rep. (2012). <https://dcc.ligo.org/LIGO-T1000247>.

88. Fishner, J. & Sanchez, E. *ISC HAM6 Assembly* tech. rep. (2018). <https://dcc.ligo.org/LIGO-D1000342>.

89. Billingsley, G. *LIGO optics* <https://galaxy.ligo.caltech.edu/optics/>.

90. Kasprzack, M. *ASC DC Calibration* aLIGO LLO Logbook. 2016. <https://alog.ligo-la.caltech.edu/aLOG/index.php?callRep=25777>.

91. Kasprzack, M. & Ramirez, K. *ASC REFL sensing matrix Measurements* aLIGO LLO Logbook. 2016. <https://alog.ligo-la.caltech.edu/aLOG/index.php?callRep=28761>.

92. Lewis, J. *ETM-07 Fiducial Line Measurements* tech. rep. (2013). <https://dcc.ligo.org/LIGO-E1300397>.

93. Lewis, J. & Billingsley, G. *ITM-04 Fiducial Line Measurements* tech. rep. (2012). <https://dcc.ligo.org/LIGO-E1200706>.

94. Lewis, J. & Billingsley, G. *ITM-08 Fiducial Line Measurements* tech. rep. (2012). <https://dcc.ligo.org/LIGO-E1200607>.

95. Lewis, J. *BS-02 Fiducial Line Measurements* tech. rep. (2012). <https://dcc.ligo.org/LIGO-E1200464>.

96. Lewis, J. *PRM-02 Fiducial Line Measurements* tech. rep. (2012). <https://dcc.ligo.org/LIGO-E1200438>.

97. Billingsley, G. *SRM-03 Fiducial Line Measurements* tech. rep. (2017). <https://dcc.ligo.org/LIGO-E1700215>.

98. Lewis, J. *CP-06 Fiducial Measurements at CIT* tech. rep. (2012). <https://dcc.ligo.org/LIGO-E1200210>.

99. Lewis, J. *CP-03 Fiducial Line Measurements* tech. rep. (2012). <https://dcc.ligo.org/LIGO-E1200502>.

100. Fritschel, P. & Gustafson, E. *Advanced LIGO Optical Layout* tech. rep. (2016). <https://dcc.ligo.org/LIGO-D0902838>.

101. Chavez, J. E. & Sanchez, E. *aLIGO Systems, LHAM2-L1 Top Level Chamber Assembly* tech. rep. (2016). <https://dcc.ligo.org/D0900365>.

102. Fishner, J. & Torrie, C. *ISC HAM1 Assembly* tech. rep. (2016). <https://dcc.ligo.org/D1000313>.

103. Kasprzack, M. *L1 ASC Calibration* tech. rep. (2016). <https://dcc.ligo.org/LIGO-T1600136>.

104. Barsotti, L. *ASC configuration for O1 for L1&H1* tech. rep. (2015). <https://dcc.ligo.org/LIGO-G1501333>.

105. Fishner, J. & Barsotti, L. *ISC HAM3 Assembly* tech. rep. (2014). <https://dcc.ligo.org/LIGO-D1000339>.

106. Barsotti, L. & Whitcomb, S. *TRANSMON ISC EX: component specifications and beam routing* tech. rep. (2013). <https://dcc.ligo.org/LIGO-D1201457>.

107. Fishner, J., Mailand, K., Barnum, S. & Barsotti, L. *ISC TRANSMON ASSEMBLY* tech. rep. (2013). <https://dcc.ligo.org/LIGO-D1000484>.

108. Barsotti, L. *TRANSMON ISC EY: component specifications and beam routing* tech. rep. (2013). <https://dcc.ligo.org/LIGO-D1201458>.

109. Brown, D., Adya, V., Töyrä, D., Freise, A. & Green, A. *Composite mirrors and modelling ASC signals* tech. rep. (2017). <https://dcc.ligo.org/LIGO-T1700114>.